Haemodynamics of Large Vessels by Phase Contrast MRI

Merih Cibiş

2016

Enabling new technology

This research is supported by the Dutch Technology Foundation STW, which is part of the Netherlands Organisation for Scientific Research (NWO) and partly funded by the Ministry of Economic Affairs (Carisma 11629).

Printing of this thesis was supported by the Dutch Technology Foundation STW and
Erasmus University in Rotterdam.

Printed in the Netherlands by Optima Grafische Communicatie
Cover design by: http://www.joos-illustraties.nl/

ISBN: 978-94-6169-814-8

Haemodynamics of Large Vessels by Phase Contrast MRI

Hemodynamiek van de grote vaten door phase contrast MRI

Thesis

to obtain the degree of Doctor from the
Erasmus University Rotterdam
by command of the
rector magnificus
Prof.dr. H.A.P. Pols
and in accordance with the decision of the Doctorate Board
The public defense shall be held on
Friday February 19th 2016 at 11.30 hours

by

Merih Cibiş
born in Eskişehir, Turkey

Erasmus University Rotterdam

DOCTORAL COMMITTEE

Promoter	Prof. dr. ir. A.F.W. van der Steen
Other members	Prof. dr. W.A. Helbing Prof. dr. E.T. van Bavel Prof. dr. M. Markl
Co-promoters	Dr. ir. J.J. Wentzel Dr. ir. A.J. Nederveen

Financial support by the Dutch Heart Foundation for the publication of this thesis is gratefully acknowledged.

TABLE OF CONTENTS

Chapter 1

Introduction

CARDIOVASCULAR DISEASES

The cardiovascular system is the network of blood vessels in the body with the major role in the transportation of oxygen and nutrition to the organs and the waste products from the organs. The diseases of the cardiovascular system, either acquired or congenital, may result in ischemia or undersupply of major organs, which is a threat to the overall health of an individual. Events caused by cardiovascular diseases are the leading cause of morbidity and mortality worldwide. Despite improvements in the treatment and the prevention strategies of cardiovascular diseases, the social and economic burdens due to these diseases continue to grow[1]. Further efforts, therefore, are required to find underlying mechanisms of these diseases and to find effective risk predicting markers for prevention and treatment. This thesis focuses on two diseases which are examples of acquired and congenital cardiovascular diseases: carotid atherosclerosis and univentricular heart (repaired with Fontan operation).

Carotid atherosclerosis

The first part of the thesis is devoted to carotid atherosclerosis. The carotid arteries are the main blood suppliers of the brain. They are located on the left and right side in the neck and they bifurcate to two arteries: internal carotid artery and external carotid artery (figure 1). Large and medium-sized arteries, including carotid arteries, are frequently affected by atherosclerosis. Atherosclerosis is an inflammatory disease which initiates at very early ages and progresses silently through decades[2]. Asymptomatic carotid atherosclerosis is highly prevalent in general population[3] yet most are unaware of its presence[4]. It is characterized by accumulation of cholesterol, calcium, lipid and other waste, also called plaques, within the inner walls of arteries[5]. The endothelial cells, which are the cells forming the innermost layer of the artery wall, have a central role in initiation and progression of atherosclerosis[6]. Endothelial cells are semi-permeable and they control the transfer of molecules between the blood and the artery wall. They regulate inflammatory responses by controlling leukocyte and lymphocyte interactions and release vasoactive substances which modulate vascular tone[7-11]. Impaired endothelial function causes a reduction of vasoactive substances, an increase in endothelial permeability, proliferation and migration of smooth muscle cells, the release of pro-inflammatory factors, and the adhesion of leukocytes to the walls. Endothelial dysfunction is a systemic disorder affected by the risk factors such as smoking, hyperlipidemia, diabetes mellitus, hypertension and aging[12,13]. Despite dependency on the systemic risk factors, atherosclerosis is a focal disease which initiates at preferred sites; such as the inner curves of bending arteries or at branching points[14]. The site preference of the disease is associated with the local haemodynamic patterns.

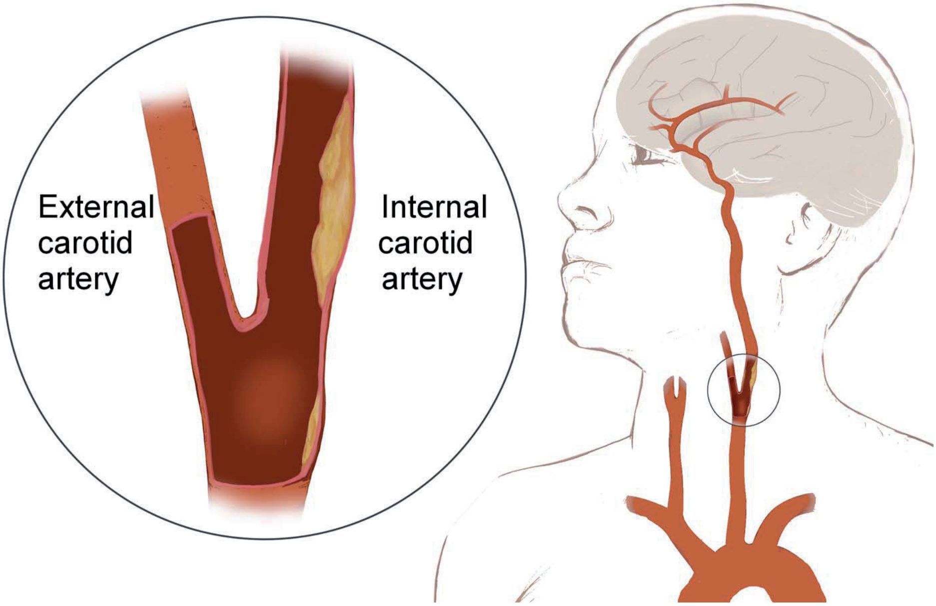

Figure 1. Carotid arteries are located at the right and left side in the neck. A carotid artery bifurcates to two arteries: internal carotid artery and external carotid artery. Carotid bulb is the major site for initiation of carotid atherosclerosis. The image is adapted from www.silkroadmedical.com

In the early stage of the disease, atherosclerotic burden causes expansion of the arterial wall while lumen area is preserved, also referred as outward remodelling[15]. As the disease progresses, the plaque area enlarges, which narrows the lumen of the artery. Plaque progression is not always related to clinical outcome. Although severe lumen narrowing increases the risk of stroke, such a clinical event is frequently caused by plaque rupture and the lumen obstruction due to thrombosis[16-18].

Univentricular Heart and Fontan Circulation

The second part of the thesis focuses on univentrical heart which is a congenital heart disease and characterized by one fully functioning heart. Congenital heart diseases occur in approximately 1% of newborns[19] and nearly 10% of these malformations belong to the group of univentricular heart[20]. In patients with univentricular heart, the functioning ventricle receives the flow of the pulmonary and systemic circulation, which causes a volume overload in the ventricle and reduces the functional ability of the heart[21]. In the early 70's, Fontan and Baudet introduced a palliative surgical technique that separated systemic and pulmonary venous return hence reduced the overload of the heart in patients with tricuspid atresia[22]. Since the introduction of the original technique, it has been adapted greatly and also applied to the patients with other sub-types of univentricular heart. Currently, infants with univentricular heart undergo multiple consecutive operations with the final surgical operation, creating so called Fontan circulation. The Fontan circulation separates systemic and pulmonary venous return by creating a direct connection between caval veins and pulmonary arteries and thus passively filling the pulmonary circulation. Two surgical approaches, which are called intracardiac lateral tunnel (ILT)[23] and extracardiac conduit (ECC)[24], are favored to create a Fontan circulation. The ILT approach involves placement of an intraatrial baffle (figure 2a) while the ECC approach (figure 2b) creates an anastomosis between the pulmonary arteries and the inferior caval vein with a prosthetic conduit[25,26]. The latest developments in these surgical procedures increased the life expectancy of these patients. However, adverse long term effects such as limited pulmonary artery growth or exercise intolerance still remain unsolved. Growing evidence shows that the adverse long term effects after Fontan operation are associated with the flow conditions in Fontan circulation.

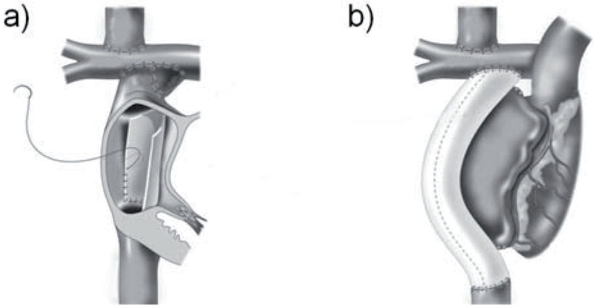

Figure 2. a) Intra-lateral tunnel Fontan operation. A baffle is replaced inside atrium that connected the inferior caval vein to the pulmonary arteries b) Extra-cardiac conduit Fontan operation. The caval veins and the pulmonary arteries are connected with a prosthesis graft. The image is adapted from[27].

HAEMODYNAMICS

Haemodynamics is the study of the physical laws related to the dynamic behavior of blood in the cardiovascular system. The majority of all cardiovascular diseases is associated with the abnormalities in haemodynamics. Among others, three haemodynamic parameters derived from the blood flow are associated with the two diseases which are the subject of this thesis: wall shear stress (WSS), oscillatory shear index (OSI) and power loss.

WSS is the tangential stress exerted by the blood flow on the endothelial cells. It is caused by the velocity gradients of the adjacent blood fluid layers. The magnitude of WSS can be calculated by multiplying dynamic viscosity of blood by wall shear rate. Wall shear rate is the spatial gradient of blood velocities near wall in the radial direction. Calculation of WSS requires information on velocity field.

OSI is derived from WSS, which measures the changes in WSS direction over one cardiac cycle. OSI is a dimensionless parameter and has a magnitude between 0 and

0.5 where 0 corresponds to unidirectional shear flow and 0.5 to pure oscillatory flow. Calculation of OSI requires information on the temporal changes of WSS.

Power loss is the conversion of kinetic energy of fluid into heat due to viscous resistance. It can be calculated by two different flow equations: the mechanical energy balance equation and the viscous dissipation term of the Navier Stokes equations. The latter method can only be used if the blood flow is in a laminar regime. While the former method requires information on both pressure and velocity field, the latter method requires information only on velocity field.

Haemodynamics in carotid atherosclerosis

Previous studies showed that the endothelial cells are responsive to the haemodynamic conditions. Disturbed flow conditions, which are defined as low **wall shear stress**[28-32] and high **oscillatory shear index**, cause endothelial dysfunction and affect endothelial permeability. Atherosclerotic plaques therefore initiate at regions of disturbed flow conditions. Quantification of WSS and OSI is essential to understand the underlying mechanism of atherosclerotic plaque formation and to predict the initiation and the progression of the disease.

Haemodynamics in Fontan Circulation

Some of the complications of Fontan circulation are associated with unfavorable flow conditions due to the surgical connection of caval veins and pulmonary arteries. The Fontan circulation prevents systemic venous return to ventricle hence the blood flows passively from caval veins to the pulmonary arteries. This reduces the blood flow and **wall shear stress** in pulmonary arteries, which might cause endothelial dysfunction. Impaired endothelial function might lead to limited pulmonary artery growth and impaired pulmonary functioning[33].

Studies also show increasing evidence that the impaired exercise capacity of Fontan patients is associated with haemodynamic flow conditions inside Fontan circulation. The complex flow patterns and specifically elevated **power loss** is related to the limited exercise capacity[34-37]. The power loss inside the Fontan circulation increases nonlinearly during exercise and reflects the inefficiency of the surgically created geometry. Quantification of power loss might provide information to detect the patients with haemodynamically inefficient Fontan circulation, which might be the potential cause of the limited exercise capacity.

QUANTIFICATION OF HAEMODYNAMIC PARAMETERS

The haemodynamic parameters associated with the aforementioned diseases can be calculated when the velocity field is known. 3D blood velocities inside vessels are generally obtained by computational fluid dynamics. Alternatively, the velocities can be non-invasively measured by phase contrast MRI measurements.

Computational fluid dynamics

Computational fluid dynamics (CFD) is a method for modelling fluid flow and related phenomena by using applied mathematics, physics and computational software. It is based on the flow equations, which are also called Navier-Stokes equations. For complex flows, these equations cannot be solved analytically. Hence these equations are discretized and solved in an iterative manner for smaller volumes. Since computational fluid dynamics has been used widely in various industries, commercial software packages are available which are validated and ready to use. CFD requires several pre-processing steps. Firstly, the flow geometry is described and divided into small volumes, which are called mesh elements. The fluid properties such as density, viscosity are defined. The boundary conditions, i.e. pressure and velocity conditions at the boundaries are defined. The set of coupled flow equations and the method for discretizing the equations are chosen and the convergence criteria are set.

Cardiovascular flows are difficult to simulate due to complex geometries and the flow conditions. Numerical simulations for such flows require special attention for the meshing procedures and the solution methods. There are many open source and commercial software packages available for this kind of simulations and all solvers provide different choices in the solution methods. In cardiovascular applications, vessel geometry can be obtained based on the subject-specific images obtained with i.e. MRI. Similarly, patient-specific boundary conditions can be applied by using flow or pressure measurements. The fluid properties such as density and viscosity can also be measured but these properties are generally approximated according to population-averaged values reported in literature. The simulations result in 3D velocity and pressure field, which can be used to calculate haemodynamic parameters.

Phase Contrast Magnetic Resonance Imaging

Phase contrast MRI is a non-invasive technique to measure the blood velocity field in large vessels by using the magnetic properties of water molecules inside flowing blood in an external magnitude field[38,39]. Exposing blood protons to a magnetic bipolar gradient field causes a phase shift in the MRI-signal that originates from these protons. This phase shift is proportional to the velocity of protons and the stationary protons have a zero net phase shift. These phase shifts are extracted as images after Fourier transformation of the MRI signal and the pixel intensity of these phase difference images are used to quantify the blood velocities.

Recently, three dimensional time-resolved ECG and respiratory navigator gated phase contrast MRI with velocity encoding in 3 directions, also called 4D flow MRI, has been developed and applied for evaluation of cardiovascular haemodynamics[40]. These MRI measurements provide time-resolved volumetric velocity information which can be used to derive haemodynamic parameters.

CFD and phase contrast MRI methods have both advantages and disadvantages. Main drawback of the former originates from the many underlying assumptions and simplifications. In addition, the accuracy of the CFD results relies on the accurate boundary conditions. CFD requires longer computational time, non-clinical expertise and tools, while phase contrast MRI is a technology already available for clinical use. CFD has however the advantage of providing velocity and pressure information at both high spatial and temporal resolution while velocity field based on phase contrast MRI is limited in spatial and temporal resolution. CFD has been widely used in different disciplines in industry and research; hence many validated CFD softwares are available. CFD has also been commonly used in estimation of haemodynamic parameters. Phase contrast MRI is an emerging technique hence its validation is required in estimation of haemodynamic parameters and the effect of its limited resolution on the estimated values of the haemodynamic parameters had to be investigated.

OUTLINE OF THE THESIS

Since the local haemodynamic conditions are associated with the initiation and progression of the cardiovascular diseases and the cardiovascular status of the patients, evaluation of the haemodynamic parameters is essential.

The aim of this thesis is to estimate haemodynamic parameters associated with carotid atherosclerosis and univentricular heart repaired with Fontan operation by using phase contrast MRI and computational fluid dynamics.

The chapters 2 to 5 focus on the quantification of haemodynamic parameters associated with carotid atherosclerosis. In these chapters, the effect of spatial and temporal resolution of phase contrast MRI on the estimated magnitude of wall shear stress and oscillatory shear index is studied. The phase contrast MRI based quantification is validated by using computational fluid dynamics.

In **chapter 2**, wall shear stress in carotid arteries of young and healthy volunteers is studied. The magnitude of wall shear stress, the direction of the wall shear stress vectors and the wall shear stress patterns calculated by ECG-gated time-resolved 3D phase contrast MRI measurements are compared with those based on computational fluid dynamics.

In **chapter 3**, wall shear stress in carotid arteries of elderly subjects with asymptomatic atherosclerotic plaque is studied. The subjects of this study are selected from a cohort study, Rotterdam study, in which untriggered 3D phase contrast MRI measurements were repeated within approximately four years of follow-up time with limited spatiotemporal resolution. In this population based setting, phase contrast MRI based wall shear stress is compared with that based on computational fluid dynamics. The changes in baseline and follow-up wall shear stress distribution are investigated. The relation between wall shear stress and carotid artery wall thickness is examined in elderly subjects.

In **chapter 4**, the effect of the spatial and temporal resolution of phase contrast MRI on the estimated values of mean and peak flow, wall shear stress and oscillatory shear index is investigated. ECG-gated time-resolved 2D phase contrast MRI measurements were performed at two measurement planes of a subject-specific carotid artery phantom at thirty different spatiotemporal resolutions. The haemodynamic parameters are calculated for each phase contrast MRI measurement and compared with each other.

In **chapter 5**, the relation between atherosclerotic plaque composition and computational fluid dynamics based wall shear stress distribution is examined. Seventy four subjects are selected from Rotterdam study. The presence of large lipid necrotic core, intra-plaque hemorrhage and calcium is evaluated and the wall shear stress at the regions of plaque with these components is examined.

The chapters 6 to 9 are devoted to evaluate the haemodynamic parameters associated with the complication after Fontan operation. The quantification of these parameters is also based on computational fluid dynamics and phase contrast MRI.

In **chapter 6**, power loss in Fontan circulations is studied using computational fluid dynamics. The nonlinear effect of exercise on power loss is investigated by calculating power loss at rest and during simulated exercise conditions in twenty nine Fontan patients. Exercise is simulated by dobutamine administration. The flow through the caval veins at rest and under exercise conditions is measured by ECG-gated time-resolved 2D phase contrast MRI.

In **chapter 7**, power loss in Fontan circulations is calculated based on ECG-gated time-resolved 3D phase contrast MRI measurements and compared with computational fluid dynamics. The effect of the spatial resolution of phase contrast MRI on the estimated value of power loss is investigated by down-sampling the velocities obtained by computational fluid dynamics and by generating MRI-like data. The effect of measurement noise on power loss is also examined by adding noise on down-sampled velocities.

In **chapter 8**, changes in wall shear stress distribution, pulmonary artery size, pulsatility and distensibility within approximately five years of follow-up time are investigated in Fontan patients. ECG-gated time-resolved 2D phase contrast MRI in the left pulmonary arteries of Fontan patients is performed at baseline and after 5 years of follow-up.

In **chapter 9**, the influence of 3 months of regular training on wall shear stress, pulsatility and distensibility is studied in Fontan patients. The haemodynamic parameters are investigated in caval veins and pulmonary arteries by using ECG-gated time-resolved 2D phase contrast MRI measurements.

In **chapter 10**, the main findings of this thesis and their implications are discussed and the future perspective is presented.

REFERENCES

[1] Roth GA, Forouzanfar MH, Moran AE, Barber R, Nguyen G, Feigin VL, Naghavi M, Mensah GA, Murray CJ. Demographic and epidemiologic drivers of global cardiovascular mortality.N Engl J Med. 2015 Apr 2;372(14):1333-41.

[2] Prati P, Vanuzzo D, Casaroli M, Di Chiara A, De Biasi F, Feruglio GA, Touboul PJ. Prevalence and determinants of carotid atherosclerosis in a general population. Stroke. 1992 Dec; 23(12): 1705-11.

[3] Bos D, van der Rijk MJ, Geeraedts TE, Hofman A, Krestin GP, Witteman JC, van der Lugt A, Ikram MA, Vernooij MW.Intracranial carotid artery atherosclerosis: prevalence and risk factors in the general population. Stroke. 2012 Jul;43(7):1878-84.

[4] Prati P, Vanuzzo D, Casaroli M, Di Chiara A, De Biasi F, Feruglio GA, Touboul PJ. Prevalence and determinants of carotid atherosclerosis in a general population. Stroke. 1992 Dec; 23 (12): 1705-11.

[5] Mughal MM, Khan MK, DeMarco JK, Majid A, Shamoun F, Abela GS. Symptomatic and asymptomatic carotid artery plaque. Expert Rev Cardiovasc Ther. 2011 Oct;9(10):1315-30.

[6] Davignon J, Ganz P. Role of endothelial dysfunction in atherosclerosis. Circulation. 2004 Jun 15;109(23 Suppl 1):III27-32.

[7] Libby P, Ridker PM, Maseri A. Inflammation and atherosclerosis. Circulation. 2002 Mar 5; 105(9): 1135-43.

[8] Ross R Atherosclerosis-- an inflammatory disease. N Engl J Med. 1999 Jan 14;340(2):115-26.

[9] Deanfield JE, Halcox JP, Rabelink TJ Endothelial function and dysfunction: testing and clinical relevance.Circulation. 2007 Mar 13;115(10):1285-95.

[10] Ross R. The pathogenesis of atherosclerosis: a perspective for the 1990s. Nature. 1993 Apr 29;362(6423):801-9.

[11] Sumpio BE, Riley JT, Dardik A. Cells in focus: endothelial cell. Int J Biochem Cell Biol. 2002 Dec;34(12):1508-12.

[12] Hadi HA, Carr CS, Al Suwaidi J. Endothelial dysfunction: cardiovascular risk factors, therapy and outcome. Vasc Health Risk Manag. 2005;1(3):183-98.

[13] Bonetti PO, Lerman LO, Lerman A. Endothelial dysfunction: a marker of atherosclerotic risk. Arterioscler Thromb Vasc Biol. 2003 Feb 1;23(2):168-75.

[14] VanderLaan PA, Reardon CA, Getz GS. Site specificity of atherosclerosis: site-selective responses to atherosclerotic modulators. Arterioscler Thromb Vasc Biol. 2004 Jan;24(1):12-22. Epub 2003 Nov 6.

[15] van Gils MJ, Vukadinovic D, van Dijk AC, Dippel DW, Niessen WJ, van der Lugt A. Carotid atherosclerotic plaque progression and change in plaque composition over time: a 5-year follow-up study using serial CT angiography. AJNR Am J Neuroradiol. 2012 Aug;33(7): 1267-73.

[16] Virmani R, Finn AV, Kolodgie FD. Carotid plaque stabilization and progression after stroke or TIA. Arterioscler Thromb Vasc Biol. 2009 Jan;29(1):3-6.

[17] Bentzon JF, Otsuka F, Virmani R, Falk E. Mechanisms of plaque formation and rupture. Circ Res. 2014 Jun 6;114(12):1852-66.

[18] Gupta A, Baradaran H, Schweitzer AD, Kamel H, Pandya A, Delgado D, Dunning A, Mushlin AI, Sanelli PC. Carotid plaque MRI and stroke risk: a systematic review and meta-analysis. Stroke. 2013 Nov;44(11):3071-7.

[19] Hoffman JI. Congenital heart disease: incidence and inheritance. Pediatr Clin North Am. 1990 Feb;37(1):25-43.

[20] Kaulitz R, Hofbeck M. Current treatment and prognosis in children with functionally univentricular hearts. Arch Dis Child. 2005 Jul;90(7):757-62.

[21] Khairy P, Poirier N, Mercier LA. Univentricular heart. Circulation. 2007 Feb 13; 115(6): 800-12.

[22] Fontan F, Baudet E. Surgical repair of tricuspid atresia. Thorax1971;26:240–8.

[23] Puga FJ, Chiavarelli M, Hagler DJ. Modifications of the Fontan operation applicable to patients with left atrioventricular valve atresia or single atrioventricular valve. Circulation 1987;76 Suppl III:III53-III60.

[24] Marcelletti C, Corno A, Giannico S, Marino B. Inferior vena cava-pulmonary artery extracardiac conduit. A new form of right heart bypass. J Thorac Cardiovasc Surg 1990;100:228-232.

[25] Lee JR, Kwak J, Kim KC, Min SK, Kim WH, Kim YJ, Rho JR. Comparison of lateral tunnel and extracardiac conduit Fontan procedure. Interact Cardiovasc Thorac Surg. 2007 Jun; 6(3):328-30. Epub 2007 Mar 15.

[26] Kumar SP, Rubinstein CS, Simsic JM, Taylor AB, Saul JP, Bradley SM. Lateral tunnel versus extracardiac conduit Fontan procedure: a concurrent comparison. Ann Thorac Surg. 2003 Nov;76(5):1389-96; discussion 1396-7.

[27] d'Udekem Y, Iyengar AJ, Cochrane AD, Grigg LE, Ramsay JM, Wheaton GR, Penny DJ, Brizard CP. The Fontan procedure: contemporary techniques have improved long-term outcomes. Circulation. 2007 Sep 11;116(11 Suppl):I157-64.

[28] Cecchi E, Giglioli C, Valente S, Lazzeri C, Gensini GF, Abbate R, Mannini L. Role of hemodynamic shear stress in cardiovascular disease. Atherosclerosis. 2011 Feb;214(2):249-56.

[29] Peiffer V, Sherwin SJ, Weinberg PD. Does low and oscillatory wall shear stress correlate spatially with early atherosclerosis? A systematic review. Cardiovasc Res. 2013 Jul 15;99(2):242-50.

[30] Chatzizisis YS, Coskun AU, Jonas M, Edelman ER, Feldman CL, Stone PH. Role of endothelial shear stress in the natural history of coronary atherosclerosis and vascular remodeling: molecular, cellular, and vascular behavior. J Am Coll Cardiol. 2007 Jun 26;49(25):2379-93.

[31] Malek AM, Alper SL, Izumo S. Hemodynamic shear stress and its role in atherosclerosis. JAMA. 1999 Dec 1;282(21):2035-42.

[32] Wentzel JJ, Chatzizisis YS, Gijsen FJ, Giannoglou GD, Feldman CL, Stone PH. Endothelial shear stress in the evolution of coronary atherosclerotic plaque and vascular remodelling: current understanding and remaining questions. Cardiovasc Res. 2012 Nov 1;96(2):234-43.

[33] Morgan VL, Graham TP Jr, Roselli RJ, Lorenz CH. Alterations in pulmonary artery flow patterns and shear stress determined with three-dimensional phase-contrast magnetic resonance imaging in Fontan patients. J Thorac Cardiovasc Surg. 1998 Aug;116(2):294-304.

[34] Whitehead KK, Pekkan K, Kitajima HD, Paridon SM, Yoganathan AP, Fogel MA. Nonlinear power loss during exercise in single-ventricle patients after the Fontan: insights from computational fluid dynamics. Circulation. 2007 Sep 11;116(11 Suppl):I165-71.

[35] Restrepo M, Tang E, Haggerty CM, Khiabani RH, Mirabella L, Bethel J, Valente AM, Whitehead KK, McElhinney DB, Fogel MA, Yoganathan AP. Energetic implications of vessel growth and flow changes over time in Fontan patients. Ann Thorac Surg. 2015 Jan;99(1):163-70.

[36] Haggerty CM, Restrepo M, Tang E, de Zélicourt DA, Sundareswaran KS, Mirabella L, Bethel J, Whitehead KK, Fogel MA, Yoganathan AP. Fontan hemodynamics from 100 patient-specific cardiac magnetic resonance studies: a computational fluid dynamics analysis. J Thorac Cardiovasc Surg. 2014 Oct;148(4):1481-9.

[37] Dasi LP, Pekkan K, Katajima HD, Yoganathan AP. Functional analysis of Fontan energy dissipation. J Biomech. 2008 Jul 19;41(10):2246-52

[38] Von Schulthess GK, Higgins CB. Blood flow imaging with MR: spin phase phenomena. Radiology 157:687-695.

[39] Nayak KS, Nielsen JF, Bernstein MA, Markl M, D Gatehouse P, M Botnar R, Saloner D, Lorenz C, Wen H, S Hu B, Epstein FH, N Oshinski J, Raman SV. Cardiovascular magnetic resonance phase contrast imaging. J Cardiovasc Magn Reson. 2015 Aug 9;17(1):71.

[40] Dyverfeldt P, Bissell M, Barker AJ, Bolger AF, Carlhäll CJ, Ebbers T, Francios CJ, Frydrychowicz A, Geiger J, Giese D, Hope MD, Kilner PJ, Kozerke S, Myerson S, Neubauer S, Wieben O, Markl M. 4D flow cardiovascular magnetic resonance consensus statement. J Cardiovasc Magn Reson. 2015 Aug 10;17(1):72.

Part 1

Carotid Atherosclerosis

Chapter 2

Wall Shear Stress Calculations based on 3D Cine Phase Contrast MRI and Computational Fluid Dynamics: a Comparison Study in Healthy Carotid Arteries

Based on:

Cibis, M, Potters, WV, Gijsen, FJH, Marquering, H, vanBavel, E,van der Steen, AFW, Nederveen, AJ, Wentzel JJ. Wall shear stress calculations based on 3D cine phase contrast MRI and computational fluid dynamics: a comparison study in healthy carotid arteries. NMR Biomed. 2014 Jul; 27(7):826-34.

ABSTRACT

Wall shear stress (WSS) is involved in many pathophysiological processes related to cardiovascular diseases and knowledge of WSS may provide vital information on disease progression. WSS is generally quantified with computational fluid dynamics (CFD), but can also be calculated using phase contrast (PC) MRI measurements. In this study, our objectives were to calculate WSS on the entire luminal surface of human carotid arteries using PC MRI velocities (WSS_{MRI}) and to compare it with WSS based on CFD (WSS_{CFD}).

Methods

Six healthy volunteers were scanned with a 3T MRI scanner. WSS_{CFD} was calculated using a generalized flow waveform with a mean flow equal to the mean measured flow. WSS_{MRI} was calculated by estimating the velocity gradient along the inward normal of each mesh node on the luminal surface. Furthermore, WSS ($WSS_{CFDlowres}$) was calculated for a down-sampled CFD velocity field mimicking the MRI resolution. To ensure minimum temporal variation, WSS was analyzed only at diastole. The patterns of WSS_{CFD} and WSS_{MRI} were compared by quantifying the overlap between low, medium and high WSS tertiles. Finally, WSS directions were compared by calculating the angles between the WSS_{CFD} and WSS_{MRI} vectors.

Results

WSS_{MRI} magnitude was lower than WSS_{CFD} (0.62±0.18Pa vs. 0.88±0.30Pa, $p<0.01$) but closer to $WSS_{CFDlowres}$ (0.56±0.18Pa, $p<0.01$). WSS_{MRI} patterns matched well with WSS_{CFD}. The overlap area was 68.7±4.4% in low and 69.0±8.9% in high WSS tertiles. The angles between WSS_{MRI} and WSS_{CFD} vectors were small in the high WSS tertiles (20.3±8.2°), but larger in the low WSS tertiles (65.6±17.4°).

Conclusions

Although WSS_{MRI} magnitude was lower than WSS_{CFD}, the spatial WSS patterns at diastole, which are more relevant to the vascular biology, were similar. PC MRI based WSS has potential to be used in the clinic to indicate regions of low and high WSS and the direction of WSS especially in regions of high WSS.

INTRODUCTION

Flow induced wall shear stress (WSS) is an important biomechanical parameter widely accepted to influence the endothelial function in the vasculature and is thereby involved in many pathophysiological processes related to cardiovascular diseases[1]. The majority of the studies showed that in the presence of risk factors, atherosclerotic plaques mainly form in the regions of low and oscillatory WSS[2-7]. Other studies also suggested that high WSS has a pathogenic effect on the initiation of aneurysm formation, while low WSS facilitates aneurysm growth[8]. These findings suggest that knowledge of WSS may provide vital information about the initiation and progression of vascular diseases. Nevertheless, WSS assessment has not been integrated into clinical practice. This is mainly due to the difficulty of determining WSS in vivo. WSS can be calculated by multiplying the blood viscosity with wall shear rate (WSR), the latter being the gradient of blood flow velocity in the normal direction of the vessel wall. The commonly used method for determining 3D blood flow velocities and WSS is computational fluid dynamics (CFD). CFD has the advantage of solving velocities at a high spatial and temporal resolution. However, the disadvantage of CFD is that it requires non-clinical expertise and extensive computational power. Phase contrast (PC) MRI can also measure time resolved 3D velocities and several methods have been developed to quantify WSS using PC MRI velocities. In earlier studies, WSS calculation was based on parabolic fitting of the velocities measured by 2D PC MRI[9-16]. This approach was improved by using b-splines for the fitting of velocities measured by 3D cine PC MRI in more recent studies[17-20]. A drawback of these studies was that WSS calculations were limited to planar slices within an artery. Recently, a new algorithm for calculation of WSS throughout the 3D luminal surface using PC MRI velocities was introduced[21]. In the current study, our objective was to compare WSS distributions on the entire 3D luminal surface of carotid arteries calculated using 3D cine PC MRI velocities with those calculated using CFD. To our knowledge, this is the first study that compares the WSS distributions based on PC MRI and CFD on the entire luminal surface of the carotid arteries.

METHODS

MRI scans

Six healthy volunteers (25-30 years old) were scanned on a 3.0T MRI system (Intera (software version 3.2.1) for the first volunteers and Ingenia (software version 4.1.3) for the last volunteer, Philips Healthcare, The Netherlands) using a dedicated 8-channel bilateral carotid coil (Chenguang Medical Technologies, Shanghai, China). A retrospectively gated 3D transient field echo (TFE) sequence with RF spoiling, a TFE factor of 8 and a parallel imaging factor (SENSE) of 2 with symmetric four-point velocity encoding was obtained with a isotropic non-interpolated resolution of 0.625 mm and a temporal resolution of 138±11ms (8 timepoints / heart cycle) as part of a carotid scan protocol (FOV/ TR/ TE/ flip angle/ bandwidth/ venc RLxAPxFH, 140x140x30mm/ 6.7ms/ 3.1ms/ 15°/ 299Hz/ px/ 60x60x100cm/sec). This 3D cine PC MRI sequence took ~20 minutes per volunteer, depending on the heart rate. No velocity aliasing was found in the images. We corrected the PC MRI datasets for possible phase-offset errors and visually checked for artifacts.

Segmentation and meshing

Three carotid arteries were excluded due to motion and pulsation artifacts and thus nine were found suitable for the analysis. We manually segmented the luminal surface of the carotid arteries on the magnitude images using ITK-SNAP[22]. We excluded small scale side branches. The segmentations were inspected on the phase images and corrected if necessary (Figure 1a). We smoothed the resulting surface with Taubin smoothing approach and split the carotid artery surface into three arteries (Figure 1b), the common carotid artery (CCA), internal carotid artery (ICA) and external carotid artery (ECA) using the open-source Vascular Modeling Toolkit (VMTK version 1.0.0)[23]. We performed the lumen segmentation only on the PC MR images acquired during diastole (t =742 ms in Figure 2a) because at this cardiac phase the blood flow fluctuations were minimal.

In the next step, we generated a tetrahedral volume mesh by using commercial mesh generation software package Gambit (Ansys). The element size was 0.12 mm at the vessel wall and increased inwardly. Each volume mesh contained approximately 1 million elements. For the computations of WSS based on PC MRI and CFD, we used the same volume mesh, enabling a one-to-one comparison between both WSS measures.

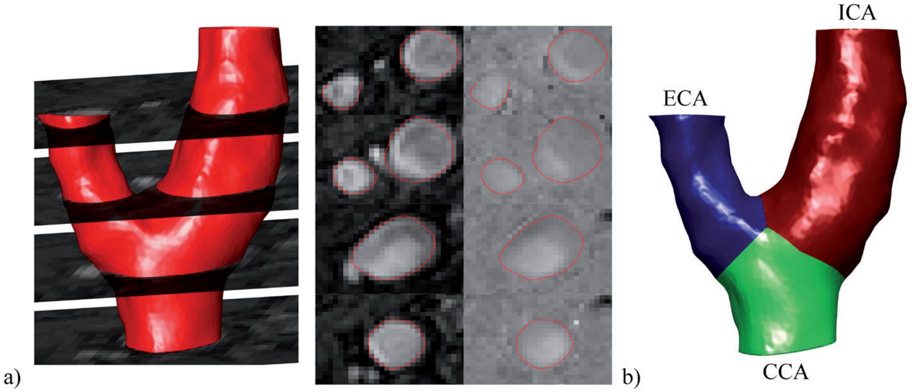

Figure 1. a) The luminal surface of the carotid artery was segmented on the magnitude images and subsequently inspected in phase images using ITK-SNAP. b) The segmented surface was split into CCA, ICA and ECA using VMTK.

WSS calculations using 3D cine PC MRI velocities

WSS based on PC MRI (WSS_{MRI}) was calculated using the 3D cine PC MRI velocities and the volume mesh, as described before[21]. In summary, we first determined the inward normal vector of each mesh node on the luminal surface. Along the normal direction, we interpolated the velocities at two inward equidistant points, which were at 1.5 and 3 mm on the inward normal. We imposed the velocity to zero on the vessel wall. We subsequently fitted a curve to the interpolated velocities using a smoothing spline. We derived the slope of this curve at the vessel wall which gives the WSR. We finally multiplied WSR with the shear dependent viscosity (Carreau-Yasuda model) resulting in WSS vectors for all mesh nodes on the vessel wall. We calculated only the diastolic WSS_{MRI}. This calculation took ~15 minutes for each carotid artery.

WSS calculations using computational fluid dynamics

We calculated the CCA, ICA and ECA flows using PC MRI velocities recorded at 8 time points (Figure 2a) as inflow boundary condition. For all carotid arteries, the sum of the ICA and ECA flows was 11±6% lower than the CCA flow. To ensure the flow conservation, ICA and ECA flows were increased in equal percentages so that the ratio of ICA and ECA flows was unaltered. Due to the limited temporal resolution of the 3D cine PC MRI measurements, the recorded flow waveform was flattened (Figure 2a). To account for the temporal flow changes in higher frequencies, we used the generalized flow waveforms of CCA and ICA reported by Lee et al[24] as substitute for the recorded flow waveforms (Figure 2b). We scaled the generalized flow waveforms so that they had mean flow rates equal to the measured mean flow rates.

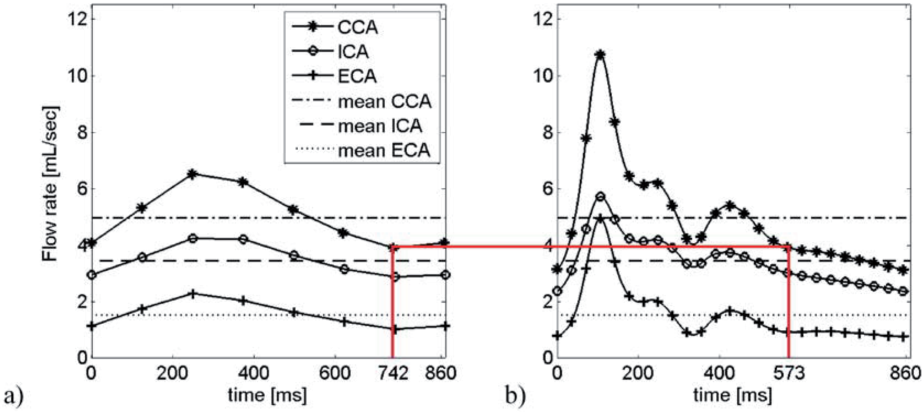

Figure 2. a) A representative flow waveform recorded at 8 time points. WSS_{MRI} was calculated using only the velocities recorded during diastole (t=742 ms) b) The generalized waveforms reported by Lee et al (24). WSS_{CFD} was calculated using only the velocities recorded during diastole (t=573 ms). The generalized and the recorded flow waveforms have equal mean flow rates.

As inflow profile, we used a single velocity profile, which was obtained by using both axial and in plane velocities and acquired during diastole (t=742ms in Figure 2a). We scaled it at each time point in the cardiac cycle so that the flow was increased or decreased according to the flow waveform but the velocity profile shape did not change (Figure 3). ECA outlet was left as stress free. Fluid density was set at 1060 kg/m^3 and the Carreau-Yasuda model was used to mimic the non-Newtonian behavior of blood with the parameters used in[25].

We performed the CFD simulations on a standard desktop computer (Intel Xeon six core processor, 2.40 GHz CPU and 12 GB RAM) using the commercial finite element software FIDAP 8.7.4 (Ansys). We set the temporal resolution to 5 ms and performed the simulations for 2 cardiac cycles. The CFD simulations took ~15 hours for each carotid artery. Although CFD results were acquired for a complete cardiac cycle, we analyzed WSS_{CFD} only in diastole (t=573 ms in Figure 2b) where CCA flow was equal to the measured diastolic CCA flow (t=742 ms in Figure 2a).

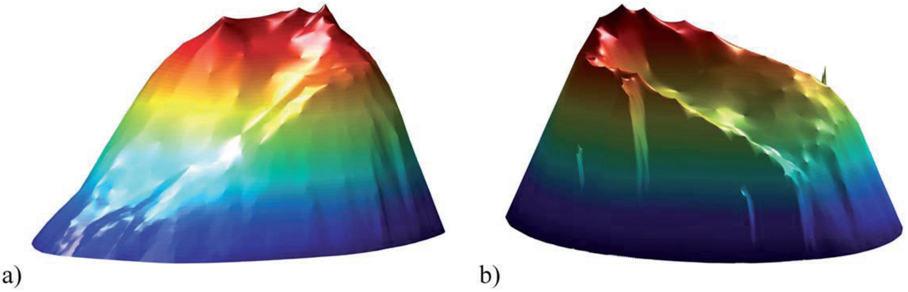

Figure 3. Shape of velocity profiles during the diastolic heart phase at the a) CCA inlet and b) ICA outlet.

Analysis of WSS_{MRI} and WSS_{CFD}

WSS magnitudes

As shown in the previous studies, the spatial resolution of the velocities may affect the calculated WSS_{MRI} values[17,21,26]. To study the effect of resolution, we down-sampled the CFD velocities into PC MRI resolution and calculated WSS ($WSS_{CFDlowres}$) based on the down-sampled velocity field. To down-sample the CFD velocity field, we first interpolated the CFD velocities to a cubic grid with an isotropic resolution of 0.1 mm. The isotropic PC MRI voxels of 0.625 mm contained ~216 of these 0.1 mm isotropic voxels. We averaged these ~216 velocity values and obtained a down-sampled CFD based velocity field that mimicked the PC MRI velocity data. The down-sampling procedure is schematically depicted in Figure 4.

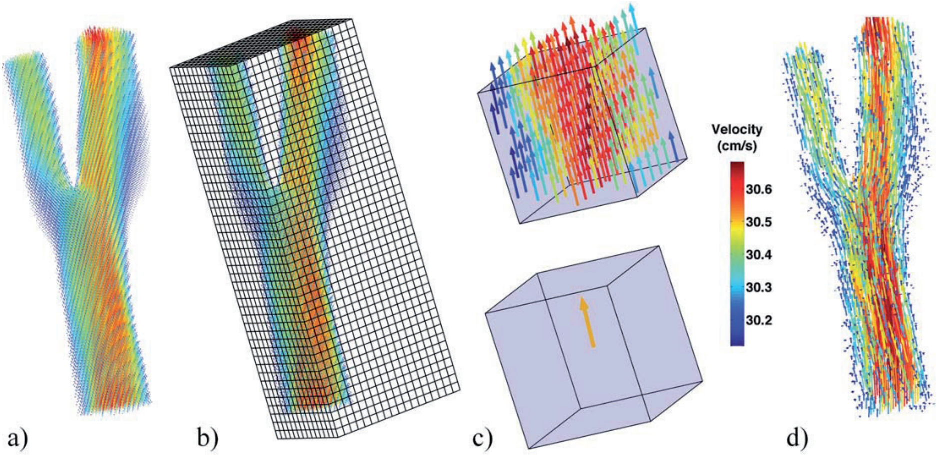

Figure 4. a) CFD velocities interpolated to 0.1mm cube grid, b) The interpolated CFD velocities placed in PC MRI voxels. c) Each voxel contained ~216 of 0.1mm isotropic velocities that were averaged. d) The down-sampled CFD velocities into PC MRI resolution of 0.625 mm.

We present the WSS_{CFD}, WSS_{MRI} and $WSS_{CFDlowres}$ magnitude maps of each artery. We report the mean of WSS_{CFD}, WSS_{MRI} and $WSS_{CFDlowres}$ per artery and also within CCA, ICA and ECA. To check whether a systematic relation exists between WSS_{CFD}, WSS_{MRI} and $WSS_{CFDlowres}$, we plotted mean WSS_{CFD} versus the difference of mean WSS_{MRI} and WSS_{CFD}, and also mean WSS_{CFD} versus the difference of mean WSS_{MRI} and $WSS_{CFDlowres}$ within CCA, ICA and ECA. For the same reason, Bland-Altman analysis, which contained all data points of all arteries, was performed between WSS_{MRI} and WSS_{CFD}, and between WSS_{MRI} and $WSS_{CFDlowres}$. Statistical significance was assessed using paired t-test.

We also compared the location of low, medium and high WSS regions. We labeled all WSS_{MRI} and WSS_{CFD} magnitudes according to three categories representing the low, medium and high tertiles. For each node, we compared the categorization of WSS_{MRI} and WSS_{CFD}. We report the percentage of the nodes having the WSS_{MRI} and WSS_{CFD} values labeled in the same tertile. Note that the nodes on the luminal surface were uniformly distributed; each tertile therefore represented 33% of the total lumen surface area.

WSS directions

We calculated the angles between WSS_{MRI} and WSS_{CFD} vectors for all mesh nodes on the luminal surface. We generated an angle map for all carotid arteries. We report the mean angle of the luminal surface and within the low, medium and high WSS tertiles. Histogram analysis was also performed for the angles that were sorted in three tertiles.

RESULTS

WSS magnitudes

WSS$_{CFD}$, WSS$_{MRI}$ and WSS$_{CFDlowres}$ magnitude maps for nine carotid arteries are shown in Figure 5. The carotid bulb walls were mostly exposed to low WSS magnitude (blue) whereas the bifurcation apex and the inner walls of ICA and ECA had high WSS magnitude (red). Although these patterns were present in WSS$_{CFD}$, WSS$_{MRI}$ and WSS$_{CFDlowres}$ maps, the magnitude of WSS was different in each map. WSS$_{MRI}$ was lower than WSS$_{CFD}$ (0.62±0.18Pa versus 0.88±0.30Pa, $p<0.01$), but was only slightly higher than WSS$_{CFDlowres}$ (0.56±0.18Pa, $p<0.01$). The mean WSS$_{CFD}$, WSS$_{MRI}$ and WSS$_{CFDlowres}$ are presented in Table 1. For higher WSS magnitudes, the difference between the WSS$_{CFD}$ and WSS$_{MRI}$ was larger (R^2= 0.4). Bland-Altman plot presented in Figure 6a shows this trend. Such a trend was absent in the Bland-Altman comparison of WSS$_{MRI}$ and WSS$_{CFDlowres}$ (R^2= 0.01), which is shown in Figure 6b.

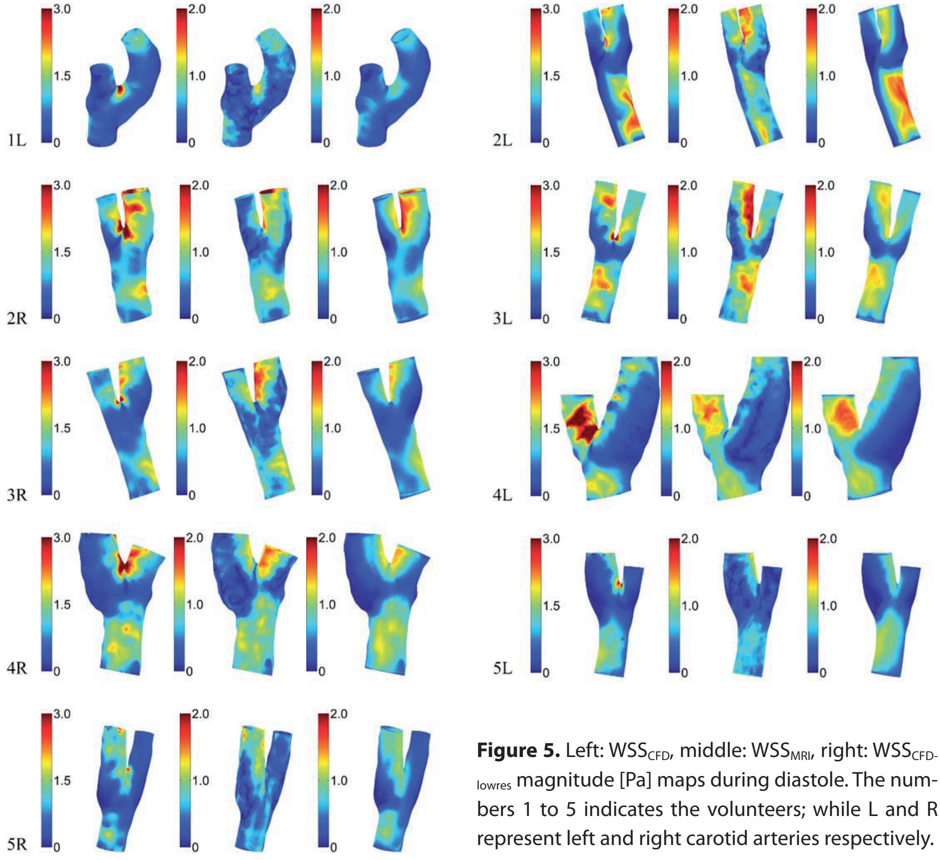

Figure 5. Left: WSS$_{CFD}$, middle: WSS$_{MRI}$, right: WSS$_{CFDlowres}$ magnitude [Pa] maps during diastole. The numbers 1 to 5 indicates the volunteers; while L and R represent left and right carotid arteries respectively.

Table 1. The mean WSS_{CFD}, WSS_{MRI} and $WSS_{CFDlowres}$ [Pa] within CCA, ICA and ECA.

WSS [Pa]	CCA	ICA	ECA
CFD	0.81±0.28	1.07±0.52	1.09±0.46
MRI	0.60±0.17	0.73±0.26	0.56±0.18
CFDlowres	0.57±0.19	0.59±0.24	0.52±0.20

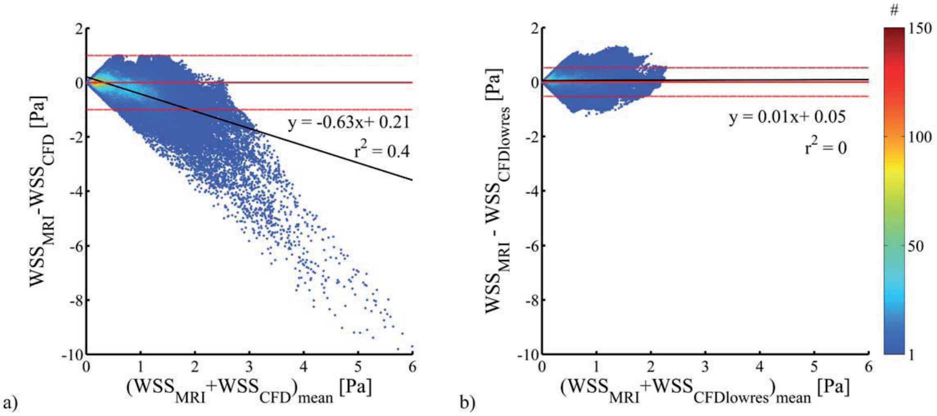

Figure 6. Bland-Altman plots a) between WSS_{MRI} and WSS_{CFD}. b) between WSS_{MRI} and $WSS_{CFDLowres}$. The regression shown in black and the mean and the limits of agreement lines are shown in red. The colors indicate the density of the data points scaled with the colorbar on the right.

Figure 7 shows WSS maps labeled according to the three categories where dark blue, light blue and yellow represent the regions of low, medium and high WSS. The percentage of the WSS_{CFD} and WSS_{MRI} values labeled in the same tertile is presented in Table 2 for each artery. On average, 68.7±4.4% of the low and 69.0±8.9% of the high WSS_{CFD} and WSS_{MRI} values matched.

Table 2. The WSS_{CFD} and WSS_{MRI} match [%] based on division of WSS values into three categories.

[%]	Low WSS tertile	Medium WSS tertile	High WSS tertile
1L	65.3	48.7	69.5
2L	64.1	33.2	57.9
2R	66.5	45.8	70.9
3L	67.9	40.7	54.2
3R	74.7	63.0	84.7
4L	78.0	51.3	67.2
4R	65.3	50.0	78.7
5L	67.4	37.0	65.8
5R	68.9	51.7	72.0
Mean	68.7	46.8	69.0

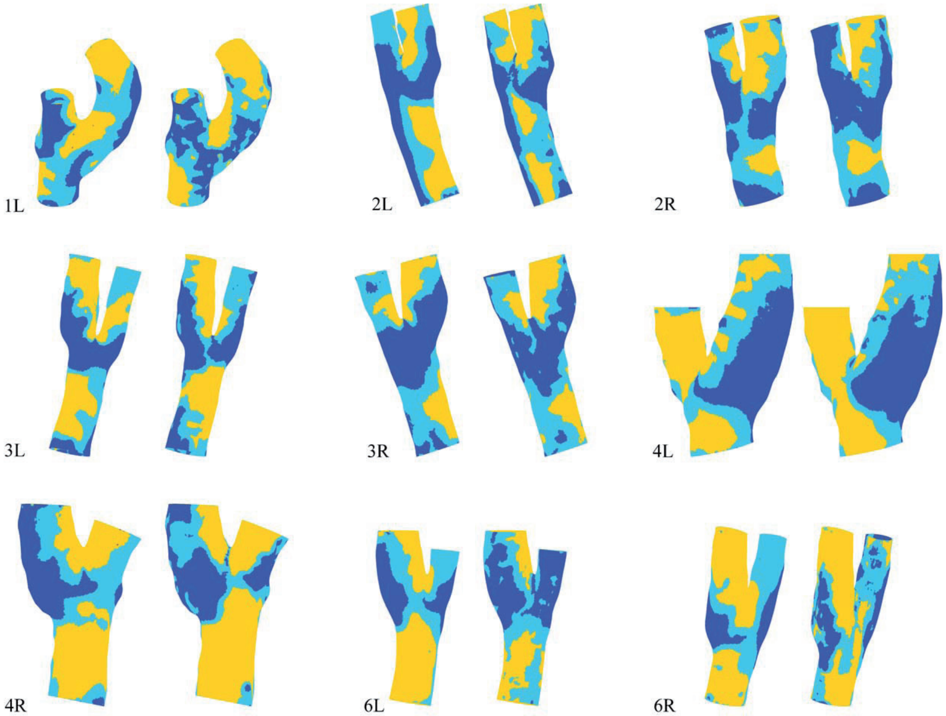

Figure 7. Maps of WSS in the nine carotid arteries where the WSS magnitudes are divided into three categories. Dark blue: low WSS, light blue: medium WSS, yellow: high WSS regions. WSS_{CFD} (left) WSS_{MRI} (right).

WSS directions

The maps of the angles between WSS_{CFD} and WSS_{MRI} vectors are shown in Figure 8. The angles were small inside CCA and at the distal part of the ECA but larger around the carotid bulb and the apex. The mean angle was 65.6±17.4° at low, 28.9±10.0° at medium and 20.3±8.2° at high WSS tertiles. The histograms of the angles that were sorted according to three tertiles are shown in Figure 9. The angle between WSS_{CFD} and WSS_{MRI} vectors was smaller than 30° in 35% of nodes in the low WSS tertile, 67% of the nodes in the medium WSS tertile and 80% of the nodes in the high WSS tertile. Within the low WSS tertile, the angles were larger and varying. We found a particularly large angle of deviation in the proximal ICA of 1L. This seemed to be due to the helical flow pattern seen in the PC MRI data but not in the CFD model. Overall, the mean angle between WSS_{CFD} and WSS_{MRI} vectors was 38.2±9.0°.

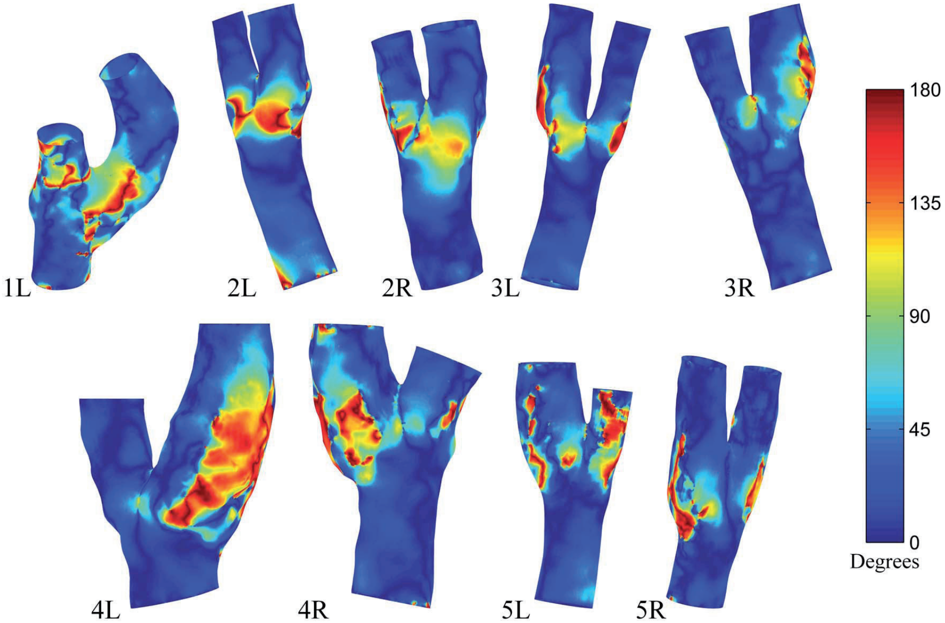

Figure 8. The map of angles [°] between $\mathrm{WSS}_{\mathrm{CFD}}$ and $\mathrm{WSS}_{\mathrm{MRI}}$ vectors throughout the luminal surface.

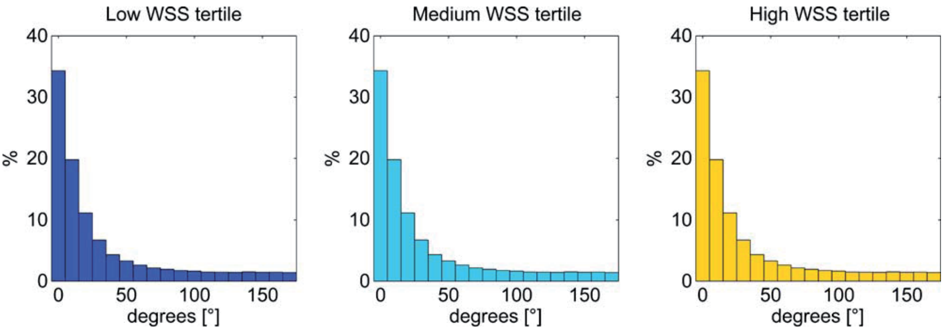

Figure 9. The histograms of the angles [°] between $\mathrm{WSS}_{\mathrm{CFD}}$ and $\mathrm{WSS}_{\mathrm{MRI}}$ vectors within the low, medium and high WSS tertiles.

DISCUSSION

In this study, the WSS vectors based on 3D cine PC MRI measurements and CFD simulations were compared in healthy carotid arteries. The strength of the current study with respect to the previous studies is that we calculated PC MRI-based WSS vectors on the entire 3D luminal surface instead of manually selected planar slices within an artery. Obtaining WSS vectors on the entire 3D luminal surface is essential since WSS distributions in the arteries are heterogeneous and planar slices may not be representative for the entire luminal surface. In that respect, our study is the first to compare subject-specific

WSS distributions based on 3D cine PC MRI velocities with those based on CFD on the 3D lumen surface of the carotid arteries.

Our results showed that the spatial patterns of WSS based on PC MRI were in good agreement with those based on CFD. Regions of low WSS along the carotid bulb and regions of high WSS at the inner walls of ECA and ICA were found by both PC MRI and CFD-based WSS calculations. However, WSS was lower when calculated using PC MRI velocities. By down-sampling the CFD velocity into PC MRI resolution, we were able to mimic the PC MRI velocity field, thereby demonstrating that this underestimation is caused by the limited resolution of PC MRI. We found that the difference between WSS_{CFD} and WSS_{MRI} increases in regions with higher WSS values. This finding indicates that PC MRI underestimates high WSS values more than low WSS values. This is because velocity gradients disappear within a voxel by the averaging effect of PC MRI and the effect is more prominent for higher velocity gradients. Such a trend was not seen for the difference between WSS_{MRI} and $WSS_{CFDlowres}$, demonstrating that the low resolution of the MRI was responsible for the large differences at high WSS.

The directions of the WSS_{CFD} and WSS_{MRI} vectors were also compared. The angles were mainly small in the CCA and at the distal part of ECA because the flows within these segments were mainly in the axial direction of the vessel. We found larger angles also in regions of low WSS and disturbed flows. The large deviation in direction of WSS_{CFD} and WSS_{MRI} vectors in these regions could be due to partial voluming effects and the low signal-to-noise ratio (SNR) of the PC MRI measurements.

The mean WSS values reported in the current study are in agreement with those reported previously. The mean diastolic WSS values reported in the literature were in the range of 0.58-0.61 [Pa] for CCA[10-11] and 0.55-0.70 [Pa] for ICA[12-13], while we found the mean diastolic WSS values in the range of 0.60±0.17 [Pa] for CCA and 0.73±0.26 [Pa] for ICA. Although PC MRI and CFD-based WSS calculations have never been compared for in vivo carotid arteries, such comparison studies were performed for realistic models of carotid arteries[16,33]. These previous studies on carotid phantoms also reported a good qualitative agreement between PC MRI and CFD-based WSS results. Kohler et al showed that PC MRI measurements with an in-plane resolution of 0.7 mm resulted in 40% lower mean WSS values than those predicted by CFD[33]. Papathanasopoulou et al however obtained higher WSS values with PC MRI velocities but they used different segmentations for PC MRI and CFD based calculations[16]. Studies have also compared WSS_{MRI} and WSS_{CFD} for in vivo and in vitro intracranial aneurysms[19,33-36] and found good qualitative agreement between them. Similar to our findings, WSS was underestimated for intracranial aneurysms when calculated using PC MRI and this effect was more prominent for higher WSS values.

Our study showed the validity of the assessment of WSS distribution based on PC MRI by comparing it with CFD based WSS. However, CFD results are also dependent on a number of assumptions and the chosen boundary conditions which may not reflect in vivo situation. In that respect, by showing a good agreement between PC MRI based WSS and WSS based on the down-sampled CFD velocities, we can also interpret our results as the validation of subject-specific CFD based WSS calculation using PC MRI measurements. Thus, with the high correlation between the two methods, it can safely be stated that the chosen boundary conditions and assumptions of CFD result in in-vivo WSS distribution at diastole.

There were three main limitations of our study design. Firstly, we compared WSS_{CFD} and WSS_{MRI} values during diastole only. This is a direct result of the choice for increased spatial resolution of the PC MRI measurements at the expense of temporal resolution. During our PC MRI scans, we recorded the velocities with a temporal resolution of 138±11ms, which is low compared to literature[20,37]. Due to the limited temporal resolution, we were unable to capture the large fluctuations in flow that are known to occur especially during systole. For that reason, we decided not to compare the systolic data. Since the analysis was performed at a single time step, time dependent hemodynamic parameters such as oscillatory shear index (OSI) were not computed. To analyze PC MRI based WSS calculations during systole and to obtain time dependent parameters, higher temporal resolution will be required in future studies. Secondly, by assuming rigid walls, we neglected the pulsatility of carotid arterial walls in our CFD simulations. However, we segmented the vessel walls on the diastolic images and we compared the WSS_{CFD} and WSS_{MRI} values only during diastole. We assume that the use of rigid walls therefore had a limited impact on our calculations. Finally, we used the diastolic spatial velocity profile shapes within the CCA and ICA throughout the cardiac cycle. As a result, we were unable to capture the helical flow that we observed in PC MRI data of carotid artery 1L in our CFD model. Acquisition of PC MRI data in higher temporal resolution and applying time varying velocity profiles as boundary conditions in the CFD simulations may prevent this limitation in future studies.

Clinical relevance

Spatial WSS patterns strongly affect endothelial cell signaling and early events in atherosclerosis[1-7]. These patterns were estimated similarly by PC MRI and CFD based calculations. For that reason, both WSS measures can be used when knowledge of low and high WSS patterns is sufficient. WSS was however underestimated when calculated using PC MRI due to the limited spatial resolution of PC MRI. Increasing the spatial resolution of PC MRI measurements may have been a remedy for reducing underestimation of WSS. However, it would have also decreased SNR and increased the scan duration dramatically. The future developments in MRI technology may allow PC MRI measurements in higher spatial resolution within reasonable time frames and as a result of this, underestimation of PC MRI based WSS may reduce in the future studies. Despite this limitation, PC MRI based WSS calculations were completed within shorter time frames (~15 minutes versus ~15 hours per artery) by using a simpler method that is easily applicable to the acquired MR images. These advantages may make 3D cine PC MRI data an attractive candidate for calculating WSS magnitudes in clinical practice in future.

It should be noted that in the low WSS regions we found large angles between the CFD and PC MRI-based WSS vectors. In the carotid arteries, particular locations such as carotid bulb are exposed to low and also oscillatory WSS. Some studies have suggested that oscillatory shear can induce proatherogenic effects on endothelial cells[32]. It may therefore be necessary to obtain accurate WSS directions also in the regions of low WSS and may limit the use of PC MRI-based WSS calculations. The use of a variable encoding velocity over the heart cycle[38] or the use of a dual encoding velocity in combination with accelerated imaging[39] may improve PC MRI measurements also at regions of low velocity such that, direction of WSS vectors is decently monitored and can also be used to estimate the degree of changes over the cardiac cycle.

CONCLUSIONS

We showed that PC MRI-based WSS magnitudes are lower than those based on CFD. This is mainly due to the limited spatial resolution of PC MRI measurements. However, we observed good agreement between high and low WSS_{CFD} and WSS_{MRI} patterns and also between the directions of the WSS vectors in the high WSS regions. Although the PC MRI based WSS calculation method has some limitations, it has the potential to be applied in the clinical assessment of WSS in carotid arteries since it is simpler and easily applicable to the acquired images compared to the current reference standard CFD.

REFERENCES

[1] Malek AM, Alper SL, Izumo S. Hemodynamic Shear Stress and Its Role in Atherosclerosis. JAMA. 1999; 282(21): 2035–2042.

[2] VanderLaan PA, Reardon CA, Getz GS. Site specificity of atherosclerosis: site-selective responses to atherosclerotic modulators. Arterioscler, Thromb, Vasc Biol. 2004; 24(1): 12–22.

[3] Shaaban AM, Duerinckx AJ. Wall shear stress and early atherosclerosis: a review. AJR. 2000; 174(6): 1657–65.

[4] Slager CJ, Wentzel JJ, Gijsen FJH, Thury A, van der Wal AC, Schaar JA, Serruys PW. The role of shear stress in the destabilization of vulnerable plaques and related therapeutic implications. Nature clinical practice. Cardiovascular medicine. 2005; 2(9): 456–64.

[5] Cecchi E, Giglioli C, Valente S, Lazzeri C, Gensini GF, Abbate R, Mannini L. Role of hemodynamic shear stress in cardiovascular disease. Atherosclerosis. 2011; 214(2): 249–56.

[6] Wentzel JJ, Corti R, Fayad ZA, Wisdom P, Macaluso F, Winkelman MO, Fuster V, Badimon JJ. Does shear stress modulate both plaque progression and regression in the thoracic aorta? Human study using serial magnetic resonance imaging. J Am Coll Cardiol. 2005; 45(6): 846–54.

[7] Pfeiffer V, Sherwin SJ, Weinberg PD. Does low and oscillatory wall shear stress correlate spatially with early atherosclerosis? A systematic review. Cardiovasc Res. 2013; 99(2): 242-50.

[8] Shojima M, Oshima M, Takagi K, Torii R, Hayakawa M, Katada K, Morita A, Kirino T. Magnitude and role of wall shear stress on cerebral aneurysm: computational fluid dynamic study of 20 middle cerebral artery aneurysms. Stroke. 2004; 35(11): 2500–5.

[9] Oshinski JN, Ku DN, Mukundan S, Loth F, Pettigrew RI. Determination of wall shear stress in the aorta with the use of MR phase velocity mapping. JMRI. 1995; 5(6): 640–7.

[10] Oyre S, Ringgaard S, Kozerke S, Paaske WP, Erlandsen M, Boesiger P, Pedersen EM. Accurate noninvasive quantitation of blood flow, cross-sectional lumen vessel area and wall shear stress by three-dimensional paraboloid modeling of magnetic resonance imaging velocity data. J. Am. Coll. Cardiol. 1998; 32(1):128–34.

[11] Sui B, Gao P, Lin Y, Qin H, Liu L, Liu G. Noninvasive determination of spatial distribution and temporal gradient of wall shear stress at common carotid artery. J Biomech. 2008; 41(14): 3024-30.

[12] Sui B, Gao P, Lin Y, Gao B, Liu L, An J. Blood flow pattern and wall shear stress in the internal carotid arteries of healthy subjects. Acta Radiol. 2008; 49(7): 806-14.

[13] van Es AC, van der Flier WM, Box FM, Middelkoop HA, Westendorp RG, van Buchem MA, van der Grond J. Carotid and basilar artery wall shear stress in Alzheimer's disease and mild cognitive impairment. Dementia and geriatric cognitive disorders. 2009; 28(3): 220-4.

[14] Masaryk AM, Frayne R, Unal O, Krupinski E, Strother CM. In vitro and in vivo comparison of three MR measurement methods for calculating vascular shear stress in the internal carotid artery. AJNR.1999; 20(2): 237–45

[15] Stokholm R, Oyre S, Ringgaard S, Flaagoy H, Paaske WP, Pedersen EM. Determination of wall shear rate in the human carotid artery by magnetic resonance techniques. Eur J Vasc Endovascular Surg. 2000; 20(5): 427–33.

[16] Papathanasopoulou P, Zhao S, Köhler U, Robertson MB, Long Q, Hoskins P, Xu XY, Marshall I. MRI measurement of time-resolved wall shear stress vectors in a carotid bifurcation model, and comparison with CFD predictions. JMRI. 2003; 17(2): 153–62.

[17] Stalder AF, Russe MF, Frydrychowicz A, Bock J, Hennig J, Markl M. Quantitative 2D and 3D phase contrast MRI: optimized analysis of blood flow and vessel wall parameters. Magn Reson Med. 2008; 60(5): 1218–31.

[18] Frydrychowicz A, Stalder AF, Russe MF, Bock J, Bauer S, Harloff A, Berger A, Langer M, Hennig J, Markl M. Three-dimensional analysis of segmental wall shear stress in the aorta by flow-sensitive four-dimensional-MRI. JMRI. 2009; 30(1): 77–84.

[19] Van Ooij P, Potters WV, Guédon A, Schneiders JJ, Marquering HA, Majoie CB, vanBavel E, Nederveen AJ. Wall shear stress estimated with phase contrast MRI in an in vitro and in vivo intracranial aneurysm. JMRI. 2013; 38(4): 876-84

[20] Harloff A, Berg S, Barker AJ, Schöllhorn J, Schumacher M, Weiller C, Markl M. Wall shear stress distribution at the carotid bifurcation: influence of eversion carotid endarterectomy. Eur. Radiol. 2013: 23(12); 3361-9.

[21] Potters W, Van Ooij P, Marquering H, vanBavel E, Nederveen AJ. Volumetric arterial wall shear stress calculation based on cine phase contrast MRI. JMRI. 2014: 1-12.

[22] Yushkevich PA, Piven J, Hazlett HC, Smith RG, Ho S, Gee JC, Gerig G. User-guided 3D active contour segmentation of anatomical structures: Significantly improved efficiency and reliability. Neuroimage. 2006; 31(3): 1116-28.

[23] Antiga L, Piccinelli M, Botti L, Ene-Iordache B, Remuzzi A, Steinman DA. An image-based modeling framework for patient-specific computational hemodynamics. Med Biol Eng Comput. 2008; 46(11): 1097–112.

[24] Lee SW, Antiga L, Spence JD, Steinman DA. Geometry of the carotid bifurcation predicts its exposure to disturbed flow. Stroke. 2008; 39(8): 2341–7.

[25] Seo T, Schachter LG, Barakat AI. Computational Study of Fluid Mechanical Disturbance Induced by Endovascular Stents. Annals of Biomedical Engineering. 2005; 33(4): 444–456.

[26] Petersson S, Dyverfeldt P, Ebbers T. Assessment of the accuracy of MRI wall shear stress estimation using numerical simulations. JMRI. 2012; 36(1): 128–38.

[27] Markl M, Wegent F, Zech T, Bauer S, Strecker C, Schumacher M, Cornelius W, Hennig J, Harloff A. In vivo wall shear stress distribution in the carotid artery: effect of bifurcation geometry, internal carotid artery stenosis, and recanalization therapy. Circ Cardiovasc imaging. 2010; 3(6): 647–55.

[28] Augst AD, Ariff B, McG. Thom SAG, Xu XY, Hughes AD. Analysis of complex flow and the relationship between blood pressure, wall shear stress, and intima-media thickness in the human carotid artery. Am J Physiol Heart Circ Physiol. 2007; 293(2): H1031–7.

[29] Marshall I. Computational simulations and experimental studies of 3D phase-contrast imaging of fluid flow in carotid bifurcation geometries. JMRI. 2010; 31(4): 928–34.

[30] Markl M, Wallis W, Harloff A. Reproducibility of flow and wall shear stress analysis using flow-sensitive four-dimensional MRI. JMRI. 2011; 33(4): 988–94.

[31] Box FMA, van der Geest RJ, Rutten MCM, Reiber JHC. The influence of flow, vessel diameter, and non-newtonian blood viscosity on the wall shear stress in a carotid bifurcation model for unsteady flow. Investigative radiology. 2005; 40(5): 277–94.

[32] Conway DE, Williams MR, Eskin SG, McIntire LV. Endothelial cell responses to atheroprone flow are driven by two separate flow components: low time-average shear stress and fluid flow reversal. Am J Physiol Heart Circ Physiol. 2010; 298: H367-H374

[33] Kohler U, Marshall I, Robertson MB, Long Q, Xu YX, Hoskins PR. MRI measurement of wall shear stress vectors in bifurcation models and comparison with CFD predictions. JMRI. 2001; 14: 563–573.

[34] Boussel L, Rayz V, Martin A, Acevedo-Bolton G, Lawton MT, Higashida R, Smith WS, Young WL, Saloner D. Phase-contrast magnetic resonance imaging measurements in intracranial aneurysms in vivo of flow patterns, velocity fields, and wall shear stress: comparison with computational fluid dynamics. Magn Reson Med. 2009; 61(2): 409–417.

[35] Isoda H, Ohkura Y, Kosugi T, Hirano M, Alley MT, Bammer R, Pelc NJ, Namba H, Sakahara H. Comparison of hemodynamics of intracranial aneurysms between MR fluid dynamics using 3D cine phase-contrast MRI and MR-based computational fluid dynamics. Neuroradiology. 2010; 52(10): 913–920.

[36] Naito T, Miyachi S, Matsubara N, Isoda H, Izumi T, Haraguchi K, Takahashi I, Ishii K, Wakabayashi T. Magnetic resonance fluid dynamics for intracranial aneurysms--comparison with computed fluid dynamics. Acta Neurochir (Wien). 2012; 154(6): 993–1001.

[37] Schubert T, Santini AF, Stalder AF, Bock J, Meckel S, Bonati L, Markl M, Wetzel S. Dampening of blood-flow pulsatility along the carotid siphon: does form follow function? Am J Neuroradiol. 2011; 32(6): 1107-12.

[38] Nilsson A, Bloch KM, Carlsson M, Heiberg E, Stahlberg F. Variable velocity encoding in a three-dimensional, three-directional phase contrast sequence: Evaluation in phantom and volunteers. JMRI. 2012; 36(6): 1450-9.

[39] Giese D, Kabbasch C, Hedderich D, Maintz D, Liebig T, Bunck A. The use of k-t PCA accelerated dual venc 3D flow MRI to assess hemodynamics before and after flow diverting stent implantation in cerebral aneurysm models. Journal of Cardiovascular Magnetic Resonance. 2014, 16 (Suppl 1): W29.

Chapter 3

Relation between wall shear stress and carotid artery wall thickening MRI versus CFD

Based on:

Cibis, M, Potters, W, Selwaness, M, Gijsen, FJ, Franco, O, Lorza, AMA, van der Lugt, A, Nederveen, AJ, Wentzel, JJ, Relationship between wall shear stress and carotid artery wall thickening MRI vs CFD. Submitted.

ABSTRACT

Wall shear stress (WSS), a parameter associated with endothelial function, is calculated by computational fluid dynamics (CFD) or phase contrast (PC) MRI measurements. Although CFD is common in WSS (WSS_{CFD}) calculations, PC MRI-based WSS (WSS_{MRI}) is more favorable in population studies; since it is straightforward and less time consuming. However, it is not clear if WSS_{MRI} and WSS_{CFD} show similar associations with vascular pathology. Our aim was to test the associations between wall thickness (WT) of the carotid arteries and WSS_{MRI} and WSS_{CFD}. The subjects (n=14) with an asymptomatic carotid plaque who underwent MRI scans two times within 4 years of time were selected from The Rotterdam Study. We compared WSS_{CFD} and WSS_{MRI} at baseline and follow-up. Baseline WSS_{MRI} and WSS_{CFD} values were divided into 3 categories representing low, medium and high WSS tertiles. WT of each tertile was compared by a one-way ANOVA test. The WSS_{MRI} and WSS_{CFD} were 0.50±0.13Pa and 0.73±0.25Pa at baseline. Although WSS_{MRI} was underestimated, a good regression was found between WSS_{MRI} and WSS_{CFD} (r^2=0.71). No significant difference was found between baseline and follow-up WSS in both CFD and MRI-based calculations. The WT at baseline was 1.36±0.16mm and did not change over time. The WT was 1.55±0.21mm in low, 1.33±0.20mm in medium and 1.21±0.21mm in the high WSS_{MRI} tertiles. Similarly, the WT was 1.49±0.21mm in low, 1.33±0.20mm in medium and 1.26±0.21mm in high WSS_{CFD} tertiles. We found that WSS_{MRI} and WSS_{CFD} were inversely related with WT. WSS_{MRI} and WSS_{CFD} patterns were similar although MRI-based calculations underestimated WSS.

INTRODUCTION

Atherosclerotic plaques are preferentially located at the bifurcations and the inner curves of the vasculature, co-localizing with regions of low wall shear stress (WSS)[1-2]. While high WSS induces an athero-protective environment, low WSS results in an athero-prone endothelial phenotype hence early arterial wall thickening initiates at the regions of low WSS[3-7].

WSS is calculated by multiplying the dynamic viscosity of blood with the spatial gradient of blood velocities perpendicular to the vessel wall. Assuming that the dynamic viscosity of blood is known, WSS can be determined using the velocities near the vessel wall. Blood velocities are generally calculated by computational fluid dynamics (CFD) simulations, which solve the Navier-Stokes equations iteratively. However, CFD requires accurate boundary conditions, non clinical expertise and long computational time. The blood velocities can alternatively be obtained by phase contrast MRI (PC MRI). It has been shown that WSS calculations using PC MRI velocity measurements underestimate the magnitude of WSS due to the limited spatial resolution of MRI[8,9]. However, MRI-based WSS calculations result in spatial WSS patterns similar to those obtained with CFD[8]. One can expect that the agreement between MRI and CFD-based WSS reduces in large population studies since MR image quality is lower due to sub-optimal scan parameters which were chosen to keep scan time clinically feasible. In addition, the quality might be lower since the MRI scans are not performed with the latest equipment to maintain consistency between baseline and follow-up measurements in long-term follow-up studies. In such a setting, the accuracy of MRI based WSS might be lower. However, MRI-based WSS calculations are more advantageous in large population studies and in routine clinical practice since they are straightforward and less time consuming than CFD-based WSS calculations.

Despite the lower accuracy of MRI-based WSS in a population-based setting, MRI can still be used for estimating WSS if MRI-based WSS calculations would illustrate the associations between vascular pathology and WSS similar to those based on CFD calculations. Previous studies have shown that there is an inverse relation between wall thickness and WSS during early wall thickening[10-12]. The aim of this study was to test if this inverse relation between WSS and the wall thickness of the carotid arteries during early wall thickening is found similarly by MRI and CFD-based calculations. The similarity of associations between MRI and CFD-based calculations would indicate the potential use of MRI in WSS calculations within a population-based setting. We chose a subgroup of subjects from a large cohort study and we calculated MRI-based WSS (WSS_{MRI}) and CFD-based WSS (WSS_{CFD}). The subgroup consisted of elderly subjects with an asymptomatic carotid plaque at baseline (t=0) who underwent two MRI scan sessions within a follow-up period of ~4 years.

METHODS

Patient Selection

The data for this work was retrospectively selected from a cohort study (Rotterdam-Study) that investigated the prevalence and the risk factors of chronic diseases in an elderly healthy population at 45 years of age or over[13]. In the Rotterdam-Study, subjects underwent a 2D ultrasound carotid artery scan and those with wall thickness larger than 2.5 mm in at least one of the carotid arteries were admitted to MR imaging of their carotid arteries[13]. The procedure of the study was reviewed and approved by the Medical Ethics Committee. From this study, we selected sub-group of subjects (n=15) that had an atherosclerotic plaque at baseline in the left carotid artery. The selected images were without visible MR artifacts (fold-over artifacts, movement artifacts, and velocity aliasing) and phase offset errors.

MRI Scanning

The MRI scans were obtained by a 1.5T MR Scanner (GE Signa Excite II; GE Healthcare, Milwaukee, WI, USA) using a bilateral phased-array surface coil (Machnet, Eelde, the Netherlands). The subjects were positioned with the neck extended to improve coil positioning. The scan protocol included, among other sequences, proton-density weighted echo planar imaging (PDw-EPI) (FOV: 13x7cm^2, in-plane resolution: 0.51mm, slice thickness: 1.2mm, TR/TE: 12000ms/24.3ms, scan time: 4:00min:sec) and 3D untriggered PC MRI (FOV: 18x18cm^2, in-plane resolution: 0.70mm, slice thickness: 1.0mm, TR/TE: 13ms/4.3ms, scan time: 6:13min:sec, VENC: 60x60x60cm/s) with three directional velocity encoding. The examples of the anatomical images obtained with PDw-EPI and the complex difference images obtained with 3D PC MRI are shown in Figure 1. PDw-EPI images were used to obtain the lumen and the wall geometry. The absolute values of the time-averaged velocities in 3 directions were extracted from the complex difference PC MR images.

Preprocessing

The phase offset errors were checked by using the velocities measured in the static muscle tissue around the carotid arteries. The PDw-EPI and PC MR images were registered (rigid registration, six degrees of freedom) to each other using an open source registration tool, Elastix[14]. After the registration, the outer wall and the lumen surface of the left carotid arteries at baseline and follow-up were segmented manually on the PDw-EPI images using the open source segmentation tool ITK-SNAP[15]. The lumen surfaces of the baseline and follow-up were then converted to volumetric meshes using Gambit (ANSYS). The size of tetrahedral elements was gradually increased inwards from 0.15 mm at the luminal surface, which resulted in 800.000 elements per artery on average. WSS_{CFD} and WSS_{MRI} calculations were performed using identical volumetric meshes.

WSS calculations based on MRI measurements

The workflow of WSS_{MRI} calculation is briefly discussed here since it was described in more detail elsewhere[16]. Firstly, the inward normal, i.e. a vector perpendicular to the vessel wall in the direction of the vessel lumen center of each mesh point at the lumen surface was obtained. The direction of the velocities measured by MRI was corrected if necessary (see Appendix). On the inward normal, the velocities were interpolated at 2 points, which were at a distance of 1.25 and 2.5 mm from the mesh point at the lumen surface. The blood velocity was set to zero at the mesh point at the lumen surface and a smoothing spline curve was fit to these three velocities. We calculated wall shear rate (WSR) by taking the gradient of the smoothing spline curve at the lumen surface. Finally, WSS was calculated by multiplying WSR with the blood viscosity, which was determined by applying the Carreau-Yasuda model using the parameters as in[17].

WSS calculations based on CFD calculations

For the WSS_{CFD} calculations, the velocity profile at the inlet of the common carotid artery (CCA) was used as it was measured. For the outflow conditions, the measured flows at the outlets of internal carotid artery (ICA) and external carotid artery (ECA) were corrected by multiplying with a constant so that the sum of outflow was equal to the CCA inflow. The corrected ICA velocity profile was implemented as a boundary condition of ICA outlet and ECA outlet was left stress-free. The fluid density was set to 1060 kg/

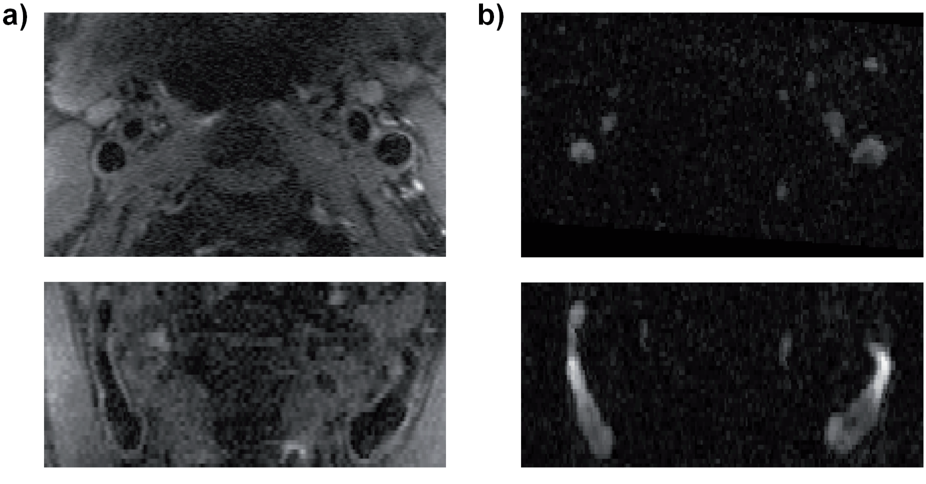

Figure 1. Typical a) PDw-EPI b) 3D time-averaged PC MRI complex difference images in axial (top) and coronal (bottom) view

m^3 and the viscosity was defined with the Carreau-Yasuda model as in the calculations based on MRI[17]. Steady state CFD simulations were performed using the commercial finite element software FIDAP 8.7.4 (ANSYS) on a standard desktop computer (Intel Xeon six core processor, 2.40 GHz CPU and 12 GB RAM). One CFD simulation took ~1 hour. WSS_{CFD} at each lumen mesh point was calculated by the post-processing tool of FIDAP.

Post-processing and analysis

By using the segmentations of the lumen and the outer wall, the lumen area and the normalized wall index (defined as wall area/ (lumen area + wall area) of CCA and ICA were calculated. The wall thickness (WT) was calculated at each lumen mesh point by calculating the shortest distance between the lumen mesh point and the outer wall. After WSS was calculated (figure 2a), the carotid bifurcation was divided into three parts: CCA, ICA and ECA. These parts were partitioned into patches by 8 circular segments (45°) and 2 mm longitudinal segments by using the vascular modeling Toolkit (VMTK version 1.0.0)[18] as shown in figure 2b and this resulted in approximately 120 patches per artery. Subsequently, the patches were flattened (figure 2c). The ECA was excluded from the analysis. The ICA and CCA were analyzed together. WSS_{CFD} and WSS_{MRI} were calculated at baseline and follow-up. Baseline WSS_{MRI} and WSS_{CFD} were compared by Bland-Altman analysis. We investigated the correlations between the baseline WT and the baseline WSS_{MRI}, and between the baseline WT and WSS_{CFD} by linear regression analysis. The WSS values of the patches were divided into three categories representing the low, medium and high WSS tertiles. The corresponding mean WT for each WSS category (low, medium, high) were calculated and compared to each other (one-way ANOVA, post hoc test). Finally, we compared the baseline and follow-up WSS_{MRI}. The comparison of the WSS calculation methods and the changes in the geometry over time were tested by using a two-sided paired t-test. $P<0.05$ was considered significant.

RESULTS

Population Characteristics

One carotid artery was excluded from the analysis due to large inflow-outflow imbalance after phase offset corrections. The average phase offset error for the remaining 14 subjects at baseline was 0.6 ± 0.6 cm/sec. The mean age of the subjects was 73.4 ± 6.8 years and the mean follow-up period was 4.3 ± 0.1 years (Table 1). A plaque, defined as maximum wall thickness larger than 2.5 mm on MRI[13], was present in the left carotid artery of all subjects at baseline (Table 2). No significant changes were found in lumen area, WSS_{MRI}, WSS_{CFD} or in WT over time.

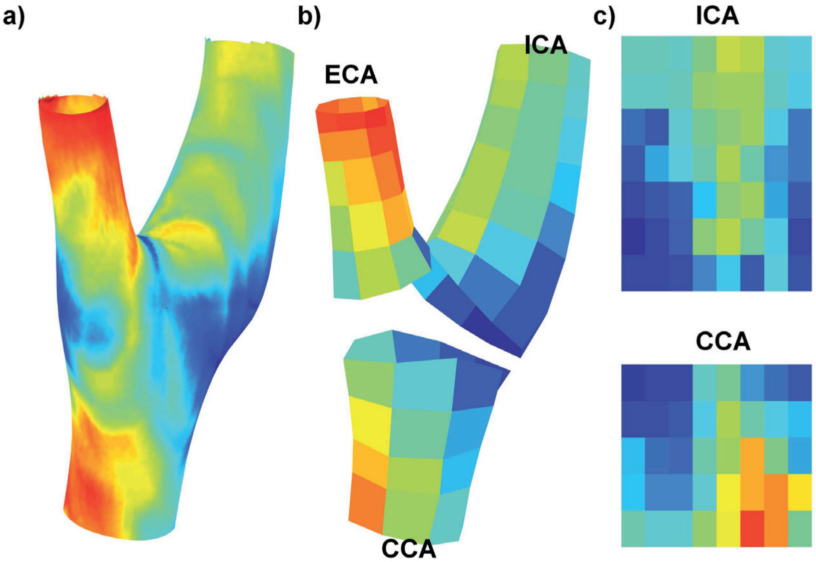

Figure 2. a) An example of WSS distribution based on PC MRI b) The carotid bifurcation was divided into three parts: CCA, ECA and ICA. These parts were partitioned into patches by 8 circular segments (45°) and 2 mm longitudinal segments resulting in approximately 120 patches per artery. c) These patches were flattened. CCA and ICA data were analyzed. ECA was excluded from the analysis.

Table 1. Baseline characteristics of the subjects (n=14).

Baseline characteristics	n=14
Male	7 (50%)
Age (years)	73.4±6.8
Follow-up period (years)	4.3±0.1
BMI	25.5±2.4
Smoking ever	10 (71%)
HDL (mmol/l)	1.5±0.4
Total cholesterol (mmol/l)	5.7±0.5
Systolic blood pressure (mm Hg)	141±20
Diastolic blood pressure (mm Hg)	76±10
Stroke	1(7%)

Table 2. Mean WSS based on MRI and CFD and mean WT at baseline and follow-up (n=14)

	Baseline	Follow-up	p-value
Lumen area CCA [mm^2]	39.7±8.6	38.3±9.1	0.22
Lumen area ICA [mm^2]	32.7±11.9	31.6±11.7	0.52
Normalized Wall Index CCA	0.49±0.05	0.49±0.04	0.63
Normalized Wall Index ICA	0.49±0.08	0.52±0.08	0.02
Mean WT [mm]	1.36±0.16	1.46±0.28	0.10
WSS_{MRI} [Pa]	0.50±0.13	0.47±0.10	0.18
WSS_{CFD} [Pa]	0.73±0.25	0.78±0.33	0.20

WSS$_{MRI}$ vs. WSS$_{CFD}$ at baseline

At baseline, the mean WSS$_{MRI}$ and WSS$_{CFD}$ were 0.50±0.13Pa and 0.73±0.25Pa respectively. Despite underestimation, a high regression relation (r^2 =0.71) was found between mean WSS$_{MRI}$ and mean WSS$_{CFD}$ (figure 3a). Figure 3b shows the Bland-Altman plots of WSS$_{MRI}$ and WSS$_{CFD}$ obtained from all patches of all subjects. In one to one comparison of the patches, we observed that WSS$_{MRI}$ was underestimated more at higher WSS values. The colors indicate the density of the data points scaled with the color bar on the right.

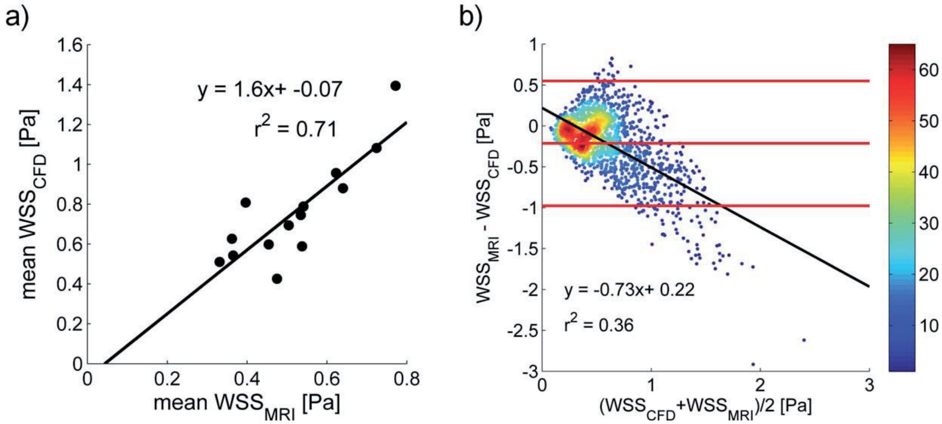

Figure 3. a) Regression between mean WSS$_{MRI}$ and mean WSS$_{CFD}$ b) Bland-Altman plots of WSS$_{MRI}$ and WSS$_{CFD}$ obtained from all patches of all subjects. Red lines indicate the 95% confidence interval. The colors of the data points indicate the density of the data points scaled with the color bar on the right.

Baseline versus Follow-up WSS

A high regression relation was found between the MRI-based WSS$_{B}$ and WSS$_{FUP}$ (r^2=0.66) and between CFD-based WSS$_{B}$ and WSS$_{FUP}$ (r^2= 0.86). The Bland-Altman plot analysis of WSS$_{B}$ and WSS$_{FUP}$ obtained from all patches of all subjects is presented in Figure 4.

Wall thickness and baseline WSS

We found a significant inverse relation between WSS$_{MRI}$ and WT in 12 out of 14 individual subjects (r^2: 0.05 to 0.49, $p<0.02$) and the relation was not significant in 2 individual subjects. A similar significant inverse relationship was found between WSS$_{CFD}$ and WT in 11 out of 14 subjects (r^2: 0.04 to 0.36, $p <0.03$). The mean WT of the entire group was 1.36±0.16 mm at baseline. The mean WT of each WSS tertile was significantly different, and we found an inverse relationship between the WSS categories and the mean WT of each WSS category (figure 5). The mean WT was 1.55±0.21 mm in low, 1.33±0.20 mm in medium and 1.21±0.21 mm in the high WSS$_{MRI}$ tertiles. Similarly, the mean WT was 1.49±0.21 mm in low, 1.33±0.20 mm in medium and 1.26±0.21 mm in high WSS$_{CFD}$ tertiles.

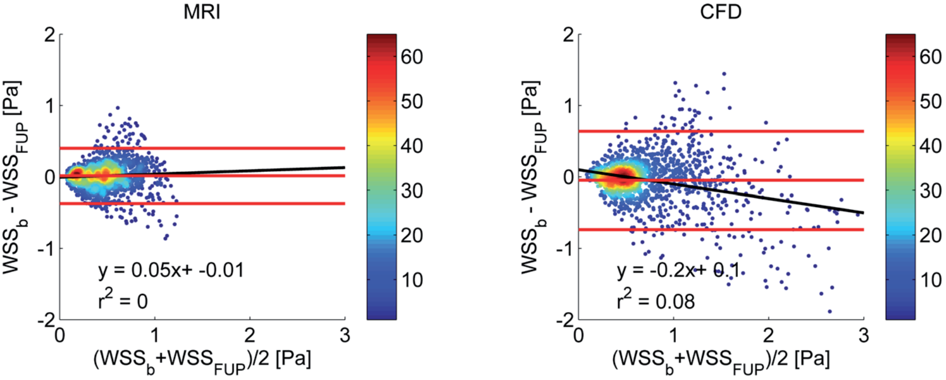

Figure 4. Bland Altman plots of baseline and follow-up WSS_{MRI} [Pa] and WSS_{CFD} [Pa]. Red lines indicate the 95% confidence interval. The colors of the data points indicate the density of the data points scaled with the color bar on the right.

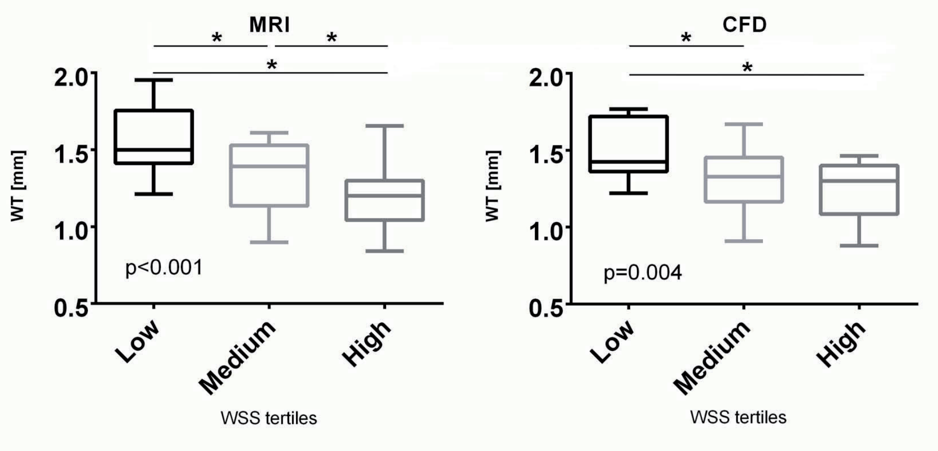

Figure 5. Low, medium and high WSS categories and the corresponding WT [mm]. Left column: categories based on WSS_{MRI}, right column: categories based on WSS_{CFD}. Significance differences between groups are shown by (*) sign.

DISCUSSION

In this study, we evaluated the association of WSS with wall thickness in 14 elderly subjects having asymptomatic plaques in the carotid arteries. We calculated WSS using two methods: 1) CFD simulations 2) PC MRI measurements. Our aim was to test if WSS_{MRI} and WSS_{CFD} were similarly associated with the wall characteristics. Although several studies have previously compared MRI and CFD-based WSS calculations in carotid phantoms[19,20] and also in vivo and in vitro in intracranial aneurysms[21-23], to our knowledge, the associations of WSS_{MRI} and WSS_{CFD} with wall thickness have never been compared in the same group of individuals. We believe that the similar associations that we found using PC MRI and CFD showed the robustness of both methods which was not shown previously.

MRI-based calculations underestimated WSS relative to CFD-based calculations mainly due to the limited resolution of MRI. WSS_{MRI} was underestimated more at regions of higher WSS values due to the averaging effect of PC MRI measurements. WT had a significant inverse relationship to both WSS_{CFD} and WSS_{MRI} which suggests that both methods are capable of finding similar associations between WSS and the wall parameters regardless of the differences in the WSS magnitude and the WSS pattern. No significant changes were observed in mean WSS over time which was expected since the lumen area and also the wall thickness did not change during the follow-up time. Local variations were observed in WSS over time which might be caused by the natural variation of the flow over time and by the measurement errors. Since MRI-based calculations underestimate WSS, the small changes in WSS might not be detected by the MRI-based longitudinal studies.

Several studies have been performed to determine the associations between WSS and wall thickness of carotid arteries[3,4,12,24-31]. WSS calculations inside carotid arteries were based on 3 methods: 1) ultrasound velocity measurements 2) PC MRI velocity measurements and 3) CFD simulations. Only a few studies used PC MRI velocity measurements, but the majority of the studies used ultrasound for this purpose. In general, the studies showed an inverse relation between WSS and wall thickness. Duivenvoorden et al[12] was one of the few that performed PC MRI measurements to calculate WSS. They included fifteen young (age 25.9±2.6), fifteen old volunteers (age 57.4±3.2) and fifteen patients (age 63.3±9.8) with cardiovascular heart disease. They determined mean WSS and WT at a single plane through the common carotid artery at a predefined distance below the flow divider. Similar to our findings they found an inverse relation between averaged WSS and arterial wall thickness. The strength of our study is that we calculated volumetric WSS distribution based on 3D PC MRI measurements in the whole artery by using patches. Our analysis therefore did not suffer from selection bias based on cross-sections.

Lee et al[24] performed duplex ultrasound measurements in hypertensive patients and in a control group. They did not find a significant correlation between intima-media thickness (IMT) and WSS in CCA. This was probably caused by the fact that they included only CCA in their analysis. CCA is the straight part of the carotid artery. Therefore, WSS and wall thickening are more uniform in CCA relative to carotid bifurcation. Jiang et al[25] found an inverse relation between IMT and WSS based on echo-Doppler examinations in a hypertensive patent group. Irace et al[11] also scanned two hundred eight patients with echo-Doppler and measured systolic blood velocity at a single location inside the artery. They divided the patients according to the cardiac heart disease risk factors into low and high-risk groups and found a negative correlation between IMT and WSS only in the low-risk group. Carallo et al[26], Kornet et al[27] and Gnasso et al[10] also found an inverse relation based on ultrasound measurements. Steinman et al[29] examined 2 subjects with MRI including PC MRI acquisition and calculated WSS based on CFD. They observed that regions of low WSS coincide with the plaque regions, but they did not find a quantitative relationship between wall thickness and WSS. Augst et al[30] examined healthy volunteers with ultrasound and found a significant negative relation between mean IMT and mean CFD-based WSS in CCA but no significant relation was found in the carotid bulb. Goubergrits et al[31] calculated CFD-based WSS distribution in ex-vivo carotid arteries and showed qualitatively an inverse relationship with WT in the carotid bifurcation.

There were several limitations in this study. Firstly, the study was performed on a small study population. Nevertheless, the patient number was sufficient to investigate the potential use of MRI in WSS calculation in a population based setting by comparing it with WSS based on CFD. Secondly, PC MRI data consisted of the absolute magnitude of 3D velocities. Thirdly, we could not test the association between WSS and changes in the wall thickness over time. This was due to the fact that the follow-up period was short to observe any changes. Longitudinal studies must be performed with longer follow-up period to investigate the associations between wall shear stress and the changes in wall thickness. Additionally, the PC MR images acquired were time averaged and therefore wall characteristics were not associated with temporally-changing WSS and also time dependent hemodynamic parameters such as oscillatory shear index. Finally, a low VENC value (60cm/s) per encoding direction was selected which might have caused aliasing. However, the extended neck positioning, in which the head is positioned at a slight upward angle, minimized this error to a negligible level as was confirmed by our comparison between the measurements with a VENC of 60 cm/s and 120 cm/s (see Appendix).

CONCLUSION

In this study, we showed that MRI and CFD-based WSS calculations show similar inverse relation between wall characteristics of the carotid arteries and WSS in elderly asymptomatic subjects with early wall thickening. The resulting similar inverse relation indicates that both methods are similarly robust and reliable. We suggest that large population studies can be performed by using PC MRI measurements, since PC MRI-based WSS calculations are straightforward and easily applicable in clinical practices.

REFERENCES

[1] Davignon, J, Ganz, P. Role of Endothelial Dysfunction in Atherosclerosis. *Circulation* 2004 Jun 15;109: III27-32.

[2] Wentzel JJ, Corti R, Fayad ZA, Wisdom P, Macaluso F, Winkelman MO, Fuster V, Badimon JJ. Does shear stress modulate both plaque progression and regression in the thoracic aorta? Human study using serial magnetic resonance imaging. *J Am Coll Cardiol.* 2005; 45(6): 846–54.

[3] VanderLaan PA, Reardon CA, Getz GS. Site specificity of atherosclerosis: site-selective responses to atherosclerotic modulators. *Arterioscler, Thromb, Vasc Biol.* 2004; 24(1): 12–22.

[4] Malek AM, Alper SL, Izumo S. Hemodynamic Shear Stress and Its Role in Atherosclerosis. *JAMA*. 1999; 282(21): 2035–2042.

[5] Slager CJ, Wentzel JJ, Gijsen FJH, Thury A, van der Wal AC, Schaar JA, Serruys PW. The role of shear stress in the destabilization of vulnerable plaques and related therapeutic implications. *Nature clinical practice. Cardiovascular medicine.* 2005; 2(9): 456–64.

[6] Cecchi E, Giglioli C, Valente S, Lazzeri C, Gensini GF, Abbate R, Mannini L. Role of hemodynamic shear stress in cardiovascular disease. *Atherosclerosis.* 2011; 214(2): 249–56.

[7] Shaaban AM, Duerinckx AJ. Wall shear stress and early atherosclerosis: a review. *AJR.* 2000; 174(6): 1657–65.

[8] Cibis, M, Potters, WV, Gijsen, FJH, Marquering, H, vanBavel, E,van der Steen, AFW, Nederveen, AJ, Wentzel JJ. Wall shear stress calculations based on 3D cine phase contrast MRI and computational fluid dynamics: a comparison study in healthy carotid arteries. NMR Biomed. 2014 Jul; 27(7):826-34.

[9] Markl, M, Wegent, F, Zech, T, Bauer, S, Strecker, C, Schumacher, M, Weiller, C, Hennig, J, Harloff, A. In vivo_wall shear stress distribution_in_the_carotid_artery: effect of bifurcation geometry, internal_carotid_artery stenosis, and recanalization therapy. Circ Cardiovasc Imaging. 2010 Nov;3(6):647-55.

[10] Gnasso A, Carallo C, Irace C, Spagnuolo V, De Novara G, Mattioli PL, Pujia A. Association between intima-media thickness and wall shear stress in common carotid arteries in healthy male subjects. Circulation. 1996;94:3257–3262.

[11] Irace C, Cortese C, Fiaschi E, Carallo C, Farinaro E, Gnasso A. Wall shear stress is associated with intima-media thickness and carotid athero- sclerosis in subjects at low coronary heart disease risk. Stroke. 2004;35: 464 – 468.

[12] Duivenvoorden, R., vanBavel, E., de Groot, E., Stroes, E. S. G., Disselhorst, J. A., Hutten, B. A., et al. Endothelial shear stress: a critical determinant of arterial remodeling and arterial stiffness in humans-a carotid 3.0-T MRI study. Circulation: Cardiovascular Imaging. 2010; 3(5), 578–585.

[13] van den Bouwhuijsen, QJA, Vernooij, MW, Hofman1, A, Krestin GP, van der Lugt, A, Witteman, JCM. Determinants of magnetic resonance imagingdetected carotid plaque components: the Rotterdam Study. *Eur Heart J* 2012 Jan; 33(2):221-9.

[14] Klein, S, Staring, M, Murphy, K, Viergever, MA, Pluim, JP. Elastix: a toolbox for intensity-based medical image registration. *IEEE Trans Med Imaging.* 2010 Jan; 29(1):196-205.

[15] Yushkevich PA, Piven J, Hazlett HC, Smith RG, Ho S, Gee JC, Gerig G.User-guided 3D active contour segmentation of anatomical structures:significantly improved efficiency and reliability. *Neuroimage* 2006; 31(3): 1116–1128.

[16] Potters W, Van Ooij P, Marquering H, vanBavel E, Nederveen AJ. Volumetric arterial wall shear stress calculation based on cine phase contrast MRI. *J Magn Reson Imaging*. 2014 Jan 17:1-12.

[17] Seo T, Schachter LG, Barakat AI. Computational Study of Fluid Mechanical Disturbance Induced by Endovascular Stents. *Annals of Biomedical Engineering*. 2005; 33(4): 444–456.

[18] Antiga L, Piccinelli M, Botti L, Ene-Iordache B, Remuzzi A, Steinman DA. An image-based modeling framework for patient-specific computational hemodynamics. *Med Biol Eng Comput*. 2008; 46(11): 1097–112.

[19] Kohler U, Marshall I, Robertson MB, Long Q, Xu YX, Hoskins PR. MRI measurement of wall shear stress vectors in bifurcation models and comparison with CFD predictions. *J Magn Reson Imaging*. 2001; 14: 563–573.

[20] Papathanasopoulou P, Zhao S, Köhler U, Robertson MB, Long Q, Hoskins P, Xu XY, Marshall I. MRI measurement of time-resolved wall shear stress vectors in a carotid bifurcation model, and comparison with CFD predictions. *JMRI*. 2003; 17(2): 153–62.

[21] Van Ooij P, Potters WV, Guédon A, Schneiders JJ, Marquering HA, Majoie CB, vanBavel E, Nederveen AJ. Wall shear stress estimated with phase contrast MRI in an in vitro and in vivo intracranial aneurysm. *JMRI*. 2013; 38(4): 876-84

[22] Boussel L, Rayz V, Martin A, Acevedo-Bolton G, Lawton MT, Higashida R, Smith WS, Young WL, Saloner D. Phase-contrast magnetic resonance imaging measurements in intracranial aneurysms in vivo of flow patterns, velocity fields, and wall shear stress: comparison with computational fluid dynamics. *Magn Reson Med*. 2009; 61(2): 409–417.

[23] Isoda H, Ohkura Y, Kosugi T, Hirano M, Alley MT, Bammer R, Pelc NJ, Namba H, Sakahara H. Comparison of hemodynamics of intracranial aneurysms between MR fluid dynamics using 3D cine phase-contrast MRI and MR-based computational fluid dynamics. *Neuroradiology*. 2010; 52(10): 913–920.

[24] Lee, MY, Wu, CM, Yu, KH, Chu, CS, Lee, KT, Sheu, SH, Lai, WT, Association between wall shear stress and carotid atherosclerosis in patients with never treated essential hypertension. *Am J Hypertens.* 2009 Jul;22(7):705-10.

[25] Jiang, Y, Kohara, K, Hiwada, K. Low wall shear stress contributes to atherosclerosis of the carotid artery in hypertensive patients. *Hypertens Res.* 1999 Sep; 22(3):203-7.

[26] Carallo, C, Irace, C, Pujia, A, De Franceschi, MS, Crescenzo, A, Motti, C, Cortese, C, Mattioli, PL, Gnasso, A. Evaluation of common carotid hemodynamic forces. Relations with wall thickening. *Hypertension*. 1999 Aug; 34(2):217-21.

[27] Kornet, L, Lambregts, J, Hoeks, AP, Reneman, RS. Differences in near-wall shear rate in the carotid artery within subjects are associated with different intima-media thicknesses. *Arterioscler Thromb Vasc Biol*. 1998 Dec;18 (12):1877-84.

[28] Peiffer, V, Sherwin, SJ, Weinberg, PD. Does low and oscillatory wall shear stress correlate spatially with early atherosclerosis? A systematic review. *Cardiovasc Res*. 2013 Jul 15; 99(2):242-50.

[29] Steinman, DA, Thomas, JB, Ladak, HM, Milner, JS, Rutt' BK, Spence, JD. Reconstruction of carotid bifurcation hemodynamics and wall thickness using computational fluid dynamics and MRI. *Magn Reson Med*. 2002 Jan;47(1):149-59.

[30] Augst, AD, Ariff, B, McG Thom, SA, Xu, XY, Hughes, AD. Analysis of complex flow and the relationship between blood pressure, wall shear stress, and intima-media thickness in the human carotid artery. *Am J Physiol Heart Circ Physiol*. 2007 Aug; 293(2): H1031-7.

[31] Goubergrits, L, Affeld, K, Fernandez-Britto, J, Falcon, L. Atherosclerosis and flow in carotid arteries with authentic geometries. *Biorheology* 2002;39:519-524.

APPENDIX

Phase difference images vs. complex difference images

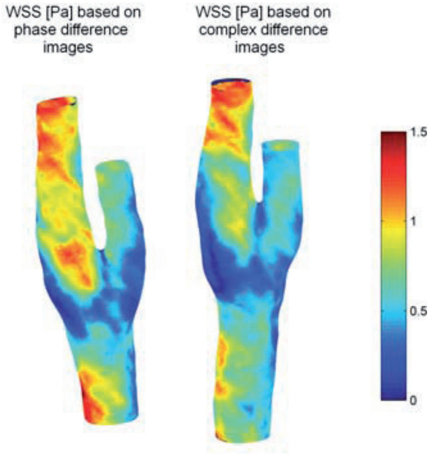

Figure 1A: WSS [Pa] distribution in a healthy carotid artery based on PC MRI complex difference image (Left) and phase difference images (Right).

In Rotterdam study, complex difference images of PC MRI scans were collected. These images provide information only on the absolute velocities in the 3 orthogonal velocity encoding directions. To test the possible use of complex difference images for velocity quantification, a healthy young volunteer underwent 2 consecutive MRI scans carotid arteries within half an hour. The complex difference images were exported in the former scan and the phase difference images in the latter one. Figure 1A shows the comparison of WSS based on complex difference images and phase difference images. Although differences in WSS distribution are observed, this might be due to biological variation (increase in flow), differences in the registration of PC MR Images on anatomical images.

Aliasing

The velocity was encoded in 3 directions with a VENC of 60 cm/s which might be resulted in aliasing. However, by putting the patients neck in an extended pose, with elevated support for the head, the main flow direction in the carotid artery was spread over the anterior-posterior and feet-head velocity encoding direction minimizing the risk of aliasing. To confirm this, we performed 2 consecutive scans in which the VENC was set to 60cm/s and 120 cm/s respectively. The results of WSS distribution at different VENC values are shown in Figure 2A. Although lower VENC resulted in slightly lower WSS values in the inner curve of the internal carotid artery corresponding to high WSS regions, the WSS distribution was found to be similar for both VENC values.

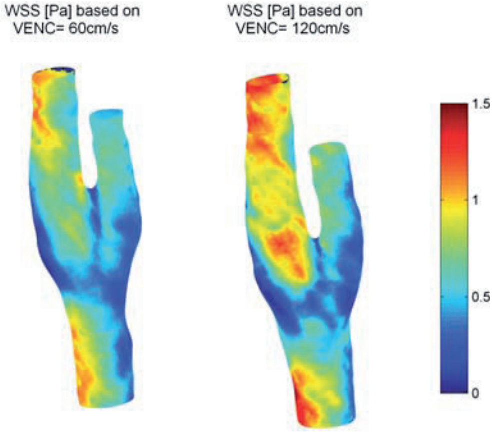

Figure 2A: WSS [Pa] distribution in a healthy carotid artery based on PC MRI with VENC 60 cm/s (Left) and 120 cm/s (Right).

Chapter 4

The effect of spatial and temporal resolution of cine phase contrast MRI on wall shear stress and oscillatory shear index assessment

Based on:

Cibis, M, Potters, WV, Gijsen, FJH, Marquering, H, van Ooij, P, van Bavel, E, Wentzel, JJ, Nederveen, AJ. The effect of spatial and temporal resolution of cine phase contrast MRI on wall shear stress and oscillatory shear index assessment.

Submitted

ABSTRACT

Introduction

Wall shear stress (WSS) and oscillatory shear index (OSI) are associated with atherosclerosis. These parameters can be derived from velocities measured with phase-contrast MRI (PC MRI). Limited spatiotemporal resolution of PC MRI however affects these measurements. We aim to investigate the effect of spatiotemporal resolution using a carotid artery phantom.

Methods

We connected the phantom to a pulsatile flow set-up. MRI measurement planes were placed at the common carotid artery (CCA) and internal carotid artery (ICA). Two-dimensional PC MRI measurements were performed at thirty spatiotemporal resolutions. The MRI-based flow was validated with ultrasound probe measurements. Mean flow, peak flow, flow waveform, WSS and OSI were compared using regression analysis. The slopes of the regression lines were reported in %/mm and %/100ms. The regions of low and high WSS and OSI were also compared.

Results

The mean PC MRI CCA flow (2.5±0.2mL/s) agreed with the ultrasound probe measurements (2.7±0.02mL/s). Mean flow (mL/s) depended only on spatial resolution (CCA:-13%/mm, ICA:-49%/mm). Peak flow (mL/s) depended on both spatial (CCA:-13%/mm, ICA:-17%/mm) and temporal resolution (CCA:-19%/100ms, ICA:-24%/100ms). Mean WSS (Pa) was in inverse relationship with spatial resolution (CCA:-19%/mm, ICA:-33%/mm). OSI was dependent on spatial resolution for CCA (-26%/mm) and temporal resolution for ICA (-16%/100ms). The regions of low and high WSS and OSI matched for most of the measurements.

Conclusions

Mean flow and mean WSS are independent of temporal resolution. Peak flow and OSI are dependent on both spatial and temporal resolution. The spatial distribution of OSI and WSS did not exhibit a strong dependency on spatiotemporal resolution.

INTRODUCTION

Atherosclerotic plaques develop at the sites of low wall shear stress (WSS) in the arteries[1,2]. Besides WSS magnitude, some studies show that oscillatory changes of the WSS direction may promote atherogenesis[3-5]. Such oscillations within the cardiac cycle are quantified by the oscillatory shear index (OSI)[6,7]. Although both WSS and OSI contribute to initiation and progression of atherosclerotic disease, most studies focus only on the WSS magnitude and exclude analysis of OSI due to the challenge of obtaining accurate WSS magnitude and OSI simultaneously[8-12].

WSS magnitude is calculated by multiplying blood viscosity with wall shear rate (WSR), the latter being the first radial derivative of blood velocity at the vessel wall. The velocity field in the artery that is necessary to calculate WSR is generally obtained with computational fluid dynamics (CFD). CFD is a powerful simulation tool that enables prediction of blood velocities and related hemodynamic parameters[13,14]. However, CFD requires accurate boundary conditions, non-clinical expertise and extensive computational resources and time. Alternatively, the velocities can be obtained by phase contrast MRI (PC MRI) measurements[15-18]. However, the WSS values based on MRI depend on the spatial resolution of PC MRI[19-23]. In a recent study, we showed that WSS estimates based on in vivo PC MRI data have a realistic representation of the spatial distribution but underestimate magnitude, due to the limited spatial resolution of PC MRI[19]. Stalder et al. also investigated the effect of spatial resolution on flow and WSS using synthetic data[17] and showed that the WSS values calculated with the method they proposed were strongly affected by the spatial resolution. Petersson et al. showed that higher true WSS values were underestimated more by PC MRI and reducing the resolution enhanced the underestimation[20]. These findings suggest that the spatial resolution of PC MRI measurements should be sufficiently high to obtain the magnitude of WSS accurately. OSI, on the other hand, is a measure of temporal changes of WSS. An accurate estimation of OSI might, therefore, only be possible with both sufficiently high spatial and temporal resolutions of PC MRI measurements.

The MRI settings such as the spatiotemporal resolution involve a trade-off between the measurement duration and the accuracy of the flow, WSS and the OSI estimations. To perform the measurement within clinically feasible scan time, the resolution is generally kept low and the accuracy of these parameters is given away. One can, however, argue that each estimated parameter is affected differently. To our knowledge, none of the previous studies has investigated the effect of spatial and temporal resolution together on these hemodynamic parameters extensively. Our objective was to evaluate the effect of resolution on the assessments of flow, WSS and OSI that we obtained from 2D cine PC MRI scans of a carotid artery phantom at different spatial and temporal resolutions.

METHODS

Phantom and flow set-up

A silicone phantom was built based on the surface reconstruction of a healthy right carotid artery (age 25 years old) acquired from a previous study[19] (figure 1a). The phantom was connected to a flow set-up (figure 1b). The set-up consisted of a computer, computer controlled pulse generator, an air pressure controller (LifeTec Group, Eindhoven, The Netherlands) and a closed flow phantom circuit filled with water. The computer, the pulse generator, the air pressure controller, and the flow meter were placed outside the MRI room. The phantom circuit, including an MR compatible pump system, was placed on the MR table connected to the phantom. The pump system consisted of thin-walled silicone cylinders that were filled with water and embedded in a rigid air-filled enclosure. Air pressure in the rigid enclosure was varied to dilate and contract the water-filled cylinders. One-way valves ensured that this cyclic air pressure induced a pulsatile flow. The shape and the magnitude of the flow waveform were set by adjusting the shape and the amplitude of the cyclic air pressure wave. The shape of the waveform was then tuned by adjustment of resistors and capacitors within the closed fluid circuit. A real-

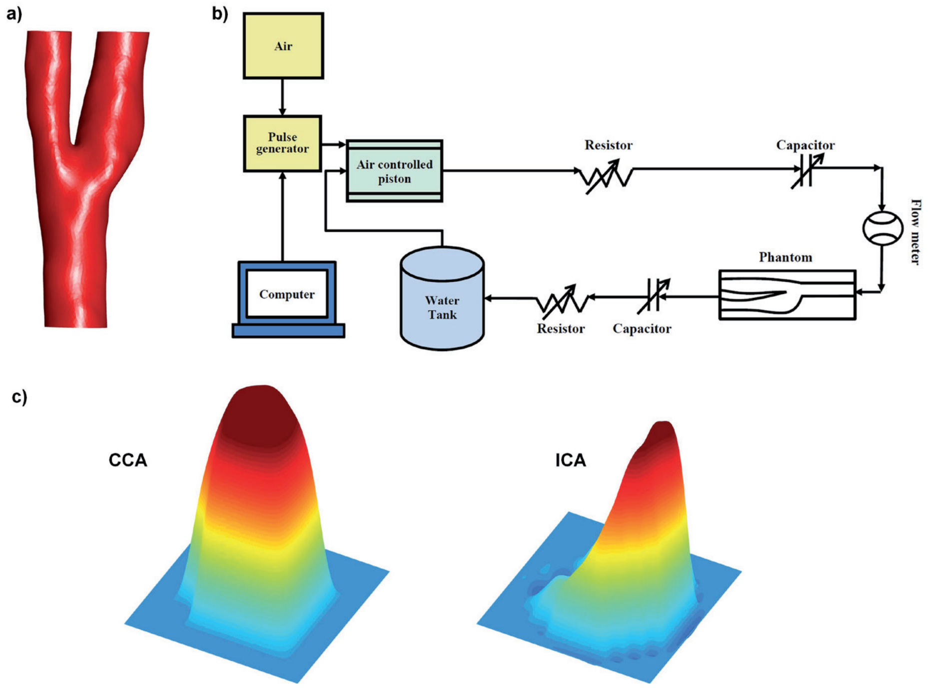

Figure 1. a) The surface reconstruction of the healthy right carotid artery based on which the phantom was built b) The sketch of the pulsatile water flow set-up c) The velocity profile measured at CCA (left) and at ICA (right) measurement planes.

time ultrasound flow probe was used to calibrate the PC MRI measured flow waveform before the MRI scans outside the MRI room while keeping all experimental conditions the same.

MRI acquisition

The carotid phantom was scanned with a 3.0T MR system (Ingenia, software version 4.1.3, Philips Healthcare, The Netherlands) using a solenoid rat coil. 2D cine PC MRI scans were performed at two planes with velocity encoding in 3 directions using various temporal and spatial resolutions as shown in figure A1 of the appendix in red circles (venc: 100 cm/s, TR: 8.9 – 24.1 ms, TE: 4.67 – 6.57ms, flip angle: 10°). We performed thirty measurements at different spatial and temporal resolutions at two planes, which took between 1.1 and 21.0 minutes per measurement depending on the spatiotemporal resolution. All measurements were performed on the same day without an interruption of the flow setup to prevent any changes in the pulse shape. The flow stability was verified with the ultrasound flow probe before and after the MR session. While the typical velocity profile in the common carotid artery (CCA) is closer to a parabolic shape, it is more skewed in the internal carotid artery (ICA) as shown in figure 1c. Hence, the WSS and OSI distributions are different between CCA and ICA. To analyze both velocity profiles and to avoid MR table movement in between positions, we chose the first plane 1 cm proximal to the branching point perpendicular to CCA and the second plane 1 cm distal to the branching point perpendicular to ICA. All the acquisitions were performed with retrospective triggering, except those requiring a temporal resolution below 30 ms. For acquisitions with temporal resolution below 30 ms, prospective triggering was used to be able to measure separate flow encoding directions in separate heart cycles. All PC MRI data was corrected for first-order phase offset errors.

Segmentation

The vessels were automatically segmented on the MRI measurement planes by an in-house tool written in MATLAB. Initial segmentation was performed by k-means clustering, followed by an active contour segmentation using the method by Herment[21]. A separate segmentation was performed for each measurement. The segmentation performed on the images at the highest spatial resolution (0.2 mm) will be denoted as the 'best segmentation' in the rest of this article.

WSS calculations based on phase contrast MRI

Since the workflow for WSS calculations based on PC MRI was discussed before in detail, we give a short overview only[22]. Firstly, the inward normal was determined for each point on the surface. The velocities measured by PC MRI were interpolated along the inward normal direction at 2 points at a distance of 1.5 and 3 mm from the wall[22]. The velocity at the surface was set to zero, and a spline curve was fitted through these two velocity vectors with inclusion of the zero velocity point at the wall. By taking the gradient of the curve at the point on the wall, wall shear rate (WSR) was calculated. WSS was calculated by multiplying WSR with the dynamic viscosity of water which was assumed to be $1.0 \cdot 10^{-3}$ Pa·s.

Oscillatory shear stress calculations

The commonly used definition of OSI was introduced by He et al[7] as follows:

$$OSI(\vec{s}) = 0.5 \left[1 - \frac{\left|\Sigma_0^T \overrightarrow{WSS}(\vec{s},t)\Delta t\right|}{\Sigma_0^T \left|\overrightarrow{WSS}(\vec{s},t)\right| \Delta t} \right] \qquad \text{Eq. 1}$$

where $\vec{s}$ is the position at the vessel wall, t is the time point, Δt is time step, and T is the number of time steps within the cardiac cycle. The OSI varies between 0 and 0.5 where higher OSI indicates larger changes in the WSS direction.

Analysis

The flow waveforms measured in the CCA were compared with the ultrasound flow probe measurements. For different spatiotemporal resolutions, we analyzed cross-sectional area, mean flow, peak flow, WSS, and OSI at the CCA and ICA. The WSS values were firstly averaged over the cardiac cycle and subsequently over the circumference of the vessel wall. The OSI values were averaged over the circumference of the vessel wall. Furthermore, to study the local distribution of WSS and OSI over the circumference, WSS and OSI values were averaged separately over the quarters of the vessels. Finally, to investigate the effect of segmentation on the estimated hemodynamic parameters, the 'best segmentation' was applied to each dataset. The mean flow, WSS and OSI were obtained with the best segmentation and compared with those obtained with the segmentation per measurement.

Statistical analysis

The associations between spatiotemporal resolutions and the hemodynamic parameters and between the results based on the measurement-specific segmentations and best segmentation were tested by linear regression analysis. In statistical evaluations, the level of significance was chosen at $p<0.05$. The results were represented as the mean ± standard deviation of the 30 measurements.

RESULTS

The linear regression coefficients and the slopes of the linear regression lines (in %/mm and %/100ms) between the hemodynamic parameters and spatiotemporal resolution are summarized in table 1.

Table 1. (CCA: top, ICA: bottom): The regression analysis for different spatiotemporal resolutions and the hemodynamic parameters. The slopes (in %/mm and %/100ms) were calculated by dividing flow, WSS and OSI with their respective maxima. (*) indicates that $p<0.05$, and (^{NS}) indicates $p>=0.05$.

	Spatial resolution		Temporal resolution	
CCA	r^2	Slope (%/mm)	r^2	Slope (%/100ms)
Mean flow [mL/s]	0.32	-13.0%*	0.00	-0.4%^{NS}
Peak flow [mL/s]	0.13	-13.0%^{NS}	0.66	-19.0%*
WSS [Pa]	0.36	-19.0%*	0.09	-6.0% ^{NS}
OSI	0.16	-26.0%*	0.10	-13.0% ^{NS}
	Spatial resolution		**Temporal resolution**	
ICA	r^2	Slope (%/mm)	r^2	Slope (%/100ms)
Mean flow [mL/s]	0.70	-49.0%*	0.00	-1.4% ^{NS}
Peak flow [mL/s]	0.15	-17.0%*	0.44	-24.0%*
WSS [Pa]	0.64	-33.0%*	0.04	-5.6% ^{NS}
OSI	0.06	-16.0%^{NS}	0.16	-16.0%*

Flow waveform at CCA

Flow waveforms obtained from PC MRI measurements at the highest and the lowest spatial and temporal resolutions are shown in figure 2a. The red line shows the flow waveform based on the ultrasound probe measurement. At the highest spatial resolution (0.2 mm) and the highest temporal resolution (24.4 ms, black dashed line), the shape of the flow waveform was similar to the one measured by the ultrasound probe. At the lowest spatial resolution (1.0 mm) and the highest temporal resolution (9.1 ms, light blue dashed line), the shape of the flow waveform was still captured although peak flow was underestimated (7.8 mL/s). At lowest temporal resolution (142.9 ms, red and orange dashed lines), the peak flow was shifted backward in the cardiac cycle and was underestimated. The ultrasound probe measurements were plotted against the PC MRI measured flows in figure 2b which shows underestimation of flow at higher flows in all cases except for the measurement at the highest spatial and temporal resolution.

Area, mean flow, and peak flow at CCA and ICA

The cross-sectional area was 24.6 ± 0.6 mm^2 at the CCA and 29.0 ± 2.9 mm^2 at the ICA. The mean flow based on PC MRI measurements was 2.5 ± 0.2 mL/s at the CCA and 1.3 ± 0.2 mL/s at the ICA. The mean flow is plotted for the different spatial resolutions in figure

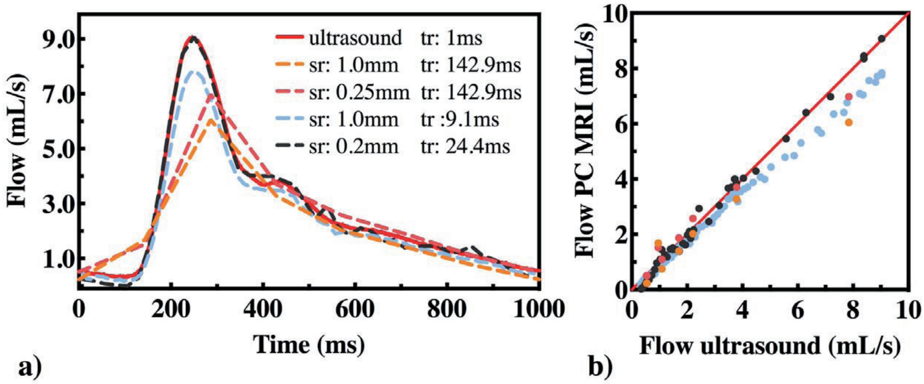

Figure 2. a) Flow waveforms at different spatial(sr) and temporal(tr) resolutions. Colored dashed lines show the PC MRI measurements and the red line shows the ultrasound probe measurement. Spatial resolution varied between 0.2mm and 1 mm and the temporal resolution varied between 9.1 ms and 142.9 ms. b) Ultrasound probe vs. PC MRI flow measurements.

3a and for the different temporal resolutions in figure 3b. A significant association was found between mean flow and the spatial resolution (slope -13.0 %/mm for the CCA and -49.0 %/mm for the ICA). No correlation was observed between mean flow and temporal resolution. The mean flow based on the ultrasound flow probe measurement was 2.7 ± 0.02 mL/s at CCA; hence, the ratio of the mean flows based on PC MRI measurements and the ultrasound flow probe measurement was 95.1 ± 7.9%.

The peak flow was 7.6 ± 1.0mL/s at CCA and 4.2 ± 0.6 mL/s at ICA. The peak flows at different spatiotemporal resolutions are shown in figure 3c and figure 3d. At the highest spatial resolution (0.2 mm) and the highest temporal resolution (24.4 ms), the peak flow was estimated accurately (9.1 mL/s) relative to ultrasound probe peak flow measurement (9.1 mL/s). At lower spatiotemporal resolutions, peak flow was underestimated. The estimated peak flow was significantly dependent on both spatial (-17.0 %/100ms for ICA) and temporal resolution (-19.0 %/100ms for CCA to -24.0 %/100ms for ICA).

WSS at CCA and ICA

The WSS at different spatial and temporal resolutions are shown for CCA and ICA in figure 4a and figure 4b. The WSS was 0.12 ± 0.01 Pa at the CCA and 0.09 ± 0.02 Pa at the ICA. At the highest spatial resolution (0.2 mm) and the highest temporal resolution (24.4 ms), WSS was determined as 0.15 Pa at the CCA and 0.14 Pa at the ICA. At lower spatial resolutions, the estimated WSS was lower. We found a significant inverse relationship between the estimated WSS and the spatial resolution (-19.0 %/mm for the CCA and -33.0 %/mm for the ICA). No relationship was found between mean WSS and temporal resolution.

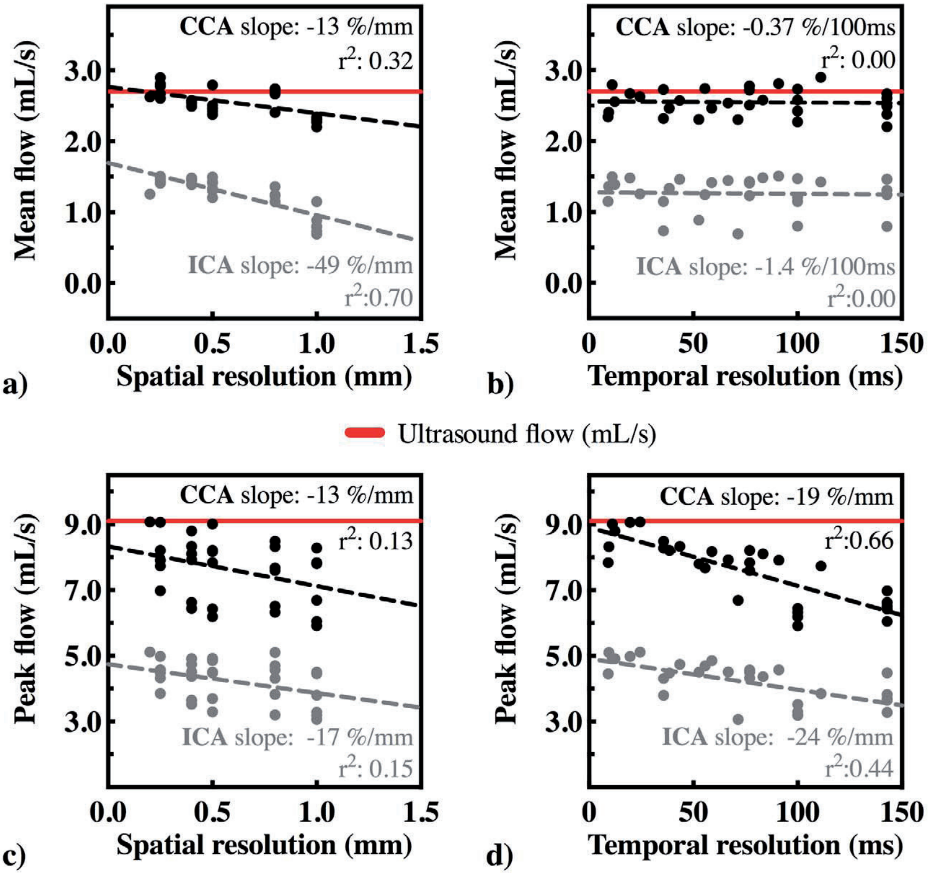

Figure 3. a) Mean flow [mL/s] vs spatial resolution [mm] b) Mean flow [mL/s] vs temporal resolution [ms] c) Peak flow [mL/s] vs spatial resolution and d) Peak flow [mL/s] vs temporal resolution at CCA and at ICA. Red lines show the mean and peak flow measured bu ultrasound echo probe.

OSI at CCA and ICA

Figure 4c and figure 4d show OSI at different spatial and temporal resolutions for the CCA and ICA. OSI was found 0.02 ± 0.02 at the CCA and 0.08 ± 0.05 at the ICA. The highest OSI values were found at the highest spatial resolution (0.2 mm) and the highest temporal resolution (24.4 ms), which were 0.08 for the CCA and 0.27 for the ICA. The OSI was underestimated at lower spatiotemporal resolutions. We found a significant association between OSI and spatial resolution in the CCA (-26.0 %/mm), but the association between OSI and temporal resolution was not significant in the CCA. In the ICA, we only found a significant association between OSI and temporal resolution (-16.0 %/100ms).

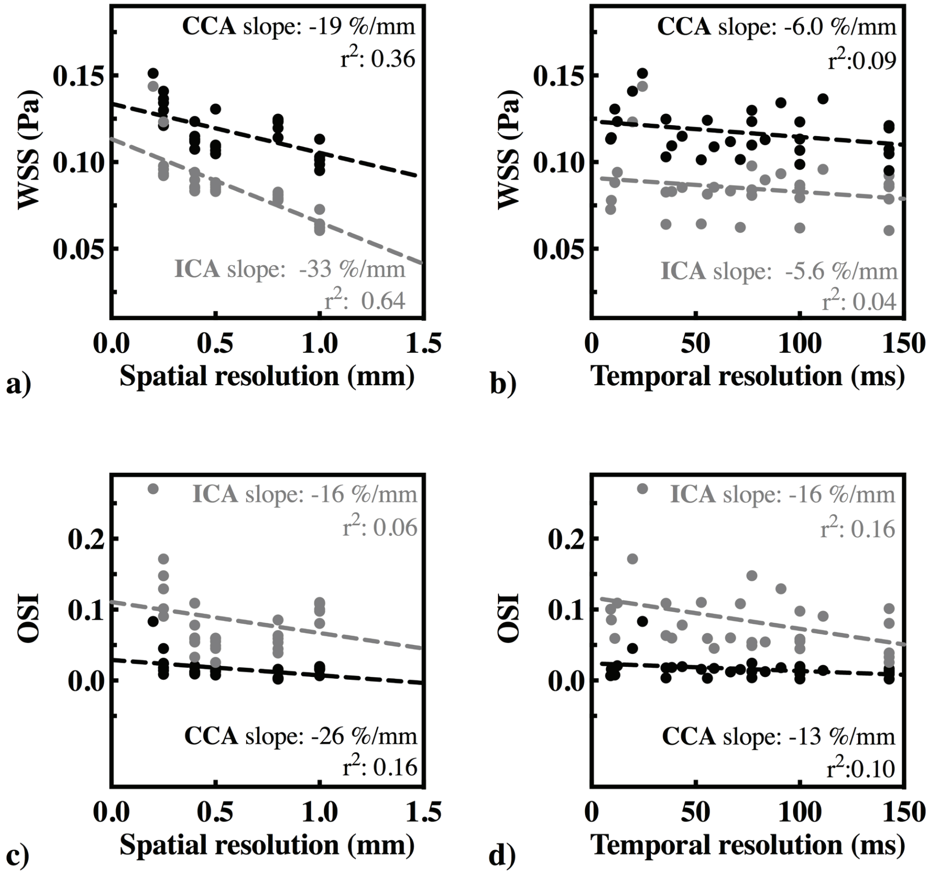

Figure 4. a) WSS [Pa] vs spatial resolution [mm] b) WSS [Pa] vs temporal resolution [ms] c) OSI vs spatial resolution and d) OSI vs temporal resolution at CCA and at ICA

Local WSS distribution

The mean WSS of each quarter for four measurements in the CCA and the ICA is shown in figure 5. For the CCA, the highest WSS quarter was the bottom right quarter (0.14 ± 0.01 Pa) and the lowest WSS quarter was the top left quarter (0.07 ± 0.02 Pa). These highest and the lowest of WSS regions were found in all measurements for the CCA regardless of spatial and temporal resolution. For the ICA, the highest WSS quarter was the bottom right quarter (0.13 ± 0.02 Pa) which was found in all measurements. The lowest WSS quarter for the ICA was the top left quarter (0.04 ± 0.02 Pa) which was found in 28/30 measurements (93%).

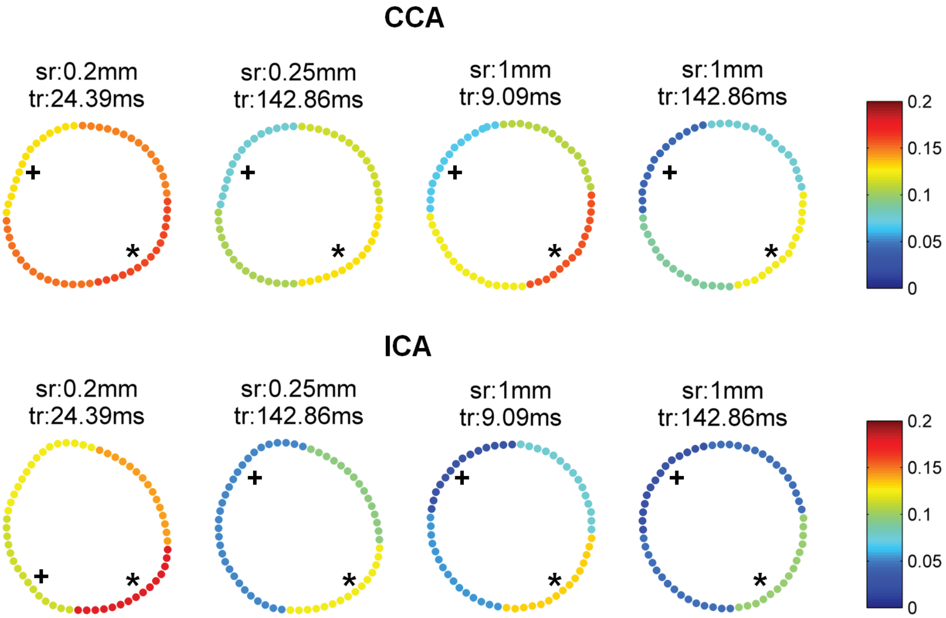

Figure 5. The mean WSS [Pa] of each quarter at different spatial and temporal resolutions in CCA and in ICA. * shows the highest WSS quarter and + shows the lowest WSS quarter.

Local OSI distribution

The mean OSI of each quarter for four measurements is shown in figure 6. OSI was generally low in all quarters of the CCA. The highest OSI quarter in the CCA was the top left quarter (0.04 ± 0.02) which was found in 23/30 measurements (77%). The lowest OSI quarter was bottom right quarter, (0 ± 0.01) and found in 29/30 (97%) measurements. For ICA, the highest OSI quarter was top left quarter (0.20 ± 0.08) and the lowest OSI quarter was the bottom right quarter (0.01 ± 0.01) which was found in all measurements regardless of spatial and temporal resolution.

Calculations using fixed segmentation at CCA

The best segmentation resulted in the cross-sectional area of 24.7 mm^2 for the CCA. The results based on the best segmentation were very similar to those based on the segmentations per measurement. The flow obtained with the best segmentation was 2.7 ± 0.2 mL/s which was in agreement with the ultrasound probe flow measurements and 8.0% higher than that obtained with the measurement specific segmentations (2.5± 0.2 mL/s, $r^2 = 0.85$, $p<0.001$). We found no significant correlation between the mean flow and spatial resolution after switching to the best segmentation ($r=-0.09$, $p=0.62$). The WSS with the best segmentation showed good agreement with that based on the measurement specific segmentations ($r^2 = 0.99$), which were on average only 2% lower in magnitude (0.11 ± 0.01 Pa, $p<0.001$). The mean OSI based on the best segmentation

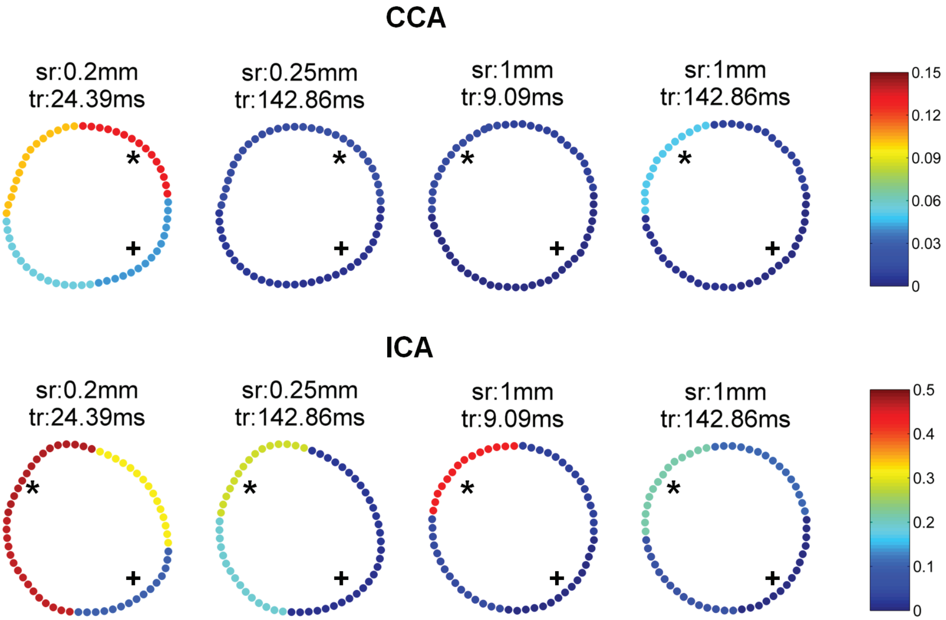

Figure 6. The mean OSI of each quarter at 4 different spatial and temporal resolutions in CCA and in ICA. * shows the highest OSI quarter and + shows the lowest OSI quarter.

was 0.02 ± 0.02 which was also in good agreement with that based on the measurement specific segmentations ($r^2 = 0.99$).

DISCUSSION

In this study, we investigated the influence of spatial and temporal resolution on the estimation of mean flow, peak flow, WSS and OSI in a realistic phantom of a carotid bifurcation. Our results show that not all parameters are affected to the same extent by spatial and temporal resolution. For example, mean flow was not dependent on the temporal resolution; but it was influenced by the spatial resolution. This was caused mainly by the difference in segmentation. At lower spatial resolutions, delineating the borders of the cross-sectional area was more difficult with larger voxels around the vessel wall. In fact, applying the best segmentation improved the estimation of mean flow for all resolutions. Nevertheless, mean flow was estimated accurately with less than 10% error regardless of the segmentation, the spatial and the temporal resolution. These observations correspond well with previous literature that also showed correct flow rates for lower resolution scans[17]. Please note that correct flow quantification requires a minimum number of 3-4.5 voxels/diameter[24,25].

The estimated flow waveform and the peak flow were mainly dependent on temporal resolution. To obtain the peak systolic time point within the cardiac cycle and the peak systolic flow accurately, it was necessary to perform the acquisition at a high temporal resolution. The higher temporal resolution also reduced flattening of the flow waveform. At a temporal resolution lower than 50 ms, the error in the estimated peak flow was more than 10%.

The WSS values were specifically relying on high spatial resolution. The observed effects of spatial resolution on average WSS magnitude are in correspondence with existing literature. The typical underestimation of WSS, when quantified by PC MRI, has been described extensively[17,20,22,26,27]. For a parabolic flow with a flow rate equal to the measured CCA mean flow, the theoretical WSS value is approximately 0.15 Pa. Since the velocity profile at CCA was close to a parabolic shape, the WSS was expected to have a value close to the theoretical WSS value. Only at a spatial resolution of 0.2 mm, the WSS based on PC MRI was close to the theoretical value and underestimated at lower resolutions. However, the changes in the spatial resolution at lower spatial resolutions had only a marginal impact in the estimated WSS value, e.g. a decrease of 0.1 mm in spatial resolution only decreases the WSS by 2-3%. Note that the duration of our 2D PC MRI measurements at spatial resolution of 0.2 mm and temporal resolution of 24 ms was 21 minutes at only one plane which is not feasible in the clinic. Furthermore, the noise level increases with the increase of spatial resolution, even more if a standard receive coil is used. Nevertheless, recent developments in MRI acceleration technologies will lead to shorter scan times and/or decreased noise levels at high resolutions[28,29], which, in time, will allow faster and more accurate WSS based on PC MRI.

The effects of temporal resolution on time-resolved WSS parameters have not been investigated previously. We found that the WSS values averaged over the cardiac cycle were not dependent on the temporal resolution. For the CCA, OSI was dependent on spatial resolution, but not on temporal resolution. For the ICA, OSI was dependent on temporal resolution, but not on spatial resolution. This is likely due to the low OSI in the CCA and the high OSI in the ICA. OSI values were higher at high spatial and temporal resolutions. However, at lower spatiotemporal resolutions, the changes in the spatiotemporal resolutions affect the estimated OSI values only to a limited extent.

Despite underestimation of the WSS and the OSI magnitude, the locations of low and high WSS and OSI regions showed a good agreement in most of the measurements, regardless of spatiotemporal resolution. This result together with the limited dependency of WSS and OSI values on the chosen spatiotemporal resolutions indicates that WSS and OSI can be compared between studies with similar PC MRI protocols.

Although the segmentation had an influence on the estimated flow, the effect of segmentation on WSS and OSI was found to be small. This may be related to the fact that choosing zero velocity at the wall improves the robustness of WSS estimations, as shown by Petersson et al[20].

In this study, we used a carotid flow profile of the CCA and the ICA, which represents two typical velocity profiles inside carotid arteries. We therefore expect that our results on the effect of spatiotemporal resolutions are representative for other areas of the carotid arteries and other vessels with similar velocity profiles.

This study had three main limitations. Firstly, we limited the study to only 2D PC MRI measurements (with 3D velocity encoding) within the carotid artery. We chose to perform 2D acquisition to keep the MRI scans within clinically acceptable scan times since high-resolution 4D PC MRI measurements would result in unacceptable long scan times. To overcome this limitation, we chose two MRI measurement planes, one at CCA, and one at ICA, representing the relevant two velocity profiles. Secondly, we performed only in vitro measurements, which do not necessarily represent in vivo situation. However, the long scan times would again be the limitation to perform measurements at very high spatial and temporal resolutions. Finally, we used water as the medium instead of a blood representing fluid. However, the effect of blood viscosity on the estimated WSS values was beyond the scope of this study.

CONCLUSIONS

In this study, we showed that the hemodynamic parameters such as mean flow, peak flow, flow waveform, WSS and OSI are influenced by spatial and temporal resolution of PC MRI measurements but to different extents. The mean flow is dependent on the spatial resolution which is caused by the segmentation errors. However, the effect of spatial resolution on the mean flow is small. We show that both mean flow and mean WSS are independent of temporal resolution. WSS is more sensitive to spatial resolution, while OSI is sensitive to both spatial and temporal resolution. Nevertheless, this study shows that the magnitude of mean and peak flow, WSS and OSI as well as the location of low and high WSS did not exhibit a strong dependency on the spatiotemporal resolution of the measurement.

ACKNOWLEDGEMENTS

We thank Marco Stijnen and Anthal Smits for their help with installing and adjusting the pump system.

REFERENCES

[1] Malek AM, Alper SL, Izumo S. Hemodynamic shear stress and its role in atherosclerosis. JAMA. 1999 Dec 1; 282(21):2035-42.

[2] VanderLaan PA, Reardon CA, Getz GS. Site specificity of atherosclerosis: site-selective responses to atherosclerotic modulators. Arterioscler. Thromb. Vasc. Biol. 2004; 24(1): 12–22.

[3] Cheng C, Tempel D, van Haperen R van der Baan A, Grosveld F, Daemen MJ, Krams R, de Crom R. Atherosclerotic lesion size and vulnerability are determined by patterns of fluid shear stress. Circulation. 2006; 113:2744–2753

[4] van Bochove GS, Straathof R, Krams R, Nicolay K, Strijkers GJ. MRI-determined carotid artery flow velocities and wall shear stress in a mouse model of vulnerable and stable atherosclerotic plaque. MAGMA 2010 Apr; 23(2):77–84

[5] Peiffer V, Sherwin SJ, Weinberg PD. Computation in the rabbit aorta of a new metric - the transverse wall shear stress - to quantify the multidirectional character of disturbed blood flow. J Biomech. 2013 Oct 18; 46(15):2651-8.

[6] Ku DN, Giddens DP, Zarins CK, Glagov S. Pulsatile flow and atherosclerosis in the human carotid bifurcation. Positive correlation between plaque location and low oscillating shear stress. Arterioscler Thromb Vasc Biol 1985; 5:293–302

[7] He X, Ku DN. Pulsatile Flow in the Human Left Coronary Artery Bifurcation: Average Conditions. J Biomech Eng 118(1), 74-82.

[8] Wentzel JJ, Corti R, Fayad ZA, Wisdom P, Macaluso F, Winkelman MO,Fuster V, Badimon JJ. Does shear stress modulate both plaque progression and regression in the thoracic aorta? Human study using serial magnetic resonance imaging. J. Am. Coll. Cardiol. 2005; 45(6): 846–854.

[9] Cecchi E, Giglioli C, Valente S, Lazzeri C, Gensini GF, Abbate R, Mannini L. Role of hemodynamic shear stress in cardiovascular disease. Atherosclerosis 2011; 214(2): 249–256.

[10] Slager CJ, Wentzel JJ, Gijsen FJH, Thury A, van der Wal AC, Schaar JA, Serruys PW. The role of shear stress in the destabilization of vulnerable plaques and related therapeutic implications. Nat. Clin. Pract. Cardiovasc. Med. 2005; 2(9): 456–464.

[11] Shaaban AM, Duerinckx AJ. Wall shear stress and early atherosclerosis: a review. Am. J. Roentgenol. 2000; 174(6): 1657–1665.

[12] Potters WV, Marquering HA, vanBavel E, Nederveen AJ. Measuring Wall Shear Stress Using Velocity-Encoded MRI. Curr Cardiovasc Imaging Rep. 2014; 7:9257.

[13] Steinman DA, Image-based computational fluid dynamics: a new paradigm for monitoring hemodynamics and atherosclerosis. Curr Drug Targets Cardiovasc Haematol Disord. 2004 Jun; 4(2):183-97.

[14] Valen-Sendstad K, Steinman DA. Mind the Gap: Impact of Computational Fluid Dynamics Solution Strategy on Prediction of Intracranial Aneurysm Hemodynamics and Rupture Status Indicators. AJNR Am J Neuroradiol. 2014 Mar; 35(3):536-43.

[15] Frydrychowicz A, Stalder AF, Russe MF, Bock J, Bauer S, Harloff A, Berger A, Langer M, Hennig J, Markl M. Three-dimensional analysis of segmental wall shear stress in the aorta by flow-sensitive fourdimensional- MRI. J. Magn. Reson. Imaging 2009; 30(1): 77–84.

[16] Stokholm R, Oyre S, Ringgaard S, Flaagoy H, Paaske WP, Pedersen EM. Determination of wall shear rate in the human carotid artery by magnetic resonance techniques. Eur. J. Vasc. Endovasc. Surg. 2000; 20(5): 427–433.

[17] Stalder AF, Russe MF, Frydrychowicz A, Bock J, Hennig J, Markl M. Quantitative 2D and 3D phase contrast MRI: optimized analysis of blood flow and vessel wall parameters. Magn. Reson. Med. 2008; 60(5): 1218–1231.

[18] Papathanasopoulou P, Zhao S, Köhler U, Robertson MB, Long Q, Hoskins P, Xu XY, Marshall I. MRI measurement of time-resolved wall shear stress vectors in a carotid bifurcation model, and comparison with CFD predictions. J. Magn. Reson. Imaging 2003; 17(2): 153–162.

[19] Cibis M, Potters W.V, Gijsen, F.J.H, Marquering H, vanBavel E, van der Steen AF, NederveenA J, Wentzel J J. Wall Shear Stress Calculations based on 3D Cine Phase Contrast MRI and Computational Fluid Dynamics: a Comparison Study in Healthy Carotid Arteries Comparison of Wall Shear Stress based on Phase Contrast MRI and CFD. NMR in Biomedicine 2014 Jul; 27(7):826-34.

[20] Petersson S, Dyverfeldt P, Ebbers T. Assessment of the accuracy of MRI wall shear stress estimation using numerical simulations. J Magn Reson Imaging 2012 Jul; 36(1):128-38.

[21] Herment A, Kachenoura N, Lefort M, Bensalah M, Dogui A, Frouin F, Mousseaux E, De Cesare A. Automated segmentation of the aorta from phase contrast MR images: validation against expert tracing in healthy volunteers and in patients with a dilated aorta. J Magn Reson Imaging. 2010 Apr; 31(4):881-8.

[22] Potters W, Van Ooij P, Marquering H, vanBavel E, Nederveen AJ. Volumetric arterial wall shear stress calculation based on cine phase contrast MRI. J. Magn. Reson. Imaging 2015 Feb;41(2):505-16.

[23] Van Ooij P, Potters WV, Guédon A, Schneiders JJ, Marquering HA, Majoie CB, vanBavel E, Nederveen AJ. Wall shear stress estimated with phase contrast MRI in an in vitro and in vivo intracranial aneurysm. J. Magn. Reson. Imaging 2013; 38(4): 876–884.

[24] Tang C, Blatter DD, Parker DL. Accuracy of phase-contrast flow measurements in the presence of partial-volume effects. J Magn Reson Imaging. 1993 Mar-Apr; 3(2):377-85.

[25] Hofman MBM, Visser FC, van Rossum AC, Vink GQM, Sprenger M, Westerhof N. In vivo validation of magnetic resonance blood volume flow measurements with limited spatial resolution in small vessels. Magn Reson Med 2012; 33:778-784

[26] Chang W, Frydrychowicz A, Kecskemeti S, Landgraf B, Johnson K, Wu Y, Wieben O, Mistretta C, Turski P. The effect of spatial resolution on wall shear stress measurements acquired using radial phase contrast magnetic resonance angiography in the middle cerebral arteries of healthy volunteers. Preliminary results. Neuroradiol J. 2011 Mar 29; 24(1):115-20.

[27] Cheng CP, Parker D, Taylor CA. Quantification of Wall Shear Stress in Large Blood Vessels Using Lagrangian Interpolation Functions with Cine Phase-Contrast Magnetic Resonance Imaging. Annals of Biomedical Engineering, 2002 Vol. 30, pp. 1020–1032.

[28] Giese D, Schaeffter T, Kozerke S. (2013), Highly undersampled phase-contrast flow measurements using compartment-based k–t principal component analysis. Magn Reson Med, 69: 434–443.

[29] Kim D, Dyvorne HA, Otazo R, Feng L, Sodickson DK, Lee VS. (2012). Accelerated Phase-Contrast Cine MRI Using k-t SPARSE-SENSE. Magnetic Resonance in Medicine, 67(4), 1054–1064.

APPENDIX

The two variable maps show the relationship between spatiotemporal resolutions and the magnitude of the hemodynamic parameters. The measurement points are shown with red circles. The values in the intermediate resolution points were interpolated. The plots included the isolines of the measurement duration for 18, 6 and 2 minutes.

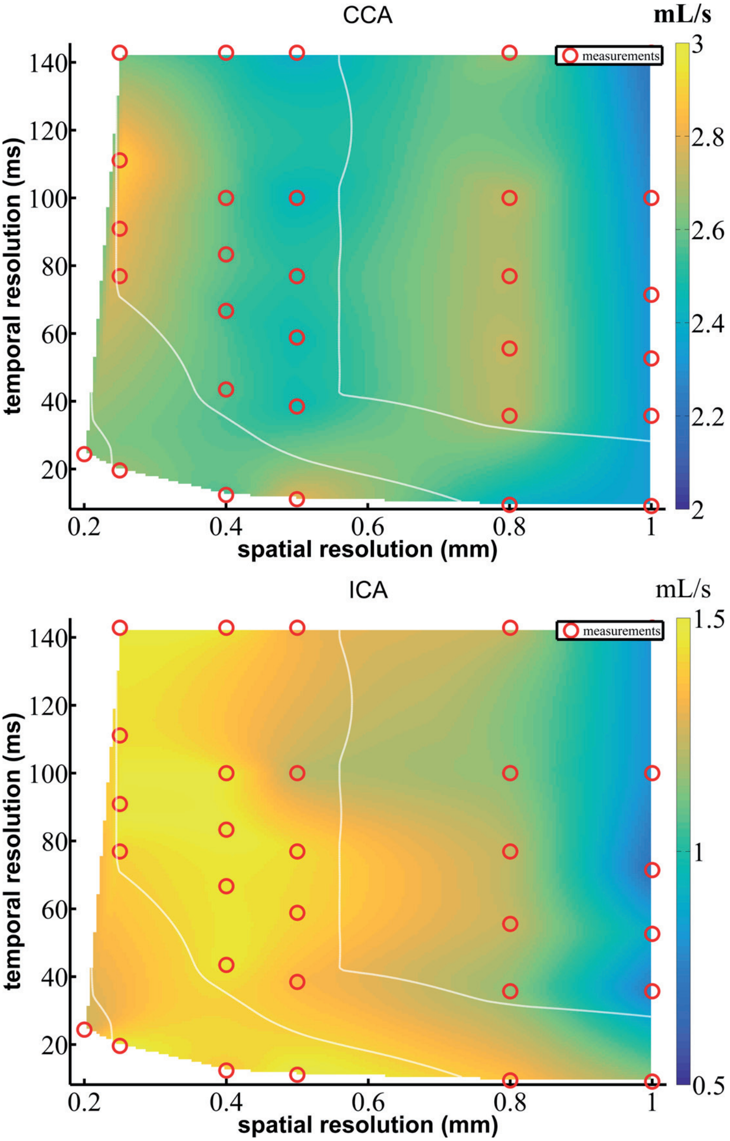

Figure 1A: Mean flow of a) CCA and b) ICA at different spatial and temporal resolutions. Red circles show the measurement points. White lines show the measurement durations of 18, 6 and 2 minutes (left to right).

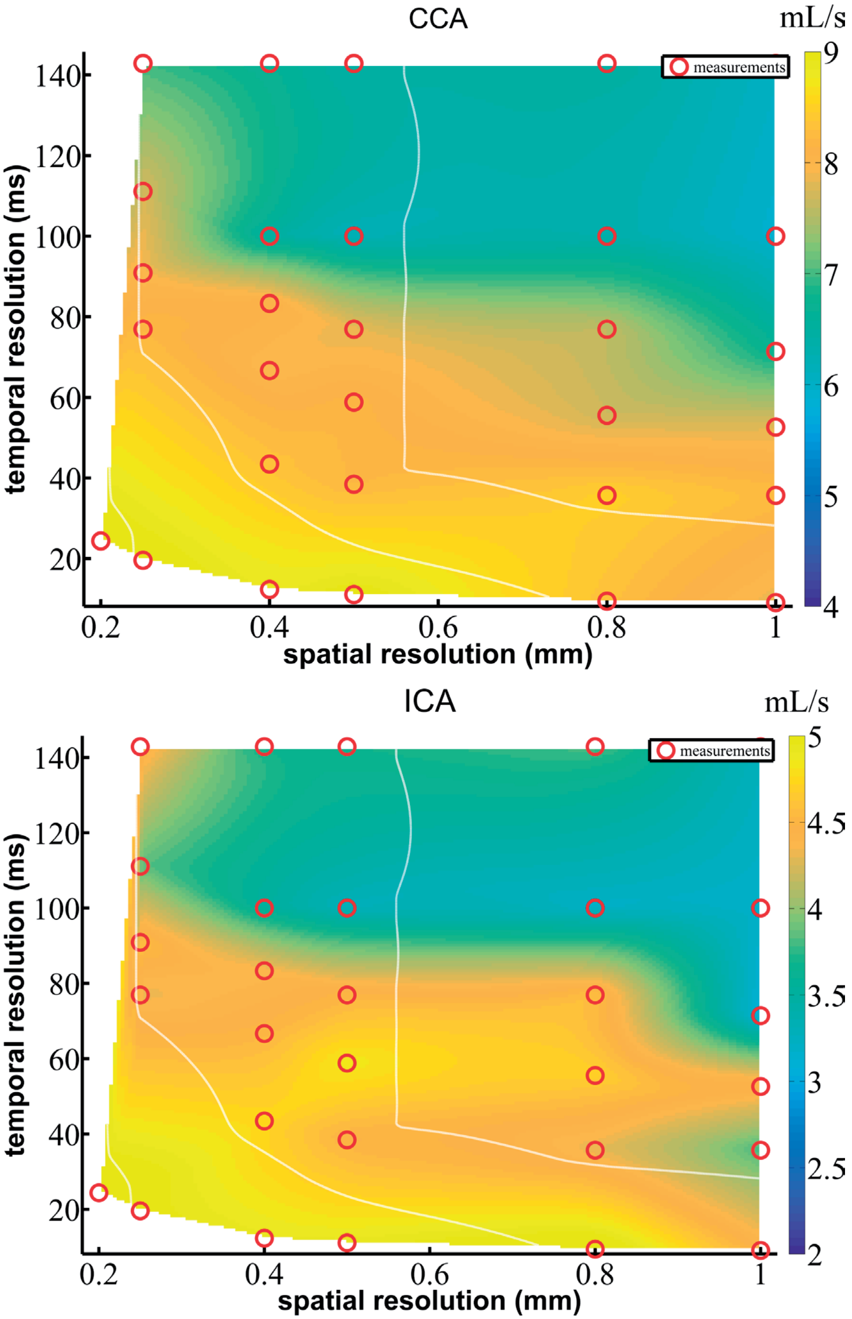

Figure 2A: Peak flow of a) CCA and b) ICA at different spatial and temporal resolutions. Red circles show the measurement points. White lines show the measurement durations of 18, 6 and 2 minutes (left to right).

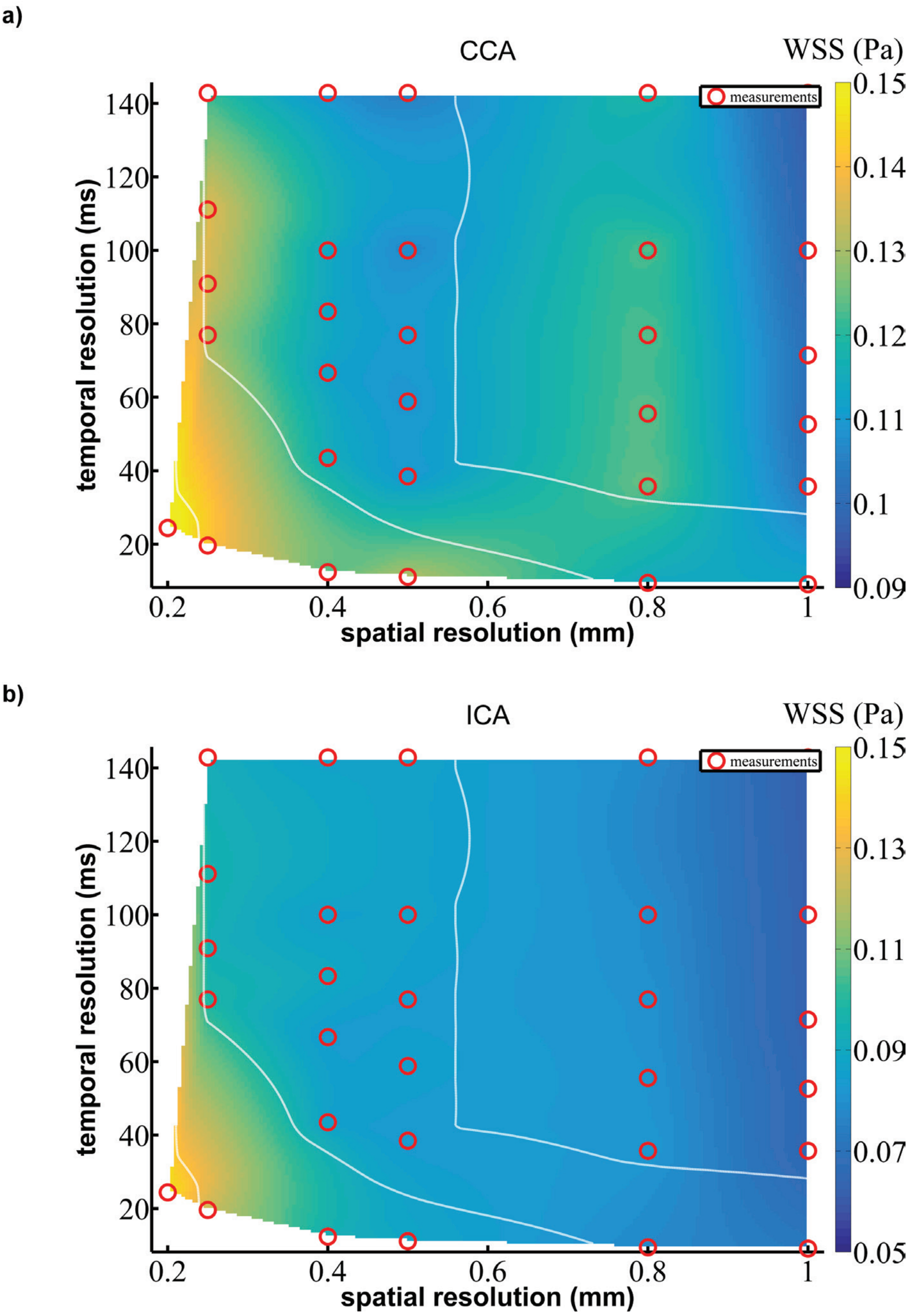

Figure 3A: WSS of a) CCA and b) ICA at different spatial and temporal resolutions. Red circles show the measurement points. White lines show the measurement durations of 18, 6 and 2 minutes (left to right).

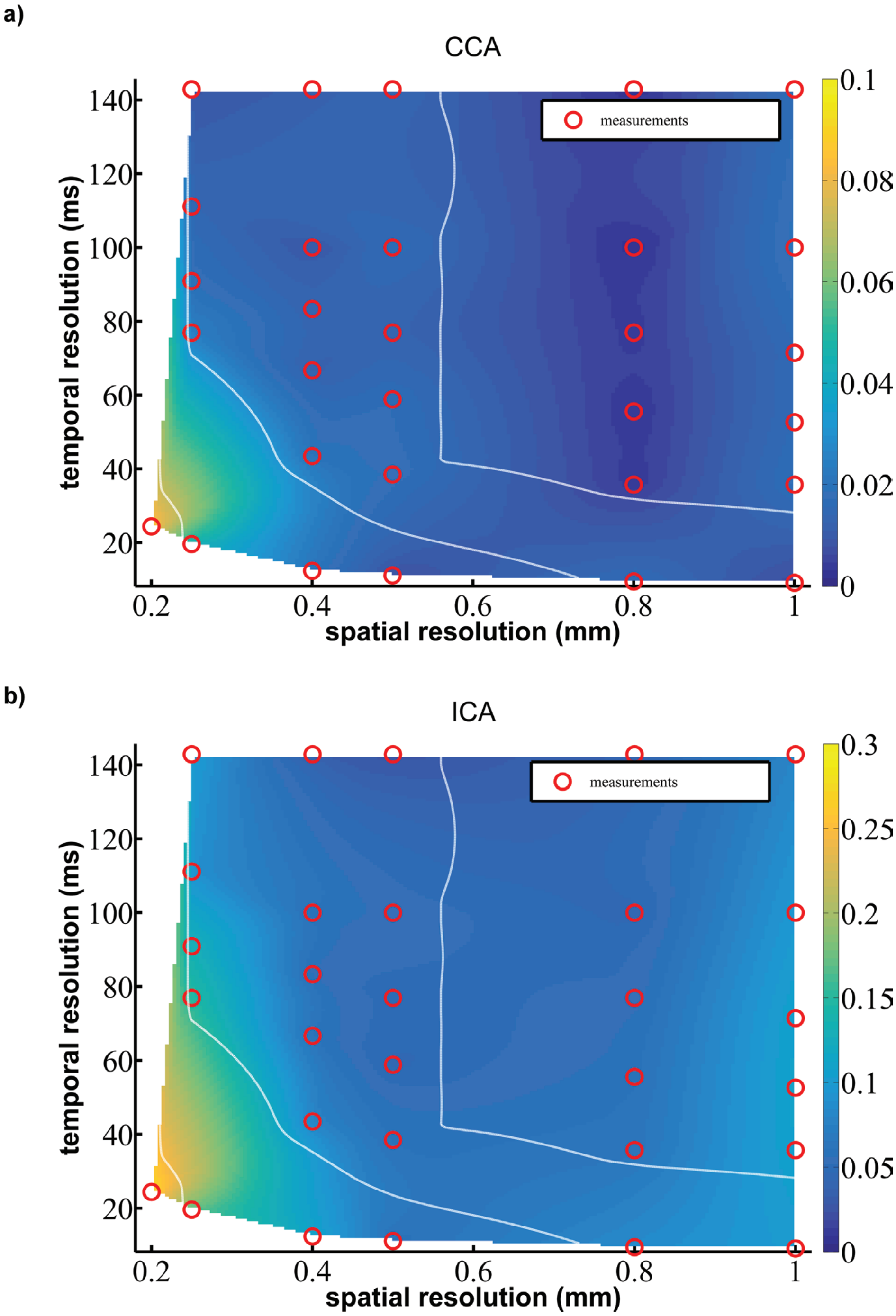

Figure 4A: OSI of a) CCA and b) ICA at different spatial and temporal resolutions. Red circles show the measurement points. White lines show the measurement durations of 18, 6 and 2 minutes (left to right).

Chapter 5

High wall shear stress relates to intra-plaque hemorrhage in asymptomatic carotid plaques

Based on:

Tuenter A, Selwaness M, Lorza AA, Schuurbiers J, Speelman L, Cibis M, van der Lugt A, de Bruijne M, van der Steen AFW, Franco O, Vernooij M, Wentzel JJ. High shear stress relates to intraplaque haemorrhage in asymptomatic carotid plaques.

Submitted

ABSTRACT

Introduction

Carotid artery plaques with vulnerable plaque components are related to a higher risk of cerebrovascular accidents. It is unknown which factors drive vulnerable plaque development. Shear stress, the frictional force of blood at the vessel wall, is known to influence plaque formation. We evaluated the association between shear stress and plaque components (intraplaque haemorrhage (IPH), lipid rich necrotic core (LRNC) and/or calcifications in plaques in carotid arteries with early atherosclerosis.

Methods

Participants (n= 74) from the population-based Rotterdam Study, all with carotid atherosclerosis assessed on ultrasound, underwent carotid MRI. Multiple MRI sequences were used to evaluate the presence of IPH, LRNC and/or calcifications in plaques in the carotid arteries. Images were automatically segmented for lumen and outer wall to obtain a 3D reconstruction of the carotid bifurcation. These reconstructions were used to calculate minimum, mean and maximum shear stresses by applying computational fluid dynamics with subject-specific inflow conditions. Associations between shear stress measures and plaque composition were studied using generalized estimating equations analysis, adjusting for age, sex and carotid wall thickness.

Results

The study group consisted of 93 atherosclerotic carotid arteries in 74 participants. In plaques with higher shear stresses, IPH was more often present (OR per unit increase in maximum shear stress (log transformed)= 12.14; p=0.001). Higher maximum shear stress was also significantly associated with the presence of calcifications (OR=4.28; p = 0.015).

Conclusion

Higher shear stress is associated with intraplaque haemorrhage and calcifications.

INTRODUCTION

Atherosclerosis in the carotid arteries is the major cause of ischemic stroke[1]. The composition of atherosclerotic plaques is an important predictor for plaque rupture and subsequent thromboembolic events[2]. The plaques with a thin fibrous cap, large lipid-rich necrotic core (LRNC), intraplaque haemorrhage (IPH) and increased plaque inflammation are considered the most vulnerable to rupture[3-5]. Conversely, the presence of calcifications has been associated with a more stable plaque phenotype[6,7].

The development of a vulnerable plaque is a complex process which is still not completely understood. Initially, plaque size and lumen obstruction were considered as the most important determinants of plaque vulnerability, but these explain variability in plaque rupture only to a limited extent[8]. One hypothesis is that plaque vulnerability may be influenced by hemodynamic forces occurring in blood vessels[9]. It is known that plaques develop at distinct sites in the arterial system, for instance, at the inner curve of the bending arteries, close to side branches and in the bulbs of the carotid arteries[10-12]. At these sites, the wall shear stress (WSS), which is the tangential stress exerted by the blood on the vessel wall, is mainly low and/or oscillatory. There is ample evidence that low WSS is involved in plaque initiation and progression through various molecular mechanisms that influence endothelial cell morphology and function[8,13-15]. In animal studies and small case studies an association between WSS and plaque composition was observed[16,17]. Although low WSS may induce plaque initiation, it has been hypothesized that plaque destabilization can be caused by high WSS on the plaque[9]. But to date, little is known about the association between WSS and plaque composition in human carotid arteries. Particularly, asymptomatic plaques have not yet been studied extensively in this respect. Understanding of plaque progression in the preclinical stage could however provide useful information for prevention.

Magnetic resonance imaging (MRI) has emerged as a non-invasive imaging modality that enables accurate identification of the main components of the atherosclerotic plaque[18]. Furthermore, it allows quantification of the blood flow through the artery, which can be used to derive the WSS on the vessel wall and plaque. The objective of this study was to evaluate the association between WSS and the different plaque components (IPH, LRNC and calcifications) in carotid arteries by combining MRI measurements and computational fluid dynamics (CFD) in asymptomatic participants with carotid atherosclerosis of a population-based cohort.

MATERIALS AND METHODS

Study population

This study was embedded within the Rotterdam Study, a prospective cohort study conducted in the Ommoord district of Rotterdam. The Rotterdam Study aims to study the causes and consequences of age-related diseases, including atherosclerosis, in a general middle-aged and elderly population (>45 years). The baseline visit started between 1990 and 1993 and participants were invited every 3 to 4 years for a range of examinations. Starting from October 2007, all participants were invited for an ultrasound of the carotid arteries. If the ultrasound showed arterial wall thickening of more than 2.5 mm in one of the carotid arteries, participants were invited for an MRI of both carotid arteries. Participants were excluded if there were contraindications for MRI, an endarterectomy was performed or if the image quality was poor[19]. For the present study, the MRI scans of the first 104 participants (208 carotid arteries) were chosen, as computational fluid dynamics is a very labour intensive measurement.

In 82 carotid arteries, MRI-based flow calculations could not be completed, mainly because of the problems in segmentation (carotid artery arms were cut off too short, arms were connected or images were unavailable). Subsequently, for 9 carotid arteries, WSS could not be calculated due to the convergence problems and of the remaining 117 carotid arteries, only 99 had a wall thickness of more than 1.5 mm. For 93 carotid arteries plaque composition information was available and for these carotid arteries (74 participants), the final analyses were done.

The Rotterdam Study has been approved by the medical ethics committee according to the Population Study Act Rotterdam Study, executed by the Ministry of Health Welfare and Sports of the Netherlands. All participants gave a written informed consent in order to participate in the study[20].

MRI of carotid arteries

Carotid plaque MR imaging was performed with a 1.5 Tesla scanner (GE Healthcare, Milwaukee, WI, USA) using a bilateral phased-array surface coil (Machnet, Eelde, the Netherlands). The total scanning time was about 30 minutes. The scanning protocol included multiple MR sequences[20]: four 2D axial sequence (a) PDw Fast Spin Echo (FSE) Black-blood (BB) sequence with fat suppression; (b) PDw-FSE-BB sequence with an increased in-plane resolution; (c) a PDw-EPI sequence; (d) T2w-EPI sequence, and two 3D sequences (I) 3DT1w- GRE sequence parallel to the common carotid artery, and (II) 3D phased-contrast MR Angiography. The sequence parameters have been described in detail elsewhere[19].

Determining plaque composition

Plaque composition was scored when the image quality of all MRI measurements was sufficient (image quality was scored ≥3 on a five-point scale). Two trained observers scored carotid artery plaques for the presence of three plaque components: lipid rich necrotic core, intraplaque haemorrhage and calcifications as described before[19]. IPH was defined as the presence of a hyperintense region of the atherosclerotic plaque on 3D-T1w-GRE. LRNC presence was defined as a hypointense region, not classified as intra-plaque haemorrhage or calcification, in the plaque on PDw-FSE or PDw-EPI and T2w-EPI images, or a region of relative signal intensity drop in the T2w-EPI images compared with the PDw-EPI images. Calcification was defined as the presence of a hypointense region in the plaque on all sequences. Inter-observer agreement was good for all measurements with Cohen's Kappa ranging from 0.86 (IPH and LRNC) to 0.94 (calcification)[19].

Wall shear stress calculations

WSS was calculated using an in-house written framework, 'the BioStress tool'. The BioStress tool is a matlab network that streamlines the various steps that need to be taken to calculate WSS using computational fluid dynamics (CFD). As an input for this tool the 3D lumen surface was segmented using an in-house developed validated automatic segmentation tool, detecting lumen and outer wall surface in the black-blood MRI and PDw-EPI images[21]. Subsequently, the BioStress tool was used for: I) smoothing the 3D lumen surface and outer wall to generate volume meshes; II) selecting the inflow and outflow conditions; III) creating a batch file with all measured patient specific inflow conditions as input for CFD simulations. The CCA flow was based on PC MRI measurements. To do so, the flow in the first 5 consecutive cross-sections in the CCA were calculated and the flow in these cross-sections were averaged to reduce the possible errors caused by inaccuracies of PC MRI.; IV) initiating the WSS calculation using computational fluid dynamics by execution of the finite element software package FIDAP. For the CFD calculations, the outflow of the ECA was set at 40% of the CCA flow, while the ICA was left stress free[22]. The steady state CFD simulations took 1 to 5 hours for each carotid artery. The WSS analyses were performed 12 mm proximal to the bifurcation and 13 mm distal from the bifurcation. By combining the WSS calculations with the wall thickness measurements, plaque areas with a wall thickness > 1.5 mm were detected and at those locations minimum (SS_{min}), mean (SS_{mean}) and maximum shear stress (SS_{max}) were determined.

Statistical analyses

WSS was not normally distributed and therefore log-transformed before running the analyses. Associations between shear stress across the plaque and plaque composition were studied using logistic regression analysis. A general linear model was used with as outcome parameter plaque composition and shear stress as determinant. This analysis was repeated for WSS quartiles. To correct for within-participant correlations between both carotid arteries, we used generalized estimating equation analysis. Associations were analysed in two models: model 1: adjusted for age and sex; and model 2: adjusted for age, sex and carotid wall thickness. Additional adjustment for wall thickness was performed since an increase in wall thickness potentially influences the lumen geometry and thus the local shear stress.

All analyses were performed using IBM SPSS statistics version 22. Data are expressed as mean ± standard deviation for quantitative variables and percentages for discrete variables. Associations between shear stress and plaque composition are presented as odds ratios with 95% confidence intervals (CI).

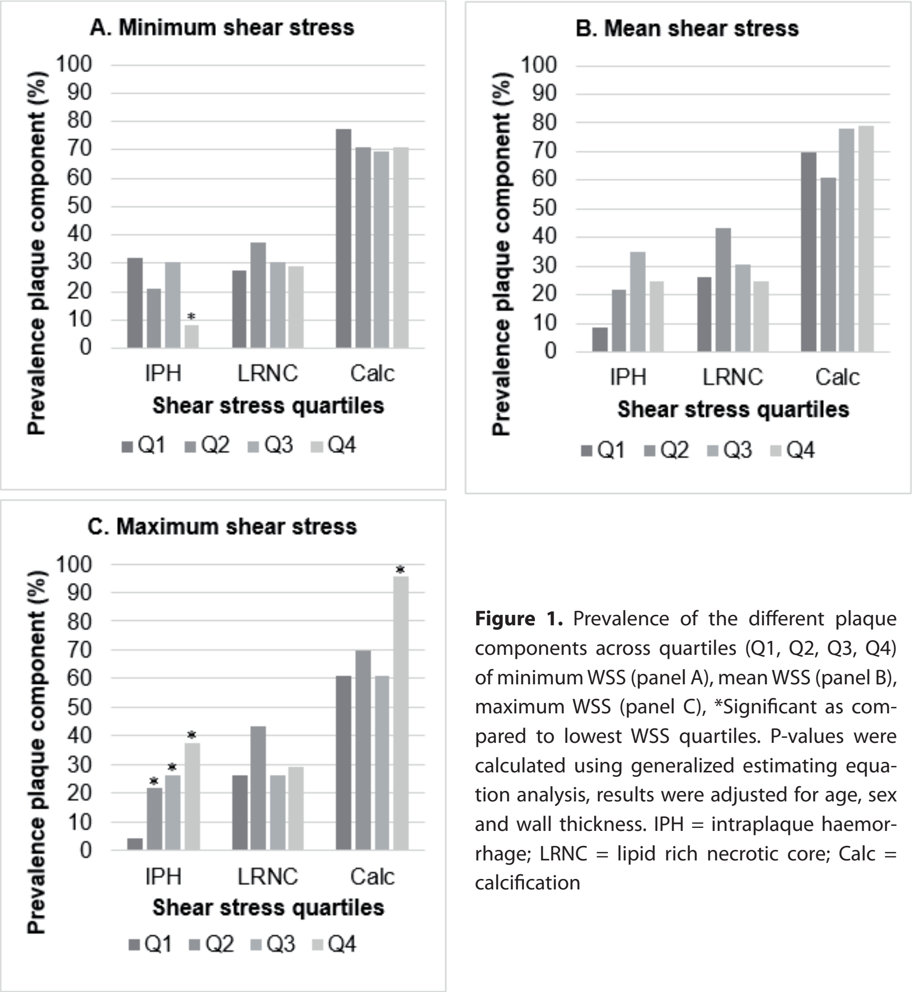

Figure 1. Prevalence of the different plaque components across quartiles (Q1, Q2, Q3, Q4) of minimum WSS (panel A), mean WSS (panel B), maximum WSS (panel C), *Significant as compared to lowest WSS quartiles. P-values were calculated using generalized estimating equation analysis, results were adjusted for age, sex and wall thickness. IPH = intraplaque haemorrhage; LRNC = lipid rich necrotic core; Calc = calcification

RESULTS

The baseline characteristics of the 74 asymptomatic participants are shown in Table 1. Mean age of the study population was 75 ±11 years, 50% of the participants were women and 73% of the participants had hypertension. Calcifications, LRNC and IPH were present in 72%, 31% and 22% of the carotid arteries, respectively. In Table 2 the results of the logistic regression analysis are presented relating WSS to plaque composition. Adjustments were made in 2 models: 1) adjusted for age and sex; 2) adjusted for age, sex and maximum wall thickness. A higher maximum WSS was associated with presence of IPH (odds ratio (OR) 12.14 (95% CI 3.21 – 45.94, P= 0.001 (model 2)). None of the WSS measures was significantly associated with the presence of a LRNC. Maximum WSS was related to the presence of calcifications with an OR 4.28 (95% CI 1.33 – 13.82, P= 0.015 (model 2)).

Table 1. Baseline characteristics of the study population

	Participants included in study (n=74)
Age (y)	74.8 (±10.5)
Women	37 (50%)
BMI (kg/m^2)	26.7 (±2.9)
Total cholesterol (mmol/L)	5.3 (±0.9)
HDL (mmol/L)	1.42 (±0.4)
Systolic blood pressure (mmHg)	144 (±21)
Diastolic blood pressure (mmHg)	79 (±11)
Hypertension*	54 (73%)
Current smokers	13 (18%)
Past smokers	39 (53%)
Diabetes Mellitus	12 (16%)
Percentage luminal stenosis	10.1 (±11.9)
Mean shear stress in plaque area(Pa)	1.1 (±1.1)

Values are means ± SD for continuous variables and percentages for dichotomous variables
*Hypertension: systolic blood pressure>=140 or diastolic blood pressure>= 90 or BP lowering medication with indication hypertension.

Figure 1 illustrates these results by showing the prevalence of the different plaque components across quartiles of WSS_{min}, WSS_{mean} and WSS_{max}. Higher maximum WSS showed a significant trend across the quartiles for IPH (p-trend= 0.013) and calcifications (p-trend = 0.011). Minimum/mean WSS quartiles were not significantly associated with presence of LRNC, IPH or calcifications.

Table 2. Odds ratios (95% confidence interval) calculated by generalized estimating equations analysis.

	LRNC	p	IPH	p	Calcification	p
WSS_{min}*						
Model 1	0.82 (0.36 – 1.86)	0.64	0.49 (0.14 – 1.76)	0.27	0.96 (0.43 – 2.14)	0.91
Model 2	0.94 (0.40 – 2.21)	0.89	0.53 (0.15 – 1.94)	0.34	1.06 (0.44 – 2.52)	0.90
WSS_{mean}*						
Model 1	1.32 (0.43 – 4.04)	0.63	3.10 (0.89 – 10.77)	0.08	2.55 (0.88 – 7.28)	0.08
Model 2	1.40 (0.44 – 4.44)	0.57	3.49 (0.94 – 12.97)	0.06	2.80 (0.93 – 8.47)	0.07
WSS_{max}*						
Model 1	1.12 (0.30 – 4.19)	0.86	12.35 (3.27 – 46.73)	**<0.01**	4.46 (1.39 – 14.31)	**0.01**
Model 2	1.10 (0.29 – 4.16)	0.89	12.14 (3.21 – 45.94)	**<0.01**	4.28 (1.33 – 13.82)	**0.02**

*log transformed
Model 1: adjusted for age, sex
Model 2: model 1 + adjusted for maximum wall thickness
LRNC = lipid rich necrotic core; IPH = intraplaque haemorrhage; WSS_{min}=minimum wall shear stress; WSS_{mean} = mean wall shear stress; WSS_{max} = maximum wall shear stress

DISCUSSION

In 74 persons with asymptomatic carotid atherosclerosis, who were sampled from a population-based setting, we evaluated the association between WSS and carotid plaque composition. We found an association between higher WSS and the presence of IPH and calcifications, but not LRNC. This association was independent from maximum plaque thickness.

Before discussing the implications of our findings, it is necessary to address some strengths and limitations. Although WSS calculations based on CFD were time consuming (up to 5 hours per carotid artery), it was feasible to repeat the calculations for 93 carotid arteries, which is a large dataset relative to the size of similar studies[23-26]. The population-based nature of our study increases generalizability of our data to other asymptomatic subjects with atherosclerosis.

For our calculations, we used individual-specific flow rates instead of standard flows, which allowed us to calculate absolute shear stress instead of relative shear stress and increases patient specificity. Unfortunately, the use of individual-specific flows challenges the statistical power of our analyses, as we were not able to calculate flow rates of a number of carotid arteries. This was partly caused by problems in the automated segmentation of the carotid bifurcation due to poor image quality. Therefore, it is important to optimize the imaging strategy and segmentation tool for future studies. The cross-sectional nature of our study limits the interpretation of cause and effect relation in the associations we found. Although we presumed that WSS induces changes in plaque composition, we cannot rule out the reverse association, i.e. that plaque composition altered the calculated WSS over the plaque.

We found that higher WSS relates to the presence of IPH. The pathophysiology of IPH is not completely clear, but the main existing hypothesis is that it develops by rupture of the vasa vasorum or immature neovessels[28]. IPH was shown to be associated with luminal stenosis, which can increase WSS[28]. This might imply that outward remodelling is not so effective if IPH is causing plaque growth. A possible explanation might be that IPH accelerates plaque growth and lumen narrowing. A potential confounder of this association is the wall thickness. Higher wall thickness is also associated with higher WSS, which is caused by the luminal stenosis, and the association holds also for more severe plaques, which often contain IPH. By adjusting for the maximum plaque thickness, we minimized the confounding effect of wall thickness. The association between high WSS and IPH is interesting as both parameters are investigated for their involvement in plaque vulnerability, plaque rupture and stroke[29].

WSS influences the development of an atherosclerotic plaque by affecting endothelial cell alignment and function[14]. For that reason, it is assumed that in areas with low or oscillatory shear stress lipids can more easily migrate into the vessel wall. We expected to find colocalization of low WSS areas with plaques containing a lipid rich necrotic core. Yet, this association was not seen in our study. To our opinion, the large variation in the stage of atherosclerosis in this population-based group influenced our results. Low WSS mainly plays a role in plaque initiation and the association between low WSS and LRNC may not be present in more developed plaques[15]. It is possible that in asymptomatic patients, WSS is already higher than average, even though the plaque does not cause severe stenosis.

The association we found between high WSS and the presence of calcifications can be partly caused by the high prevalence of calcifications in plaques that are more severe. During plaque development, WSS remains constant for a long period, but when plaque formation causes luminal stenosis, WSS starts to increase[30]. Luminal stenosis occurs in the presence of more developed plaques and possibly the association between presence of calcifications and high maximum WSS exists due to this pathophysiology. However, even after adjusting for maximum wall thickness we still found this association, suggesting that there are also other, unknown, factors that influence this relation.

In conclusion, we found that higher wall shear stress is associated with the presence of calcifications and intraplaque haemorrhage in atherosclerotic carotid plaques. More research is necessary to determine the causality between hemodynamic factors and plaque composition.

REFERENCES

[1] Hollander M, Bots ML, Del Sol AI, Koudstaal PJ, Witteman JC, Grobbee DE, et al. Carotid plaques increase the risk of stroke and subtypes of cerebral infarction in asymptomatic elderly: the Rotterdam study. Circulation. 2002;105(24):2872-7.

[2] Stary HC, Chandler AB, Dinsmore RE, Fuster V, Glagov S, Insull W, Jr., et al. A definition of advanced types of atherosclerotic lesions and a histological classification of atherosclerosis. A report from the Committee on Vascular Lesions of the Council on Arteriosclerosis, American Heart Association. Circulation. 1995;92(5):1355-74.

[3] Underhill HR, Yuan C, Yarnykh VL, Chu B, Oikawa M, Dong L, et al. Predictors of surface disruption with MR imaging in asymptomatic carotid artery stenosis. AJNR Am J Neuroradiol. 2010;31(3):487-93.

[4] Gupta A, Baradaran H, Schweitzer AD, Kamel H, Pandya A, Delgado D, et al. Carotid plaque MRI and stroke risk: a systematic review and meta-analysis. Stroke. 2013;44(11):3071-7.

[5] Schaar JA, Muller JE, Falk E, Virmani R, Fuster V, Serruys PW, et al. Terminology for high-risk and vulnerable coronary artery plaques. Report of a meeting on the vulnerable plaque, June 17 and 18, 2003, Santorini, Greece. Eur Heart J. 2004;25(12):1077-82.

[6] Wu B, Pei X, Li ZY. How does calcification influence plaque vulnerability? Insights from fatigue analysis. ScientificWorldJournal. 2014;2014:417324.

[7] Wong KK, Thavornpattanapong P, Cheung SC, Sun Z, Tu J. Effect of calcification on the mechanical stability of plaque based on a three-dimensional carotid bifurcation model. BMC Cardiovasc Disord. 2012;12:7.

[8] Sadat U, Teng Z, Gillard JH. Biomechanical structural stresses of atherosclerotic plaques. Expert Rev Cardiovasc Ther. 2010;8(10):1469-81.

[9] Groen HC, Gijsen FJ, van der Lugt A, Ferguson MS, Hatsukami TS, Yuan C, et al. High shear stress influences plaque vulnerability Part of the data presented in this paper were published in Stroke 2007;38:2379-81. Neth Heart J. 2008;16(7-8):280-3.

[10] Zarins CK, Giddens DP, Bharadvaj BK, Sottiurai VS, Mabon RF, Glagov S. Carotid bifurcation atherosclerosis. Quantitative correlation of plaque localization with flow velocity profiles and wall shear stress. Circ Res. 1983;53(4):502-14.

[11] Asakura T, Karino T. Flow patterns and spatial distribution of atherosclerotic lesions in human coronary arteries. Circ Res. 1990;66(4):1045-66.

[12] Gnasso A, Irace C, Carallo C, De Franceschi MS, Motti C, Mattioli PL, et al. In vivo association between low wall shear stress and plaque in subjects with asymmetrical carotid atherosclerosis. Stroke. 1997;28(5):993-8.

[13] Dai G, Kaazempur-Mofrad MR, Natarajan S, Zhang Y, Vaughn S, Blackman BR, et al. Distinct endothelial phenotypes evoked by arterial waveforms derived from atherosclerosis-susceptible and -resistant regions of human vasculature. Proc Natl Acad Sci U S A. 2004;101(41):14871-6.

[14] Malek AM, Alper SL, Izumo S. Hemodynamic shear stress and its role in atherosclerosis. JAMA. 1999;282(21):2035-42.

[15] Gimbrone MA, Jr., Topper JN, Nagel T, Anderson KR, Garcia-Cardena G. Endothelial dysfunction, hemodynamic forces, and atherogenesis. Ann N Y Acad Sci. 2000;902:230-9; discussion 9-40.

[16] Chatzizisis YS, Jonas M, Coskun AU, Beigel R, Stone BV, Maynard C, et al. Prediction of the localization of high-risk coronary atherosclerotic plaques on the basis of low endothelial shear stress: an intravascular ultrasound and histopathology natural history study. Circulation. 2008;117(8):993-1002.

[17] Cheng C, Tempel D, van Haperen R, de Boer HC, Segers D, Huisman M, et al. Shear stress-induced changes in atherosclerotic plaque composition are modulated by chemokines. J Clin Invest. 2007;117(3):616-26.

[18] Yuan C, Mitsumori LM, Ferguson MS, Polissar NL, Echelard D, Ortiz G, et al. In vivo accuracy of multispectral magnetic resonance imaging for identifying lipid-rich necrotic cores and intraplaque hemorrhage in advanced human carotid plaques. Circulation. 2001;104(17):2051-6.

[19] van den Bouwhuijsen QJ, Vernooij MW, Hofman A, Krestin GP, van der Lugt A, Witteman JC. Determinants of magnetic resonance imaging detected carotid plaque components: the Rotterdam Study. Eur Heart J. 2012;33(2):221-9.

[20] Hofman A, Darwish Murad S, van Duijn CM, Franco OH, Goedegebure A, Ikram MA, et al. The Rotterdam Study: 2014 objectives and design update. Eur J Epidemiol. 2013;28(11):889-926.

[21] Arias A, Petersen J, van Engelen A, Tang H, Selwaness M, Witteman JM, et al. Carotid Artery Wall Segmentation by Coupled Surface Graph Cuts. In: Menze B, Langs G, Lu L, Montillo A, Tu Z, Criminisi A, editors. Medical Computer Vision Recognition Techniques and Applications in Medical Imaging: Springer Berlin Heidelberg; 2013. p. 38-47.

[22] Groen HC, Simons L, van den Bouwhuijsen QJ, Bosboom EM, Gijsen FJ, van der Giessen AG, et al. MRI-based quantification of outflow boundary conditions for computational fluid dynamics of stenosed human carotid arteries. J Biomech. 2010;43(12):2332-8.

[23] Gallo D, Steinman DA, Morbiducci U. An insight into the mechanistic role of the common carotid artery on the hemodynamics at the carotid bifurcation. Ann Biomed Eng. 2015;43(1):68-81.

[24] Lee SW, Antiga L, Spence JD, Steinman DA. Geometry of the carotid bifurcation predicts its exposure to disturbed flow. Stroke. 2008;39(8):2341-7.

[25] Tang D, Kamm RD, Yang C, Zheng J, Canton G, Bach R, et al. Image-based modeling for better understanding and assessment of atherosclerotic plaque progression and vulnerability: data, modeling, validation, uncertainty and predictions. J Biomech. 2014;47(4):834-46.

[26] Yang C, Canton G, Yuan C, Ferguson M, Hatsukami TS, Tang D. Impact of flow rates in a cardiac cycle on correlations between advanced human carotid plaque progression and mechanical flow shear stress and plaque wall stress. Biomed Eng Online. 2011;10(61):10-61.

[27] Takaya N, Yuan C, Chu B, Saam T, Polissar NL, Jarvik GP, et al. Presence of intraplaque hemorrhage stimulates progression of carotid atherosclerotic plaques: a high-resolution magnetic resonance imaging study. Circulation. 2005;111(21):2768-75.

[28] Gijsen F, van der Giessen A, van der Steen A, Wentzel J. Shear stress and advanced atherosclerosis in human coronary arteries. J Biomech. 2013;46(2):240-7.

[29] Wentzel JJ, Janssen E, Vos J, Schuurbiers JC, Krams R, Serruys PW, et al. Extension of increased atherosclerotic wall thickness into high shear stress regions is associated with loss of compensatory remodeling. Circulation. 2003;108(1):17-23.

Part 2

Univentricular heart repaired by Fontan operation

Chapter 6

The effect of resolution on viscous dissipation measured with 4D flow MRI in patients with Fontan circulation: Evaluation using computational fluid dynamics

Based on:

Cibis M, Jarvis K, Markl M, Rose M, Rigsby C, Barker AJ, Wentzel JJ, The effect of resolution on viscous dissipation measured with 4D flow MRI in patients with Fontan circulation: Evaluation using computational fluid dynamics. Journal of Biomechanics 2015 Sep 18;48(12):2984-9

ABSTRACT

Viscous dissipation inside Fontan circulation, a parameter associated with the exercise intolerance of Fontan patients, can be derived from computational fluid dynamics (CFD) or 4D flow MRI velocities. However, the impact of spatial resolution and measurement noise on the estimation of viscous dissipation is unclear. Our aim was to evaluate the influence of these parameters on viscous dissipation calculation. 6 Fontan patients underwent whole heart 4D flow MRI. Subject-specific CFD simulations were performed. The CFD velocities were down-sampled to isotropic spatial resolutions of 0.5 mm, 1mm, 2 mm and to MRI resolution. Viscous dissipation was compared between 1) high resolution CFD velocities, 2) CFD velocities down-sampled to MRI resolution, 3) down-sampled CFD velocities with MRI mimicked noise levels, and 4) in-vivo 4D flow MRI velocities. Relative viscous dissipation between subjects was also calculated. 4D flow MRI velocities (15.6±3.8cm/s) were higher, although not significantly different than CFD velocities (13.8±4.7cm/s, p= 0.16), down-sampled CFD velocities (12.3± 4.4cm/s, p= 0.06) and the down-sampled CFD velocities with noise (13.2± 4.2cm/s, p= 0.06). CFD-based viscous dissipation (0.81±0.55mW) was significantly higher than those based on down-sampled CFD (0.25±0.19 mW, p= 0.03), down-sampled CFD with noise (0.49±0.26mW, p=0.03) and 4D flow MRI (0.56±0.28mW, p= 0.06). Nevertheless, relative viscous dissipation between different subjects was maintained irrespective of resolution and noise, suggesting that comparison of viscous dissipation between patients is still possible.

INTRODUCTION

Hypoplastic left or right heart syndrome is among the most severe congenital heart diseases, typically requiring multiple successive surgical interventions to reconstruct the cardiovascular system into a single ventricle physiology[1]. The final surgical procedure creates the total cavo-pulmonary connection (TCPC), also known as Fontan circulation, which results in systemic venous return being supplied directly to the lungs through the pulmonary arteries without passing through the right ventricle[2]. Although advances in surgical procedures and treatment have significantly improved life expectancy of these patients, long term drawbacks such as exercise intolerance exist. Recent studies have suggested that limited exercise tolerance of Fontan patients might be associated with complex flow patterns and specifically elevated viscous dissipation inside the Fontan connection[3]. Khiabani et al[4] reported an inverse relationship between viscous dissipation and oxygen consumption during exercise in a cohort study of thirty two Fontan patients. Haggerty et al[5] showed an inverse relationship between viscous dissipation and systemic venous flow and cardiac index in a cohort study of hundred Fontan patients. These results suggest that the ability to directly measure viscous dissipation in-vivo might shed extra light on Fontan function and risk for impaired outcome in these patients.

Typically, viscous dissipation is calculated by solving the mechanical energy balance equation[6,7]. This approach requires pressure, which is determined either by invasive measurements or computational fluid dynamics (CFD) simulations. Patient specific CFD simulations have been used in a number of studies to derive viscous dissipation and have provided a better understanding of the impact of the individual Fontan geometry on Fontan hemodynamics[8-13]. However, CFD relies on the accurate definition of geometric and in-flow boundary conditions and requires non-clinical expertise, engineering tools, powerful computer systems and extensive computational time. Due to these requirements and limitations, it is challenging to include CFD in routine clinical practices. Alternatively, viscous dissipation can be calculated using the viscous term of the Navier-Stokes equation[14,15]. This approach bypasses the need for the pressure and requires only the blood flow velocities inside the TCPC, which can be non-invasively obtained in-vivo by 4D flow MRI (time-resolved 3D phase contrast MRI with 3-directional velocity encoding)[16,17]. However, the 4D flow MRI based velocities are expected to result in under-resolved viscous dissipation since the dissipation term involves spatial derivatives of the velocity field and the low spatial resolution of MR images causes underestimation of the spatial derivatives. Nevertheless, we hypothesize that under-resolved viscous dissipation might still be sufficient to detect the cases with relatively high viscous dissipation which is clinically more important than obtaining the absolute magnitude of viscous dissipation.

In this study, we firstly aim to analyze the effect of resolution and noise of the velocity field on the estimated viscous dissipation of Fontan patients. In order to study the effect of spatial resolution, we performed subject specific CFD simulations and we generated MRI-like data by down-sampling the CFD velocities to different resolutions. Secondly, we aim to compare patient-specific 4D flow MRI and CFD based viscous dissipation. We compared four results obtained with: 1) CFD velocities at high resolution, 2) CFD velocities down-sampled to MRI resolution, 3) down-sampled CFD velocities with subject-specific noise added posteriori, 4) in-vivo 4D flow MRI velocities.

THEORY

The viscous dissipation per unit volume can be calculated by the associated term of the Navier Stokes equation in laminar flow regimes:

$$\phi_{VD} = \frac{1}{2}\mu \sum_i \sum_j \left[\left(\frac{\partial \mu}{\partial \chi_i} + \frac{\partial \mu}{\partial \chi_j} \right) - \frac{2}{3} (\Delta \cdot \nu)\, \delta_{ij} \right]^2 \qquad \text{Eq.1}$$

where ϕ_{VD} is viscous dissipation per unit volume based on viscous dissipation term and μ is the dynamic viscosity. $\delta_{ij} = 1$ for $i=j$ and $\delta_{ij} = 0$ for $i \ddagger j$, i and j are the principal directions x, y, z[18]. Eq.1 consists of dynamic viscosity and the spatial derivatives of velocity field. Viscous dissipation per unit volume can therefore be calculated by Eq.1 if velocity field is known, e.g. by 4D flow MRI measurements. Total viscous dissipation is calculated by the integral of unit viscous dissipation (Eq.1):

$$\int \phi_{VD} dV = \sum_{i=1}^{\nu o \chi els} \phi_{VD} V_i \qquad \text{Eq. 2}$$

METHODS

Study Cohort and MR Imaging

Six Fontan patients underwent MRI scans (ages: 9-21 years, gender: 5 male, operation type: 4 extra cardiac conduit and 2 lateral tunnel) with coverage of the heart and great arteries using a 1.5 T system (Avanto or Aera, Siemens, Germany). ECG synchronized and diaphragm navigator gated 4D flow MRI was performed during free breathing. All data were acquired with three directional velocity encoding (3D spatial resolution: 1.9- 2.5x 1.9- 2.5x 2.2- 3.3 mm^3, temporal resolution: 38.4- 41.6ms, venc: 100- 150 cm/s, TE: 2.4- 2.7ms, TR: 4.8- 5.2ms, flip angle: 15°). The scan time was in the range of 6 to 12 minutes including the navigator gating efficiency. All scans were performed using navigator respiration gating with scan efficiencies ranging from 60-80% and with accelerated imaging. Four scans were performed using regular GRAPPA with acceleration factor of R=2 and k-t GRAPPA (R=5) was available for the last two scans. Post-processing of 4D flow MRI data included corrections for Maxwell terms, eddy current induced phase offsets, and velocity aliasing[19-21]. The study was approved by our local Institutional Review Board and informed consent was obtained from all participants or their parents.

Segmentation and meshing

3D segmentation of the Fontan geometry was performed manually on the time-averaged magnitude images using an open source segmentation tool, ITK-SNAP[22]. The segmentations included IVC, superior vena cava (SVC) and left and right pulmonary arteries (LPA and RPA) with the segmental branches excluded. The segmentations were then converted into volumetric meshes of tetrahedral elements using GAMBIT. The mesh size of 0.6 mm was chosen after performing a mesh independency study using a generic t-shape model. The volumetric meshes were used to conduct CFD simulations.

CFD simulations

All CFD simulations were performed using the commercial finite element software FIDAP V.8.7.4 (ANSYS) on a standard desktop computer (Intel Xeon six core processor, 2.40 GHz CPU and 12 GB RAM). Time resolved IVC, SVC, LPA and RPA flows were calculated at the inlets and outlets of the geometry using 4D flow MRI measurements. The LPA and RPA flows were corrected to match inflow (sum of IVC and SVC flows) while maintaining their split ratio. IVC, SVC and RPA velocity profiles were preserved and used as boundary conditions in CFD simulations. LPA boundary was left as stress free. The walls were assumed as rigid and no-slip condition was prescribed. Blood density was assumed to be 1.06 g/cm^3 and viscosity was assumed to obey the Carreau-Yasuda model[23]. For the simulations, we chose a pressure-based segregated algorithm and the backward Euler method for time integration. The convergence criterion was set to 0.1%. Time resolved CFD simulations were performed for 2 cardiac cycles with time intervals of 3 ms. The results of the 2nd cardiac cycle were analysed. The Reynolds number at the inlets and outlets was 165±77.

Down-sampling velocities

Firstly, the velocities obtained from CFD were mapped into equally spaced grids with resolution of 0.1 mm, followed by 3D convolution integration with a 3D Gaussian operator[24,25]. Afterwards, down-sampled velocities were obtained by averaging the high resolution velocities within the voxels of the down-sampled grid[26].

Viscous dissipation calculations

We calculated viscous dissipation by using Eq.1 and Eq.2 at the time point with highest inflow (sum of IVC and SVC flows). The under-resolved viscous dissipation was calculated at isotropic resolutions of 0.5 mm, 1.0 mm, and 2.0 mm and at patient-specific MRI resolution. The subject specific noise, which was defined as the standard deviation of measured velocities in static regions, was added to the velocities down-sampled to MRI resolution and under-resolved viscous dissipation was calculated also after adding noise.

Analysis

The under-resolved viscous dissipations obtained with down-sampled CFD velocities were quantified. The velocity and the viscous dissipation fields are only qualitatively compared with the maximum intensity projection (MIP) visualization. We compared the mean velocity and the viscous dissipation obtained from 1) CFD velocities at resolution of 0.1 mm, 2) the CFD velocities down-sampled to MRI resolution, 3) the down-sampled CFD velocities with added noise and 4) the patient-specific 4D flow MRI velocities. Relative viscous dissipation of each subject was also calculated by dividing viscous dissipation by the mean viscous dissipation of all subjects.

All numbers were reported as mean± standard deviation. Differences between CFD and 4D flow MRI derived findings were analyzed using the Wilcoxon signed rank test, $p<0.05$ was considered statistically significant.

RESULTS

The CFD based viscous dissipation at resolution of 0.1 mm and the under-resolved viscous dissipation obtained with the CFD velocities down-sampled to the resolutions of 0.5 mm, 1.0 mm and 2.0 mm are shown in Figure 1. CFD based viscous dissipation was 0.81±0.55 mW and under-resolved viscous dissipation was 0.60±0.41 mW at resolution of 0.5 mm, 0.45±0.30 mW at resolution of 1.0 mm and 0.27±0.19 mW at resolution of 2.0 mm.

MIPs of the 3D velocity and viscous dissipation fields of all six Fontan cases are shown in Figure 2. Blood flow velocities were generally lower and more uniform in the SVC, while higher velocities were found in the IVC and pulmonary arteries. In addition, high velocities and velocity

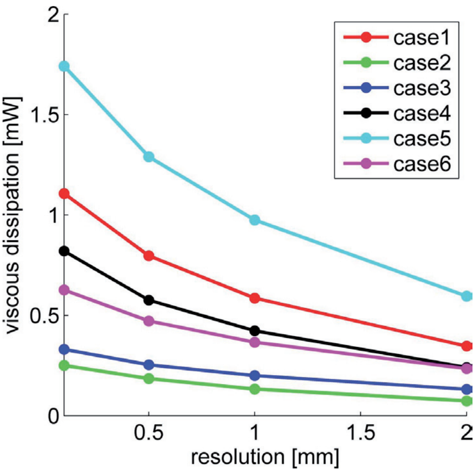

Figure 1. Viscous dissipation calculated with the CFD velocities at resolution of 0.1 mm and with the CFD velocities down-sampled to isotropic resolutions of 0.5 mm, 1.0 mm and 2.0 mm.

gradients were observed in the Fontan junctions. Viscous dissipation was found to be larger in the junction and the pulmonary arteries due to colliding IVC and SVC flows and thus complex flow patterns. The velocity and viscous dissipation patterns were generally in good agreement between CFD and 4D flow MRI based results although discrepancies were observed in some cases.

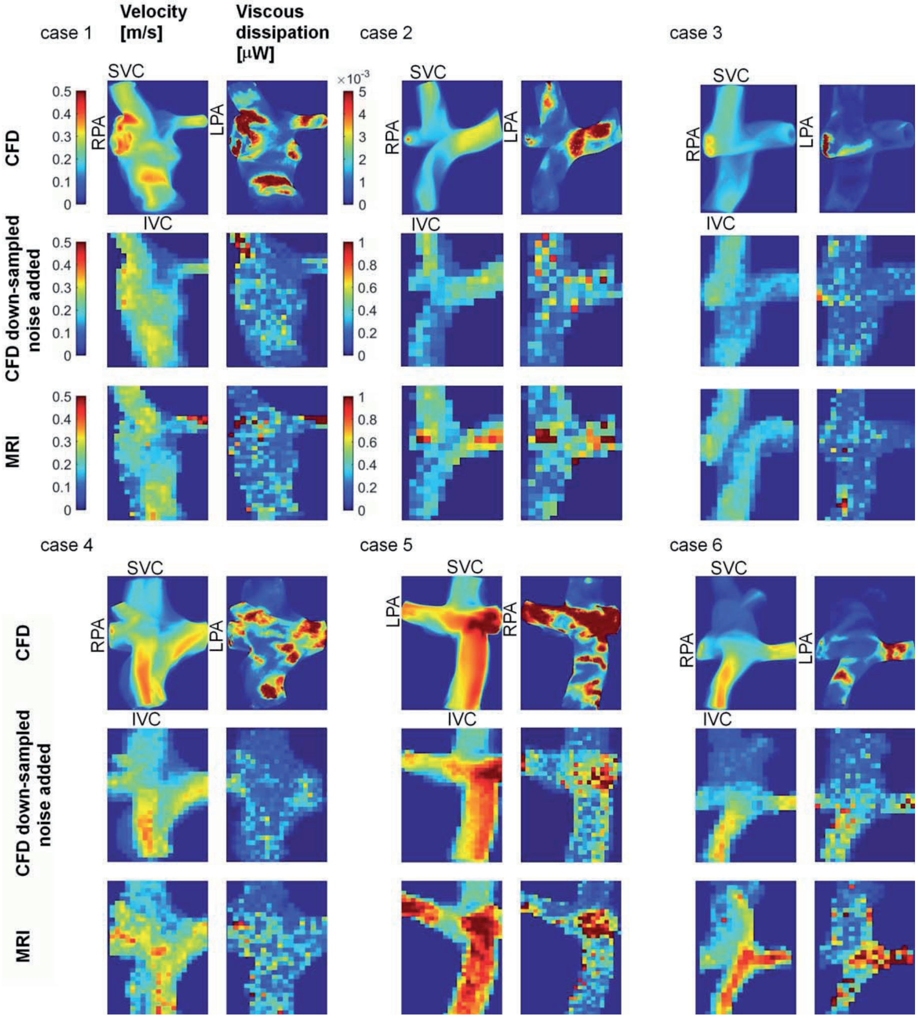

Figure 2. MIP of velocity (Left) and viscous dissipation (Right) fields obtained by CFD, down-sampled CFD with added noise and 4D flow MRI are shown for each subject. The color-maps given for case 1 are valid for all subjects. Note that the color-map scale of CFD-based viscous dissipation was 200 times smaller than others since the volume of the voxels in CFD was ~1000 times smaller than those in MRI. Hence viscous dissipation per voxel was also smaller.

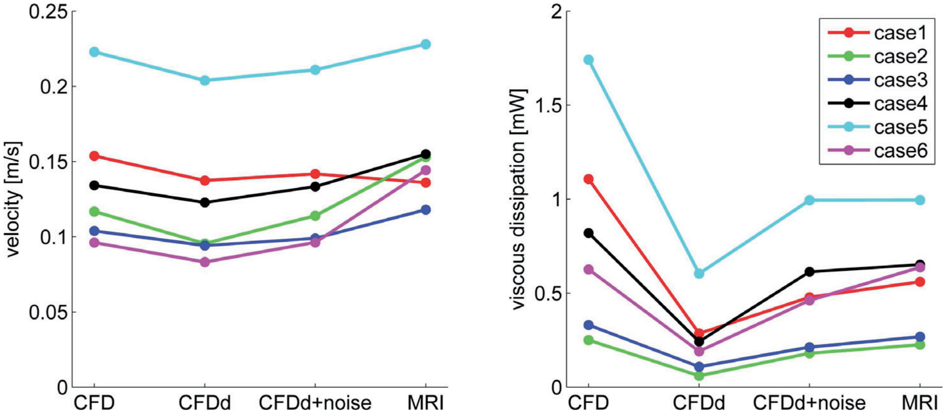

Figure 3. Mean velocity [m/s] (left) and viscous dissipation [mW] (right) by using velocities of CFD, down-sampled CFD velocities without noise (CFDd) , down-sampled CFD velocities with noise added (CFDd+noise) and MRI measurements. Each color represents different case.

Velocity and viscous dissipation averaged over the Fontan connection for all subjects are shown in Figure 3. The 4D flow MRI measured velocities (15.6±3.8 cm/s) were higher although not significantly different than the CFD based velocities (13.8±4.7 cm/s, p=0.16), down-sampled CFD based velocities (12.3±4.4 cm/s, p=0.06) and the down-sampled CFD velocities with noise (13.2±4.2 cm/s, p=0.06). Viscous dissipation based on CFD velocities (0.81±0.55 mW) was significantly higher than others. Down-sampling CFD velocities resulted in significant underestimation of viscous dissipation (0.25±0.19 mW, p=0.03). Adding noise increased viscous dissipation in down-sampled CFD (0.49±0.26 mW, p=0.03), but the values remained lower than 4D flow MRI derived findings (0.56±0.28 mW, p=0.06). Despite differences in magnitude of viscous dissipation, no significant difference was found between relative viscous dissipations calculated with CFD, down sampled CFD with and without noise and MRI velocities (p=0.56). Relative viscous dissipation changed by 0±29% between high resolution CFD and MRI based calculations. Relative viscous dissipation of all subjects calculated by 4 velocity types is shown in Figure 4.

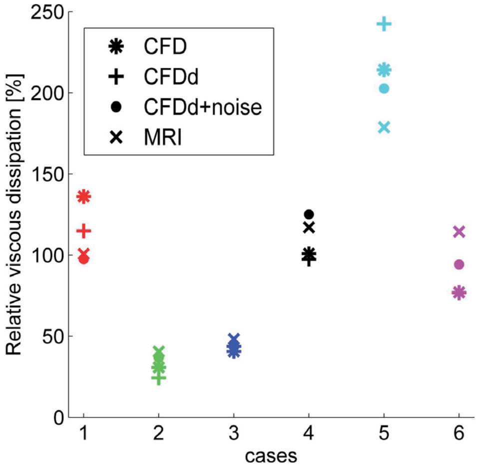

Figure 4. Relative viscous dissipation [%] per subject calculated using CFD velocities, down-sampled CFD velocities without noise (CFDd), down-sampled CFD velocities with noise added (CFDd+noise) and MRI measurements.

DISCUSSION

The aim of our study was to investigate the influence of resolution and noise of 4D flow MRI velocities on in vivo viscous dissipation. The effect of spatial resolution of 4D flow MRI was studied by down-sampling patient-specific CFD simulations and creating MRI-like data instead of performing MRI measurements at several resolutions. This was necessary since in vivo MRI scans at different resolutions were not feasible due to long scan times required for 4D flow MRI.

Down-sampling the velocities resulted in under-resolved viscous dissipation and we found a nonlinear inverse relationship between spatial resolution and the estimated viscous dissipation. The viscous dissipation calculated with CFD velocities at resolution of 0.1 mm was 66±4% larger than that based on CFD velocities down-sampled to the isotropic resolution of 0.2 mm. This large underestimation of viscous dissipation was due to the complex flow and larger velocity gradients which were missing after down-sampling. The effect of down-sampling on viscous dissipation was however very consistent for all patients. Adding noise to the down-sampled velocities caused an increase in the estimated viscous dissipation due to increase in spatial gradients around noisy data. While lowering the resolution decreased the magnitude of estimated viscous dissipation, we set out to understand if relative relationships between subjects were retained. Regardless of measurement noise and spatial resolution, the relative viscous dissipation between subjects was obtained similarly by the CFD and MRI based calculations. This was due to the fact that CFD and MRI based velocity patterns and the regions of high and low velocity gradients were mostly in good agreement.

At peak flow, the mean of the Reynolds numbers at inlet and outlets was 165±77 which is lower than Reynolds numbers that would cause transition to turbulence. Therefore, use of viscous dissipation term of the Navier-Stokes equations was possible. Under exercise conditions, however, the flow can be transitionally turbulent which might require the analysis including the dissipation due to turbulence.

Although not significant, the MRI-based mean velocity was higher than that based on CFD in five out of six cases. We imposed MRI measured velocities as boundary conditions for CFD and we preserved the velocity profile as measured by 4D flow MRI. After imposing velocities, we forced the velocities at near wall elements to zero to satisfy slip boundary condition which reduced the mean of the velocities within the volume resulted in deviations between MRI and CFD based mean velocities.

The accuracy of the velocities measured by 4D flow MRI and consequently the accuracy of the estimated viscous dissipation were influenced by the magnitude of velocities and the venc defined. Since there is a linear relationship between magnitude of velocity and the velocity to noise ratio (VNR), the higher velocities were expected to be more accurate. One can therefore expect that the estimated unit viscous dissipation is more accurate at regions of higher velocities.

The study of Venkatachari et al[15] was the first to calculate viscous dissipation in experimental phantoms using the viscous dissipation term of the Navier Stokes equation with velocities measured by MRI. Barker et al[14] conducted a study to obtain in vivo viscous dissipation by viscous dissipation term of the Navier Stokes equation in patients with aortic diseases but the results were not validated. To our knowledge our study is the first that investigates in-vivo viscous dissipation based on MRI and CFD and verifies the potential of MRI-based viscous dissipation calculation in detecting the cases with high viscous dissipation.

The viscous dissipation inside Fontan circuit varies within a wide range of values depending on many parameters such as the age of the subject, amount of blood flow, the operation type, and size of the conduit[6]. Most of the viscous dissipation values calculated in our study were within the range of the values reported in the literature. In the study of Bossers et al, they calculated losses under simulated exercise which increases blood flow and causes higher viscous dissipation in the range of 0.6-7.7 mW in their recent study which they also excluded segmental branches. Other studies reported 5-10 times larger viscous dissipation[21,27] since they included segmental branches.

In this study, our intention was not to perform PC MRI simulations by solving the Bloch equations. Instead we generated PC MRI like data to study the effect of resolution and noise by mimicking MRI velocities by down-sampling the velocities into lower resolutions and adding subject-specific noise posteriori.

This study is clearly limited by the small size but the primary purpose was to understand the impact of imaging parameters and methodological approach played in the computation of viscous dissipation. Secondly, the patient data was collected at different spatial resolutions but ideally the data should have been collected with the same resolution. Also of note, is that the segmentations were performed using time-averaged images and wall motion was neglected. Furthermore, Venc was sub-optimally chosen being two times higher than the maximum velocity inside the Fontan circulation to measure velocities inside heart and aorta and thereby resulting in a lower signal to noise ratio.

Clinical Implications

Viscous dissipation inside TCPC has been of interest since it is related to TCPC resistance and contributes to the limited outcome of these patients. Gathering information on viscous dissipation might therefore be useful for clinical assessment of Fontan patients. Calculation of viscous dissipation by using 4D flow MRI velocities is straightforward hence easily applicable to the clinical routine. The main drawback of using 4D flow MRI is that it causes underestimation of the magnitude of viscous dissipation. One remedy might be increasing the spatial resolution of MRI measurements. Despite underestimation of viscous dissipation due to resolution, when CFD and MRI based results were compared, relative viscous dissipation between subjects remained the same. These results suggest that although the magnitude of viscous dissipation might be difficult to ascertain accurately, Fontan circuits with comparable or elevated viscous dissipation can still be captured by using an approach which employs MRI velocities. Therefore, use of viscous dissipation term and MRI velocities at low resolution can still lead to valid conclusions in comparative studies which make use of similar image resolution.

The under-resolved viscous dissipation can be used in the clinics only after a large number of reference datasets are obtained by using a consistent protocol. Therefore, more clinically oriented studies have to be performed which involve the assessment of exercise capacity of Fontan patients and the under-resolved viscous dissipation within a larger patient population to set a threshold value for clinical decisions.

CONCLUSION

In this study, viscous dissipation was calculated using the viscous dissipation term of the Navier-Stokes equation. This approach has the advantage of bypassing the need for pressure, since it requires information only on the velocity field. However, the trade-off is that viscous dissipation is under resolved if the spatial resolution of the velocity field is low, such as in 4D flow MRI measurements. Nevertheless, we found that the ranking of patient-specific viscous dissipation was retained within the patient group at different spatial resolution of the velocities and also after noise added. We therefore suggest that the subjects with elevated viscous dissipation can be detected by 4D flow MRI based viscous dissipation calculations despite underestimation of the magnitude of viscous dissipation.

ACKNOWLEDGEMENTS

This study is funded by Dutch Technology Foundation STW [Carisma 11629], NIH NHLBI grant R01HL115828; NIH grant K25HL119608 and AHA 14PRE18620016.

REFERENCES

[1] Gewillig M. The Fontan Circulation. Heart. 2005; 91:839-846.

[2] Khairy P, Poirier N, Mercier LA. Univentricular heart. Circulation 2007; 115:800-812.

[3] Whitehad KK, Pekkan K, Kitajima HD, Paridon SM, Yoganathan AP, Fogel MA. Nonlinear Power Loss during Exercise in Single-Ventricle Patients after the Fontan. Circulation 2007; 116:I165-71.

[4] Khiabani RH, Whitehead KK, Han D, Restrepo M, Tang E, Bethel J, Paridon SM, Fogel MA, Yoganathan AP. Exercise capacity in single-ventricle patients after Fontan correlates with haemodynamic energy loss in TCPC. Heart. 2014 Sep 2. pii: heartjnl-2014-306337.

[5] Haggerty CM, Restrepo M, Tang E, de Zélicourt DA, Sundareswaran KS, Mirabella L, Bethel J, Whitehead KK, Fogel MA, Yoganathan AP. Fontan hemodynamics from 100 patient-specific cardiac magnetic resonance studies: a computational fluid dynamics analysis. J Thorac Cardiovasc Surg. 2014 Oct;148(4):1481-9

[6] Bossers SS, Cibis M, Gijsen FJ, Schokking M, Strengers JL, Verhaart RF, Moelker A, Wentzel JJ, Helbing WA. Computational fluid dynamics in Fontan patients to evaluate power loss during simulated exercise. Heart. 2014 May; 100(9):696-701.

[7] Itatani K, Miyaji K, Nakahata Y, Ohara K, Takamoto S, Ishii M. The lower limit of the pulmonary artery index for the extracardiac Fontan circulation. J Thorac Cardiovasc Surg 2011; 142:127-135.

[8] Baretta A, Corsini C, Yang W, Vignon-Clementel IE, Marsden AL, Feinstein JA, Hsia TY, Dubini G, Migliavacca F, Pennati G. Virtual surgeries in patients with congenital heart disease: a multi-scale modelling test case. Philos Transact A Math Phys Eng Sci 2011;369:4316-4330.

[9] Bove EL, de Leval MR, Migliavacca F, Balossino R, Dubini G. Toward optimal hemodynamics: computer modeling of the Fontan circuit. Pediatr Cardiol 2007; 28:477-481.

[10] de Leval MR, Dubini G, Migliavacca F, Jalali H, Camporini G, Redington A, Pietrabissa R. Use of computational fluid dynamics in the design of surgical procedures: application to the study of competitive flows in cavo-pulmonary connections. J Thorac Cardiovasc Surg 1996;111:502-513.

[11] Dubini G, Leval, MR, Pietrabissa, R, Montevecchi, FM., Fumero, R. A numerical fluid mechanical study of repaired congenital heart defects application to the TCPC. Journal of Biomechanics 1996; 29:111-121.

[12] Itatani K, Miyaji K, Tomoyasu T, Nakahata Y, Ohara K, Takamoto S, Ishii M. Optimal conduit size of the extracardiac Fontan operation based on energy loss and flow stagnation. Ann Thorac Surg 2009; 88:565-572; discussion 572-563.

[13] Sundareswaran KS, Haggerty CM, de Zelicourt D, Dasi LP, Pekkan K, Frakes DH, Powell AJ, Kanter KR, Fogel MA, Yoganathan AP.Visualization of flow structures in Fontan patients using three-dimensional phase contrast magnetic resonance imaging. J Thorac Cardiovasc Surg. 2012 May; 143(5):1108-16.

[14] Barker AJ, van Ooij P, Bandi K, Garcia J, Albagdadi M, McCarthy P, Bonow RO, Carr J, Collins J, Malaisrie SC, Markl M. Viscous energy loss in the presence of abnormal aortic flow. Magn Reson Med. 2014 Sep;72(3):620-8

[15] Venkatchari AK, Halliburton SS, Setser RM, White RD, Chatzimavroudis GP. Noninvasive quantification of fluid mechanical energy losses in the total cavopulmonary connection with magnetic resonance phase velocity mapping. Magn Reson Imaging. 2007 Jan; 25(1):101-9.

[16] Markl M, Geiger J, Kilner PJ, Föll D, Stiller B, Beyersdorf F, Arnold R, Frydrychowicz A. Time-resolved three-dimensional magnetic resonance velocity mapping of cardiovascular flow paths in volunteers and patients with Fontan circulation. Eur J Cardiothorac Surg. 2011 Feb; 39(2):206

[17] Sundareswaran KS, Pekkan K, Dasi LP, Whitehead K, Sharma S, Kanter KR, Fogel MA, Yoganathan AP. The total cavopulmonary connection resistance: a significant impact on single ventricle hemodynamics at rest and exercise. Am J Physiol Heart Circ Physiol. 2008 Dec; 295(6):H2427-35.

[18] Bird RB, Stewart WE, Lightfoot EN. Transport Phenomena. NewYork: John Wiley and Sons, Inc.; 1960.

[19] Bernstein MA, Zhou XJ, Polzin JA, King KF, Ganin A, Pelc NJ, Glover GH. Concomitant Gradient Terms in Phase Contrast Mr: Analysis and Correction. Magnetic Resonance in Medicine. 1998;39:300-308

[20] Bock J, Kreher W, Hennig J, Markl M. Optimized Pre-Processing of Time-Resolved 2d and 3d Phase Contrast Mri Data. Proc. Intl. Soc. Mag. Reson. Med. 2007;15:3138

[21] Walker PG, Cranney GB, Scheidegger MB, Waseleski G, Pohost GM, Yoganathan AP. Semiautomated Method for Noise Reduction and Background Phase Error Correction in Mr Phase Velocity Data. J Magn Reson Imaging. 1993;3:521-530

[22] Yushkvich PA, Piven J, Hazlett HC, Smith RG, Ho S, Gee JC, Gerig G. User-guided 3D active contour segmentation of anatomical structures: significantly improved efficiency and reliability. Neuroimage 2006; 31(3): 1116–1128.

[23] Seo T, Schachter LG, Barakat AI. Computational Study of Fluid Mechanical Disturbance Induced by Endovascular Stents. Annals of Biomedical Engineering. 2005, 33(4), 444–456.

[24] Casas B, Lantz J, Dyverfeldt P, Ebbers T. 4D flow MRI-Based pressure loss estimation in stenotic flows: Evaluation using numerical simulations. Magn Reson Med. 2015 May 28.

[25] Morbiducci U, Ponzini R, Rizzo G, Biancolini ME, Iannaccone F, Gallo D, Redaelli A. Synthetic dataset generation for the analysis and the evaluation of image-based hemodynamics of the human aorta. Med Biol Eng Comput. 2012 Feb; 50(2):145-54.

[26] Cibis M, Potters WV, Gijsen FJ, Marquering H, vanBavel E, van der Steen AF, Nederveen AJ, Wentzel JJ. Wall shear stress calculations based on 3D cine phase contrast MRI and computational fluid dynamics: a comparison study in healthy carotid arteries. NMR Biomed. 2014 Jul; 27(7):826-34.

[27] Marsden AL, Vignon-Clementel IE, Chan FP, Feinstein JA, Taylor CA. Effects of exercise and respiration on hemodynamic efficiency in CFD simulations of the total cavopulmonary connection. Ann Biomed Eng 2007; 35:250–63.

Chapter 7

Computational fluid dynamics in Fontan patients to evaluate power loss during simulated exercise

Based on:

Bossers SS, Cibis M, Gijsen FJ, Schokking M, Strengers JL, Verhaart RF, Moelker A, Wentzel JJ, Helbing WA. Computational fluid dynamics in Fontan patients to evaluate power loss during simulated exercise. Heart. 2014 May;100(9):696-701.

ABSTRACT

Introduction

Exercise intolerance is common in total cavopulmonary connection (TCPC)-patients. It has been suggested that power loss (Ploss) inside the TCPC plays a role in reduced exercise performance. Our objective is to establish the role of Ploss inside the TCPC during increased flow, simulating exercise in a patient-specific way.

Methods

Cardiac magnetic resonance imaging (CMR) was used to obtain flow rates from the caval veins during rest and increased flow, simulating exercise with dobutamine. A 3-dimensional reconstruction of the TCPC was created using CMR data. CFD-simulations were performed to calculate Ploss inside the TCPC-structure for rest and stress conditions. To reflect the flow distribution during exercise, a condition where inferior caval vein (IVC) flow was increased twofold compared to rest, was added. 29 TCPC-patients (15 intra-atrial lateral tunnel (ILT) and 14 extracardiac conduit (ECC)) were included.

Results

Mean Ploss at rest was 1.36±0.94 (ILT) and 3.20±1.26 (ECC) mW/m^2 ($p<0.001$), 2.84±1.95 (ILT) and 8.41±3.77 (ECC) mW/m^2 ($p<0.001$) during dobutamine and 5.21±3.50 (ILT) and 15.28±8.30 (ECC) mW/m^2 ($p=0.001$) with twofold IVC flow. The correlation between cardiac index and Ploss was exponential (ILT: $R^2=0.811$, $p<0.001$, ECC: $R^2=0.690$, $p<0.001$)).

Conclusions

Ploss inside the TCPC-structure is limited, but increases with simulated exercise. This relates to the anatomy of TCPC and the surgical technique used. In all flow conditions, ILT patients have lower Ploss than ECC patients. We did not find a relationship between Ploss and exercise capacity.

INTRODUCTION

In most patients with univentricular heart disease, treatment consists of creating a total cavopulmonary connection (TCPC) known as Fontan procedure. In this series of operations the superior caval vein (SVC) and the inferior caval vein (IVC) are connected to the pulmonary arteries[1]. The TCPC is usually performed using the intra-atrial lateral tunnel (ILT) or extracardiac conduit (ECC) technique.

Important reduction of mortality and morbidity of the Fontan operation have been obtained over the last 30 years. Despite improvements, deterioration of functional capacity and limited exercise tolerance remain well-known long-term problems after Fontan completion[2,3]. While the mechanisms of exercise intolerance are not completely understood, it has been suggested that it may be related to power loss (Ploss) inside the TCPC-baffle. Previous studies demonstrated that the anatomy of TCPC significantly affects Ploss[4,5]. Furthermore, Ploss increases nonlinearly during exercise[4]. Several studies have used computational fluid dynamics (CFD) to explore Ploss change with exercise. In these studies, flow conditions were measured at rest using cardiac magnetic resonance imaging (CMR) and exercise was simulated in CFD by increasing the flows with a constant multiplier, not necessarily reflecting the patient-specific conditions[4]. Other studies measured flows during exercise, but used generalized TCPC-geometries, not considering the individual geometric variations between patients[5].

We aimed to study the extent of Ploss inside the TCPC-baffle, using patient-specific TCPC-anatomy and flow at rest and during patient-specific flow increase with dobutamine, simulating exercise conditions. We also aimed to assess the relationship between Ploss and the exercise capacity of Fontan patients, comparing results of the ILT and ECC techniques.

METHODS

Patients

The patients participated in an ongoing cross-sectional multicenter study in the Netherlands. The surgical technique used depended on the preference of the operating surgeon. In the Netherlands, referral patterns for congenital heart disease mainly follow a geographical pattern. Therefore, both the ILT and the ECC groups may be considered 'random samples' of Fontan-patients.

Inclusion criteria were: TCPC, staged approach according to a current technique (i.e. ILT and ECC); completion of the TCPC before the age of 6 years; inclusion in the study at an age of at least 8 years; at least 4 years since completion of the TCPC. Patients with severe mental retardation and with significant shunting were excluded. Informed consent was obtained from all patients and/or their parents. The study was approved by the institutional review boards of the participating centres. For the current analysis we selected the first consecutive 15 ILT and 14 ECC patients from a total of 70 patients that successfully underwent the complete CMR-protocol.

CMR

All MRI scans were performed on 1.5 Tesla whole-body MRI systems (General Electric Signa 1.5T, Philips Achieva 1.5T and Siemens Avanto 1.5T). To obtain anatomical data, axial stacks of steady-state free-precession were made. In-plane resolution was between 1.1 and 1.6mm, depending on patient size. Slice thickness was 6mm, and the gap between consecutive slices was -3mm, resulting in a virtual slice thickness of 3mm.

Flow rates for SVC, IVC and left pulmonary artery (LPA) were measured by through-plane phase-contrast MRI with at least 24 phases per cardiac cycle during free-breathing, with signal averages of 3. Views per segment was 5- 6, repetition time was 1.99- 5.62 ms and phase-FOV was 0.7- 0.8, as a result temporal resolution was 16- 45 ms. A standard velocity encoding of 60 cm/s was used, which was increased with small steps in case of aliasing. Flow was measured at rest and during increased flow simulating exercise by administering dobutamine-hydrochloride (Centrafarm Services, Etten-Leur, the Netherlands) intravenously at a rate of 7.5 μg/kg/min[6]. After dobutamine administration, when a new steady-state in heart-rate was reached, flow measurements were repeated, using the same parameters as in the rest conditions. Dobutamine is a synthetic catecholamine with a positive inotropic and, to lesser extent, chronotropic effect. Dobutamine increases oxygen demand in myocardial tissue. This increases cardiac output, thereby increasing flow in a similar fashion in all vessels[7]. Flow data was analysed on an Advanced Workstation (General Electric Medical Systems). The images were quantitatively analysed with the Flow Analysis software (Medis Medical Imaging Systems). To adjust for phase-offset errors, flow measurements were corrected using a solid gel phantom[8].

Segmentation and meshing

The TCPC geometry was extracted from the axial stacks of an MRI dataset by delineating the lumen contours manually using ITK-SNAP. The segmentations were performed by one researcher (MC) to avoid inter-observer variations. We cut the segmentations before the main splitting branches in IVC, SVC and in right pulmonary artery (RPA). The LPA was cut at the same length as the RPA.

The segmented geometry was uniformly smoothed with a pass band of 0.1 in 30 iterations using VMTK. We added flow extensions with a length of one mean profile radius to the IVC and SVC inlets, and four mean profile radii to the LPA outlets. After carrying out a mesh independency study, the geometries were meshed with uniform tetrahedral elements of 0.75mm using GAMBIT (ANSYS).

CFD

The CFD simulations were performed on a standard desktop computer (Intel Xeon six core processor, 2.40GHz CPU and 12GB RAM) using the commercial finite element software FIDAP 8.7.4 (Ansys).

We calculated the time-averaged IVC, SVC and LPA flow rates. The blood flow rates measured at IVC, SVC and LPA were prescribed with a parabolic velocity profile. The RPA outlet was set as stress-free. The walls were assumed as rigid and no-slip condition was prescribed. The blood flow was assumed to be laminar. The density of the blood was set to $1060 kg/m^3$. Carreau model was used to account for the non-Newtonian blood properties. For the simulations, we chose pressure-based segregated algorithm, backward Euler method for time integration and upwinding stabilization scheme. The convergence criterion was set to 0.1%.

Simulations were performed at three flow conditions: 1) resting condition using the individual flows measured during rest 2) stress condition using the flows measured during increased flow, simulating exercise, with dobutamine 3) a condition where only IVC flow was twofold higher than at resting condition. We will refer to this condition as IVCincrease. IVCincrease was necessary because dobutamine increases blood flow equally between the upper and lower half of the body. However, during supine exercise on a bicycle ergometer, this increase is mainly in the lower half of the body[9]. Some studies have shown this effect by using a supine bicycle ergometer during MRI flow measurements[9,10]. IVCincrease condition was based on results reported by Hjortdal et al[9] where caval blood flow was measured by MRI in Fontan patients during supine exercise on a MRI-compatible ergometer. In their study, the exercise at a load of 1.0Watt/kg caused a twofold flow increase in the IVC, while SVC-flow remained constant[9]. For the IVCincrease condition, flow split of the pulmonary arteries was kept as in the resting condition.

Reynolds numbers were calculated for each simulation using the following equation:

$$Re = \frac{\rho U D}{\mu}$$

ρ : blood density, U: mean velocity, D: hydraulic diameter μ: dynamic equation:

Power loss

Power loss was calculated using the control volume approach as described by Liu et al[11]:

$$\text{Ploss} = \int_{CS} \left[P + \frac{1}{2}\rho u_j u_j \right] u_i n_i dS$$

CS: control surface, p: static pressure, ρ: density, u_i: the components of velocity vector in each element. n_i: the components of the surface normal vector and dS: the area of the differential control surface.

Resistance index (RI) was also calculated by using the following equations[12]:

$$\Delta P = \frac{Ploss}{\mathrm{CO}}$$

$$RI = \frac{\Delta P}{CI}$$

ΔP: Ploss based pressure drop, CO: cardiac output, CI: cardiac index

Bicycle ergometry

To assess exercise capacity, all patients performed bicycle ergometry according to a generalized study-protocol within the framework of the aforementioned study[3]. From this maximum oxygen uptake (VO_2peak) and ventilation/carbon-dioxide slope (VE/VCO_2-slope) were determined.

Statistical Analysis

Statistical analysis was performed using SPSS 21.0. Data was tested for normal distribution and expressed as mean ±standard deviation or median (interquartile range) as appropriate. Results were corrected for body surface area (BSA). Comparisons between ILT and ECC groups were made using independent T-test or Mann-Whitney U test as appropriate. To compare flow measurements between rest and dobutamine paired samples T-test was used. Repeated measures ANOVA with Bonferroni adjustment was used to compare variables during the 3 different simulated conditions. The correlation between Ploss and CI was determined using 'curve estimation'. P-values ≤ 0.05 were considered statistically significant.

RESULTS

There were no significant differences between the ILT and ECC group in terms of baseline parameters, age at study, age at partial cavopulmonary connection, age at Fontan completion and BSA (Table 1).

Fontan circuit dimensions

Mean area of the SVC was comparable for both groups; 1.48±0.43cm^2/m^2 for ILT and 1.27±0.29cm^2/m^2 for ECC patients (p=0.130). The IVC area was larger in ILT patients; 5.64±1.82cm^2/m^2 (ILT) vs. 2.13±0.43cm^2/m^2 (ECC) (p<0.001). ILT patients had also larger pulmonary arteries than ECC patients (LPA: 1.42±0.43cm^2/m^2 vs. 1.01±0.45cm^2/m^2 p=0.018, RPA: 1.82±0.50cm^2/m^2 vs. 1.15±0.36cm^2/m^2, p<0.001).

MRI flow measurements

At rest, there was no significant difference between ILT and ECC flow rates (35±8 vs. 32±6 mL/s/m^2 at IVC and 18±6 vs. 18±5 mL/s/m^2 at SVC) and between cardiac index (CI) of the ILT and ECC group (3.2±0.7 vs. 3.0±0.5 L/min/m^2). Dobutamine-infusion increased flow

Table 1. patient characteristics per group.

		ILT (n=15)	ECC (n=14)
Gender		12M/3F	6M/8F
Age at study (years)		12.9 (±3.0)	12.3 (±2.2)
Age at partial cavopulmonary connection (PCPC) (years)		1.3 (±0.9)	1.2 (±1.1)
Age at total cavopulmonary connection (TCPC) (years)		2.9 (±1.0)	3.3 (±1.0)
Body surface area (m^2)		1.34 (±0.28)	1.33 (±0.24)
Heart defect (n)	Double outlet right ventricle type	4	2
	Double inlet left ventricle type	4	2
	Hypoplastic left heart syndrome	2	2
	Pulmonary atresia	2	0
	Tricuspid atresia	1	7
	Other	2	1
Dominant ventricle (n)	Left	8	9
	Right	7	5
Initial surgery (n)	Pulmonary artery banding	6	8
	Blalock-Taussig-shunt	5	2
	Norwood I	2	2
	Damus-Kaye-Stansell	1	1

Values are presented as mean ±standard deviation or number of patients.

and cardiac index in both ILT and ECC patient groups ($p<0.001$). In the ILT group, IVC flow increased to 43±8 mL/s/m^2, SVC flow to 23±10 mL/s/m^2 and CI to 4.0±0.9 L/min/m^2. In the ECC group, IVC flow increased to 43±8 mL/s/m^2, SVC flow to 25±6 mL/s/m^2 and CI to 4.0±0.6 L/min/m^2. There were no significant differences in flow rates and CI between both groups during dobutamine. Mean Reynolds number at IVC inlet was 636±195 at rest, 821±264 under dobutamine and 1273±390 at IVCincrease flow condition and at SVC inlet was 537±111 at rest and 701±191 under dobutamine.

Power loss

Overall in the 29 patients, Ploss increased from 2.25±1.43mW/m^2 during rest to 5.53±4.07mW/m^2 after dobutamine-infusion ($p<0.001$ vs rest). Ploss increased further to 10.08±8.02mW/m^2 at IVCincrease condition ($p<0.001$ vs. rest, $p=0.001$ vs. dobutamine) (figure 1). For both groups, there was a strong exponential correlation between CI and Ploss (figure 2).

For all conditions there was a linear correlation between Ploss and IVC area (R^2 =0.32-0.34, $p=0.001$) and Ploss and RPA area (R^2 =0.20-0.27, $p<0.015$). LPA area showed a significant correlation with Ploss during IVCincrease only (R^2 =0.15, $p=0.036$). SVC area did not correlate with Ploss.

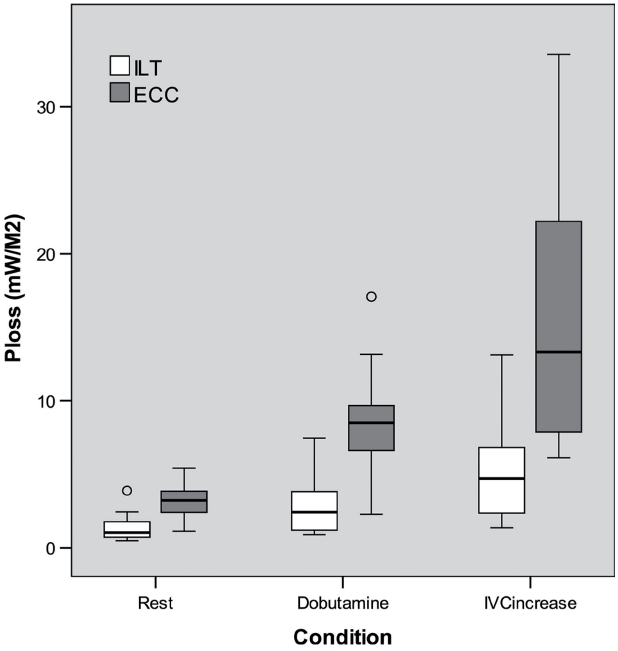

Figure 1. Ploss normalized for BSA per condition per patient group

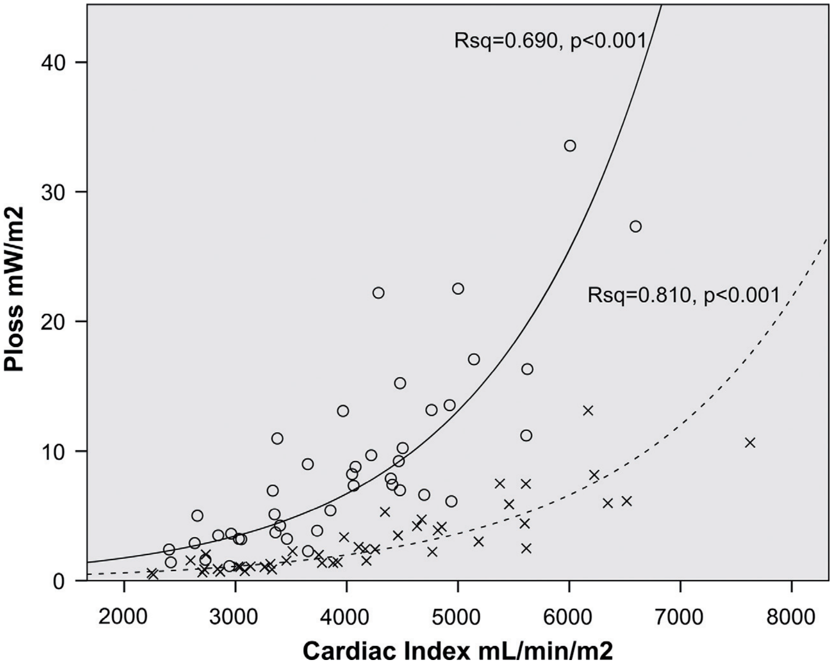

Figure 2. Normalized Ploss vs Cardiac Index for all patients during all conditions (crosses/dotted line = ILT, circles/solid line = ECC) (exponential correlation, ILT: R^2=0.811, p<0.001, ECC: R^2=0.690, p<0.001).

Power loss ILT versus ECC

A summary of Ploss for ILT and ECC patients is presented in table 2. In all flow conditions Ploss was significantly higher for ECC patients than for ILT patients. Ploss was significantly higher after dobutamine than at rest (ILT: $p=0.001$, ECC: $p<0.001$) for all patients and further increased with IVCincrease flow condition (ILT: $p<0.001$vs. rest, $p=0.020$ vs. dobutamine, ECC: $p<0.001$ vs. rest, $p=0.013$ vs. dobutamine). The percentage of Ploss-increase relative to rest was comparable between both patient groups under dobutamine and also for IVCincrease. Resistance index was significantly higher for all conditions in the ECC group.

Exercise capacity vs. power loss

Of the 29 patients, 18 had a maximal exercise test (peak respiratory exchange rate≥1.00). VO_2peak was determined only for these 18 patients and was 78 (71- 86)% of the predicted value. VE/VCO2-slope, a submaximal, effort-independent parameter, was determined in all 29 patients. Median VE/VCO_2-slope was 125 (114- 171)% of the predicted value.

Exercise capacity as assessed by VO_2peak did not correlate with Ploss in any flow condition. Furthermore, submaximal parameter VE/VCO_2-slope did not correlate with Ploss. There was no correlation between resistance index and exercise capacity.

DISCUSSION

Patients that underwent the Fontan procedure are among those with congenital heart disease that have the highest risk for poor clinical state and functional deterioration[1]. Power loss as a result of the complex flow pattern in the Fontan baffle has been suggested to contribute to impaired clinical state, along with factors such as increased afterload, decreased preload and abnormal ventricular-arterial coupling[13]. The role of Ploss in the Fontan pathway has been subject to debate. Factors contributing to power

Table 2. Results of the power loss calculations, per group.

	Condition	ILT (n=15)	ECC (n=14)	p-value
Ploss(mW/m^2)	Rest	1.36 ±0.94	3.20 ±1.26	<0.001 *
	Dobutamine	2.84 ±1.95	8.41 ±3.77	<0.001 *
	IVC increase	5.21 ±3.50	15.28 ±8.30	0.001 *
Increase in Ploss compared to rest (%)	Dobutamine	104(48-142)	143(113-192)	0.070 $
	IVC increase	285 ±136	385 ±155	0.079 *
Resistance Index (mmHg/[L/min/m^2])	Rest	0.055 ±0.020	0.159 ±0.061	<0.001 *
	Dobutamine	0.072 ±0.024	0.229 ±0.088	<0.001 *
	IVC increase	0.076 ±0.035	0.279 ±0.122	<0.001 *

Values are presented as mean ±standard deviation, or median (interquartile range). P-values display significance between ILT-patients and ECC-patients. *: Independent samples T-test, $: Mann-Whitney U-test.

loss include geometric properties and flow splits[4,5]. In this study, we created patient-specific models which reflect the variations in TCPC-geometries and flow patterns. To the best of our knowledge, this is the first study that combines patient-specific geometries as well as patient-specific dobutamine-enhanced simulated exercise conditions in patients with a Fontan circulation. Our results confirm a strong, non-linear correlation between Ploss and cardiac index during increased flow, simulating exercise and show a distinct difference between ILT and ECC patients. We observed a large spread in Ploss at the same level of cardiac index, which supports the theory that differences in Ploss relate to patient-specific geometry.

Between the ILT and ECC patient groups with comparable baseline characteristics, there were clear differences in Ploss at different flow conditions. At comparable flow volumes, the mean velocity at IVC was lower for ILT patients than the ECC patients. This was because blood flows through larger IVC surface areas in the ILT patients. Power loss is proportional to the square of the velocity (as shown in the equation for Ploss), resulting in lower Ploss in ILT patients. Additionally, the smaller pulmonary artery size in the ECC patients led to higher pressure drops and thus higher Plosses for this group[14].

The significant difference in pulmonary artery size between both groups is an interesting finding. Considering the cardiac diagnoses it could be advocated that ECC patients were at increased risk of compromised pulmonary blood flow before the partial and total cavopulmonary connection. However, there was no difference in the proportion of procedures to increase pulmonary blood flow between both groups. Another option is that the relatively small amount of patients has caused a sampling artifact. Furthermore the loss of pulsatility in the ECC might have resulted in less growth of the pulmonary arteries compared to those in the ILT-patients[15].

We could not establish a relationship between exercise capacity and Ploss or resistance index. Whitehead et al. found a non-significant negative trend between resistance index inside the TCPC and VO_2peak[4]. In our study, with larger sample size, we could not reproduce this finding. This indicates that other factors influence exercise capacity more than power loss inside the TCPC.

In comparison to other studies, we found a low Ploss inside the TCPC, especially for the ILT group. Several factors explain the wide range of Ploss in different studies including Fontan baffle geometry, the level of (simulated) exercise, respiratory effects and boundary conditions for CFD. Table 3 provides a comparison between our study and other studies in this field.

Whitehead et al and Marsden et al used patient specific Fontan-geometries for CFD simulations. In these studies, Ploss at rest was up to 5–10 times higher than our study, at similar cardiac index. An important difference between our study and the study form Marsden et al. and others, was that they included side branches of the pulmonary arteries[16,17]. Another difference between our study and that by Whitehead et al is that they assumed flow increased up to 300% during exercise[4].

The variation in reported Ploss may also be related to the differences in the flow cross-sectional areas. In some studies flow rates for IVC and SVC were similar to ours, but the diameters of these vessels were smaller than in our study, resulting in higher power losses, as described earlier[11,18,19].

In a more recent study, Baretta et al. found power losses close to our findings. They simulated the total circulation of one patient, using combined anatomical and flow data from echocardiography, catheterization and CMR. In their study, the efficiency of several TCPC variants was investigated by performing virtual surgery in a pre-TCPC Fontan patient[17].

The role of Ploss in the TCPC in the total circulation

It has been suggested that cardiac output in Fontan patients is more dependent on preload then on contractility, which is generally well preserved[13,20]. Preload in the Fontan circulation is directly dependent on transpulmonary blood flow. Considering the generally higher pulmonary and systemic vascular resistance in Fontan patients compared to healthy controls, Ploss inside the TCPC may be clinically relevant.

Total circulatory power has been found to be lower in Fontan patients (0.71±0.25W/ m^2) than in controls (1.06±0.21W/ m^2)[21,22]. Compared to these values, power loss levels reported for the TCPC baffle have been considered to be nearly negligible. However it has been shown that the percentage of the power lost inside the TCPC can be as high as 30-40% of input power for some patients under exercise conditions, which can be considered to be significant[23].

Sundareswan et al showed a weak correlation (R=0.36) between cardiac output and TCPC-resistance. They calculated that a 10% increase of TCPC-resistance would reduce cardiac output with 8.6%[12]. Ploss is directly dependent on TCPC-resistance and the total flow, supporting the theory that Ploss inside the TCPC might have an effect on the circulation in Fontan patients. This could not be confirmed for clinical outcome parameters, such as measures of exercise capacity, in our study.

Recommendations for future research

A common limitation of CFD models of the Fontan circulation is that pulmonary and systemic circulation are not taken into account. In reality, the pulmonary arterial branches and the pulmonary vascular bed are connected to the TCPC-baffle. Clearly, pulmonary vascular resistance contributes to Ploss and preferably should be included in calculations in the Fontan circulation. Nevertheless, pressure drop due to geometric features and the flow rates of IVC, SVC and pulmonary arteries are the main determinants of Ploss in Fontan baffle.

Table 3. Comparison of CFD-studies in Fontan-patients. R_p; pulmonary vascular resistance; PA, pulmonary artery; IVC, inferior caval vein; SVC, superior caval vein

author	year of publication	N	patient specific model	exercise simulated	R_p in model	Respiration Effects	PA sidebranches	Cardiac Index (L/min/m^2)	diameter IVC/SVC (mm)	diameter PA (mm)	Ploss rest (mW)	Ploss exercise (mW)
This study; ILT		15	+	+	-	-	-	3.2 - 5.3	22-42 / 12-22	11-23	0.59 - 4.40	1.71 - 23.1
This study; ECC		14	+	+	-	-	-	3.0 - 4.9	15-21 / 12-17	9-19	1.63 - 7.67	7.03 – 48.2
Baretta[17]	2011	1	+	+	+	+	+	2.6	20.0 / 11.8		1.09 - 4.8	3.3 - 4.8
Marsden [16]	2006	2	+	+	+	+	+	2.86 - 4.52			6.7 - 13.9	19.5 - 169.4
Whitehead [4]	2007	10	+	+	+	-	-	2.37 - 5.20			~5-30	~120 - 1200
de Leval [26]	1996	5	+	-				~3.00	22.0-25.0 / 15.0	15.0	5.0 – 8	
Itatani [5]	2009	17	-	+	+	+	-	2.86 - 4.52	13.8 / 10.5	9.6	1.5	2.7 - 5.8
Bove [27]	2007	1	-	-	+	-	-	2.23			4 - 56.6	
Ryu [19]	2001	3	-	-		-	-	4.00	13.0-15.0 / 8.0-13.0	13.0	10.0	
Liu [11]	2004	1	-	-				1.00 - 6.00	15.0 / 8.0	13.3	12.0 - 14	
Dubini [28]	1996	9	-	-			-	3.00	15.0 / 12.0	10.0	1.5	

Values are presented as range or mean (in case of single/fixed value)

Respiration plays a key role in the Fontan circulation[24]. An opportunity for improvement is the incorporation of respiration into CFD models. Although pulmonary artery pulsatility is decreased in Fontan patients they may still have pulsatile function, especially in ILT patients[15]. In the CFD simulations, we assumed that the vessel walls were rigid. Considering the limited pulsatility in the Fontan circulation, the common assumptions of rigid walls and steady flow are valid. Furthermore, Long et al. showed in two patients that the time averaged power efficiencies calculated with rigid walls were only 1.5% lower than that calculated with compliant walls[25].

CONCLUSION

Ploss inside the TCPC-structure is limited but increases with (simulated) exercise. This relates to patient-specific TCPC anatomy and the surgical technique used. In all flow conditions, ILT patients have lower Ploss than ECC patients. We did not find a relationship between Ploss and exercise capacity.

ACKNOWLEDGEMENTS

For Julia and other children who died from a univentricular heart defect.

REFERENCES

[1] Khairy P, Poirier N, Mercier LA. Univentricular heart. Circulation 2007;115:800-812.

[2] Anderson PA, Sleeper LA, Mahony L, Colan SD, Atz AM, Breitbart RE, Gersony WM, Gallagher D, Geva T, Margossian R, McCrindle BW, Paridon S, Schwartz M, Stylianou M, Williams RV, Clark BJ, 3rd. Contemporary outcomes after the Fontan procedure: a Pediatric Heart Network multicenter study. J Am Coll Cardiol 2008;52:85-98.

[3] Robbers-Visser D, Kapusta L, van Osch-Gevers L, Strengers JL, Boersma E, de Rijke YB, Boomsma F, Bogers AJ, Helbing WA. Clinical outcome 5 to 18 years after the Fontan operation performed on children younger than 5 years. J Thorac Cardiovasc Surg 2009;138:89-95.

[4] Whitehead KK, Pekkan K, Kitajima HD, Paridon SM, Yoganathan AP, Fogel MA. Nonlinear power loss during exercise in single-ventricle patients after the Fontan: insights from computational fluid dynamics. Circulation 2007;116:I165-171.

[5] Itatani K, Miyaji K, Tomoyasu T, Nakahata Y, Ohara K, Takamoto S, Ishii M. Optimal conduit size of the extracardiac Fontan operation based on energy loss and flow stagnation. Ann Thorac Surg 2009;88:565-572; discussion 572-563.

[6] Robbers-Visser D, Boersma E, Helbing WA. Normal biventricular function, volumes, and mass in children aged 8 to 17 years. J Magn Reson Imaging 2009;29:552-559.

[7] Robbers-Visser D, Luijnenburg SE, van den Berg J, Roos-Hesselink JW, Strengers JL, Kapusta L, Moelker A, Helbing WA. Safety and observer variability of cardiac magnetic resonance imaging combined with low-dose dobutamine stress-testing in patients with complex congenital heart disease. Int J Cardiol 2009.

[8] Gatehouse PD, Rolf MP, Graves MJ, Hofman MB, Totman J, Werner B, Quest RA, Liu Y, von Spiczak J, Dieringer M, Firmin DN, van Rossum A, Lombardi M, Schwitter J, Schulz-Menger J, Kilner PJ. Flow measurement by cardiovascular magnetic resonance: a multi-centre multi-vendor study of background phase offset errors that can compromise the accuracy of derived regurgitant or shunt flow measurements. J Cardiovasc Magn Reson 2010;12:5.

[9] Hjortdal VE, Christensen TD, Larsen SH, Emmertsen K, Pedersen EM. Caval blood flow during supine exercise in normal and Fontan patients. Ann Thorac Surg 2008;85:599-603.

[10] Pedersen EM, Stenbog EV, Frund T, Houlind K, Kromann O, Sorensen KE, Emmertsen K, Hjortdal VE. Flow during exercise in the total cavopulmonary connection measured by magnetic resonance velocity mapping. Heart 2002;87:554-558.

[11] Liu Y, Pekkan K, Jones SC, Yoganathan AP. The effects of different mesh generation methods on computational fluid dynamic analysis and power loss assessment in total cavopulmonary connection. J Biomech Eng 2004;126:594-603.

[12] Sundareswaran KS, Pekkan K, Dasi LP, Whitehead K, Sharma S, Kanter KR, Fogel MA, Yoganathan AP. The total cavopulmonary connection resistance: a significant impact on single ventricle hemodynamics at rest and exercise. Am J Physiol Heart Circ Physiol 2008;295:H2427-2435.

[13] Robbers-Visser D, Jan Ten Harkel D, Kapusta L, Strengers JL, Dalinghaus M, Meijboom FJ, Pattynama PM, Bogers AJ, Helbing WA. Usefulness of cardiac magnetic resonance imaging combined with low-dose dobutamine stress to detect an abnormal ventricular stress response in children and young adults after fontan operation at young age. Am J Cardiol 2008;101:1657-1662.

[14] Dasi LP, Krishnankuttyrema R, Kitajima HD, Pekkan K, Sundareswaran KS, Fogel M, Sharma S, Whitehead K, Kanter K, Yoganathan AP. Fontan hemodynamics: importance of pulmonary artery diameter. J Thorac Cardiovasc Surg 2009;137:560-564.

[15] Robbers-Visser D, Helderman F, Strengers JL, van Osch-Gevers L, Kapusta L, Pattynama PM, Bogers AJ, Krams R, Helbing WA. Pulmonary artery size and function after Fontan operation at a young age. J Magn Reson Imaging 2008;28:1101-1107.

[16] Marsden AL, Vignon-Clementel IE, Chan FP, Feinstein JA, Taylor CA. Effects of exercise and respiration on hemodynamic efficiency in CFD simulations of the total cavopulmonary connection. Ann Biomed Eng 2007;35:250-263.

[17] Baretta A, Corsini C, Yang W, Vignon-Clementel IE, Marsden AL, Feinstein JA, Hsia TY, Dubini G, Migliavacca F, Pennati G. Virtual surgeries in patients with congenital heart disease: a multi-scale modelling test case. Philos Transact A Math Phys Eng Sci 2011;369:4316-4330.

[18] Itatani K, Miyaji K, Nakahata Y, Ohara K, Takamoto S, Ishii M. The lower limit of the pulmonary artery index for the extracardiac Fontan circulation. J Thorac Cardiovasc Surg 2011;142:127-135.

[19] Ryu K, Healy TM, Ensley AE, Sharma S, Lucas C, Yoganathan AP. Importance of accurate geometry in the study of the total cavopulmonary connection: computational simulations and in vitro experiments. Ann Biomed Eng 2001;29:844-853.

[20] Gewillig M, Brown SC, Eyskens B, Heying R, Ganame J, Budts W, Gerche AL, Gorenflo M. The Fontan circulation: who controls cardiac output? Interact Cardiovasc Thorac Surg 2010;10:428-433.

[21] Senzaki H, Masutani S, Kobayashi J, Kobayashi T, Sasaki N, Asano H, Kyo S, Yokote Y, Ishizawa A. Ventricular afterload and ventricular work in fontan circulation: comparison with normal two-ventricle circulation and single-ventricle circulation with blalock-taussig shunts. Circulation 2002;105:2885-2892.

[22] Sundareswaran KS, Kanter KR, Kitajima HD, Krishnankutty R, Sabatier JF, Parks WJ, Sharma S, Yoganathan AP, Fogel M. Impaired power output and cardiac index with hypoplastic left heart syndrome: a magnetic resonance imaging study. Ann Thorac Surg 2006;82:1267-1275; discussion 1275-1267.

[23] Marsden AL, Reddy VM, Shadden SC, Chan FP, Taylor CA, Feinstein JA. A new multiparameter approach to computational simulation for Fontan assessment and redesign. Congenit Heart Dis 2010;5:104-117.

[24] Hjortdal VE, Emmertsen K, Stenbog E, Frund T, Schmidt MR, Kromann O, Sorensen K, Pedersen EM. Effects of exercise and respiration on blood flow in total cavopulmonary connection: a real-time magnetic resonance flow study. Circulation 2003;108:1227-1231.

[25] Long CC, Hsu MC, Bazilevs Y, Feinstein JA, Marsden AL. Fluid–structure interaction simulations of the Fontan procedure using variable wall properties. International journal for numerical methods in biomedical engineering 2012;28:513-527.

[26] de Leval MR, Dubini G, Migliavacca F, Jalali H, Camporini G, Redington A, Pietrabissa R. Use of computational fluid dynamics in the design of surgical procedures: application to the study of competitive flows in cavo-pulmonary connections. J Thorac Cardiovasc Surg 1996;111:502-513.

[27] Bove EL, de Leval MR, Migliavacca F, Balossino R, Dubini G. Toward optimal hemodynamics: computer modeling of the Fontan circuit. Pediatr Cardiol 2007;28:477-481.

[28] Dubini G, Leval, M.R., Pietrabissa, R., Montevecchi, F., M., Fumero, R. A numerical fluid mechanical study of repaired congenital heart defects application to the TCPC. Journal of Biomechanics 1996;29:111-121.

Chapter 8

Long term serial follow-up of pulmonary artery size and wall shear stress in Fontan patients.

Based on:

Bossers S, Cibis M, Kapusta L, Potters W, Snoeren MM, Wentzel JJ, Moelker A, Helbing W, Long term serial follow-up of pulmonary artery size and wall shear stress in Fontan patients. Accepted

ABSTRACT

Introduction

Pulmonary arterial (PA) flow is abnormal after the Fontan operation and is marked by a lack of pulsatility. We assessed the effects of this abnormal flow on the size and function of the PA's in Fontan patients in long term serial follow-up.

Methods

23 Fontan patients with serial follow-up were included. Median age was 11.1 (9.5-16.0) years at baseline and 15.5 (12.5-22.7) years at follow-up . Median follow-up duration was 4.4 (4.0-5.8) years. Flow and size of the left pulmonary artery (LPA) was determined using phase contrast MRI. From this wall shear stress (WSS), distensibility and pulsatility were determined. A group of healthy peers was included for reference.

Results

Flow and pulsatility were significantly lower in patients than in controls ($p<0.001$). Mean area was comparable in patients and controls, but distensibility was significantly higher in controls ($p<0.001$).

Mean and peak WSS were significantly lower in Fontan patients ($p<0.001$). Between baseline and follow-up, there was a significant increase in normalized flow (15.1(14.3-19.1) ml/sec/m^2 to 18.7(14.0-22.6) ml/sec/m^2, $p=0.023$). Area, pulsatility, distensibility and WSS did not change, but there was a trend toward a lower mean WSS ($p=0.068$). Multivariable regression analysis showed that flow, area and age were important predictors for WSS.

Conclusions

WSS in Fontan patients is decreased compared to healthy controls and tends to decrease further with age. Pulsatility and distensibility are significantly lower compared to healthy controls. Pulmonary artery size however, is not significantly different from healthy controls and long term growth after Fontan-operation is proportionate to body size.

INTRODUCTION

The Fontan circulation, used as a final palliative approach for univentricular heart defects, is marked by a direct connection of the systemic venous return to the pulmonary arteries (PA)[1]. This leads to passive pulmonary blood flow, that is no longer driven by a subpulmonary ventricle. As a result, these children have an abnormal flow pattern in their PAs early on in life, characterized by a nearly complete loss of pulsatility[2,3].

It is hypothesized that this abnormal flow and pulsatility could influence PA growth and function on the long-term. Since the Fontan circulation is dependent on a low transpulmonary pressure gradient, it is important to monitor the development of these vessels. However, the longitudinal data on PA size and function in Fontan circulation scarce is scarce and studies investigating PA size in Fontan patients have also shown conflicting results[3-5].

Wall shear stress (WSS) is important in the development of vasculature. Reduced levels of WSS have been related to PA endothelial dysfunction. There is an inverse relation between vessel diameter and WSS[6]. A previous study from our centre has shown that WSS is reduced in Fontan patients during rest, and also during exercise relative to healthy subject[3]. One can therefore expect that the reduced level of WSS might influence the growth and function of pulmonary arteries.

To date, only few studies have investigated PA growth using MRI long term after the Fontan operation. No studies have measured the course of WSS over time in Fontan patients. The objective of this study was to assess PA growth, function and WSS over time in Fontan patients using MRI.

METHODS

Patients

All patients participated in an ongoing cross-sectional multicenter study in the Netherlands. Patients who underwent Fontan operation at young age, either according to an atriopulmonary connection or a total cavopulmonary connection (TCPC) were included. Patients with mental retardation and contraindications for cardiac magnetic resonance imaging (CMR) were excluded. Informed consent was obtained from all patients and/or their parents. The study was approved by the institutional review boards of the participating centres. The study was conducted in accordance with the Helsinki Declaration. Medical records were reviewed for anatomical and operative details.

MRI imaging

In an earlier study, it was shown that accurate flow measurement in the RPA was not feasible in every patient because of the short distance between the connection of the superior caval vein and the first branching point of the RPA. Comparison of LPA and

RPA flow in the aforementioned study did not show any significant differences in flow parameters between both PA's[3]. Therefore we analyzed left pulmonary artery (LPA) only.

All MRI scans were performed on a 1.5T whole-body MRI system in the participating centres (General Electric Signa, Philips Achieva and Siemens Avanto). The LPA was localized on a transverse steady state free precession (SSFP) image set. On this transverse image, another localizer was planned longitudinally along the LPA. Using both these imaging planes, a flow measurement plane was planned perpendicular to the flow direction. Specific care was taken to match the imaging planes between both visits. In-plane resolution was between 1.1 and 1.6 mm, depending on patient size. Slice thickness was 6 mm. Phase contrast measurements were obtained using unidirectional velocity encoding (VENC) of 60 cm/s. In case of aliasing, this VENC was stepwise increased with increments of 20 cm/s until aliasing disappeared. Flow was measured over 24 phases per cardiac cycle. To incorporate the effect of breathing, which is essential in the pulmonary circulation of Fontan patients, phase-contrast flow measurements were made without breath-holds and with 3 signal averages.

LPA contours were drawn on all phases using Flow Analysis software (Medis Medical Imaging Systems) to determine mean, maximal and minimal areas and mean, maximal and minimal flows. Distensibility, which is the maximum change in cross-sectional area during the cardiac cycle, and pulsatility, which is the flow change during the cardiac cycle, were calculated according to the following formulas:

$$distensibility = \frac{(maximal\ area\text{-}minimal\ area)}{maximal\ area}$$

$$pulsatility = \frac{(maximal\ flow\text{-}minimal\ flow)}{mean\ flow}$$

WSS calculation

Wall shear stress was calculated according to van Duivenvoorden et al[7]. In short, blood flow velocities were calculated within the LPA contours using the phase contrast MR images. Velocities within a distance ≥0.5 pixels to the outer lumen border were excluded since those pixels were partially located outside of the lumen. The cross-section was divided into four segments with 10 degrees of overlap. In each segment, the velocities were projected onto one plane. Assuming blood velocity to be zero at the lumen wall, the projected velocities within 3 pixel distance inwards were fit with a second order curve and wall shear rate (WSR) per segment was calculated for each time point. WSS was calculated by multiplying WSR with the blood viscosity (3.2 P). We averaged the WSS values of 4 segments to obtain mean cross-sectional WSS. The analysis was performed on cardiac cycle averaged WSS only[7].

Healthy controls

In healthy controls RPA was chosen for the flow and WSS analysis since the first branching point of LPA was closer to the bifurcation than the branching point of RPA leading to disturbed flow signals in the LPA images. Images in these controls were acquired as part of another study protocol, and were only acquired at one point in time. In this study, VENC was 150 cm/s and images were taken during breath-hold at expiration[3].

Statistical analysis

Statistical analysis was performed using SPSS 21.0. Data was tested for normal distribution and expressed as mean ± standard deviation or median (interquartile range) as appropriate. Results were corrected for body surface area (BSA). Comparisons between Fontan patients and healthy controls were made using independent T-test or Mann-Whitney U test as appropriate. To compare measurements between baseline and follow-up, paired samples T-test or Wilcoxon singed-rank test were used. P-values ≤ 0.05 were considered statistically significant. In order to identify predictors for WSS, linear regression analysis was performed. A p-value ≤ 0.05 was required for a variable to be retained in the final model.

RESULTS

28 patients underwent two MRI studies each with flow measurements of the LPA. In 4 patients, scanning planes did not properly match between both visits. These patients were therefore excluded. Another patient underwent a conversion from APC to extracardiac conduit (ECC) TCPC with concomitant PA-surgery between both visits and was therefore excluded. There were no interventions during follow-up in the other patients. There were no patients with patent fenestrations at the time of both visits. There were no patients with large calibre changes or PA stenosis at the time of both visits.

The remaining 23 patients were included in the current analysis. Their characteristics are shown in table 1. Median age at first visit was 11.1 (9.5-16.0) years and 15.5 (12.5-22.7) at the second visit. Median follow-up duration between both visits was 4.4 (4.0-5.8) years. All patients underwent the Fontan operation before the age of 7 years. An atriopulmonary connection was performed in 2 patients, all other patients had a TCPC (ILT n=16, ECC n=5). In most TCPC-patients (17 out of 21) the TCPC was performed in a staged manner, preceded by a bidirectional Glenn shunt.

In 8 patients, the initial procedure consisted of the creation of a BT-shunt (Norwoord stage I excluded) and these patients were therefore considered to have an impaired pulmonary blood flow pre-surgery.

Table 1. Patient characteristics

Baseline parameters		patients baseline (n=23)	patients follow-up (n=23)	controls (n=16)
Male/Female (n)		16/7		8/8
Age at study (years)		11.1 (9.5-16.0)	15.5 (12.5-22.7)	13.5 (12.1-15.5)
BSA (m^2)		1.15 (1.02-1.78)	1.53 (1.28-1.77)	1.56 (1.36-1.69)
Age at Fontan completion (years)		3.3±1.6		
Follow-up since Fontan completion		8.1 (6.9-9.4)	12.3 (10.4-16.1)	
cardiac diagnosis (n)	Tricuspid atresia	7		
	Hypoplastic left heart syndrome	3		
	Double inlet left ventricle	5		
	Double outlet right ventricle	3		
	Other	5		
Dominant ventricle (n)	Left	17		
	Right	6		
Impaired Pulmonary blood flow pre-surgery		8		
Fontan Type	TCPC; ILT	16		
	TCPC; ECC	5		
	APC	2		
Pre Fontan procedures	BT-shunt	8		
	PA-banding	9		
	Norwood	3		
	Rashkind	2		
	Bidirectional Glenn	17		

BSA: body surface area, TCPC: total cavopulmonary connection, APC: atriopulmonary connection, ILT: intra-atrial lateral tunnel, ECC: extracardiac conduit, BT-shunt: Blalock-Taussig-shunt, PA-banding: pulmonary artery banding

Comparison with controls

Table 2 shows the results of MRI measurements and WSS calculations for controls as well as for both visits for the patients. Mean flow, maximal flow and pulsatility were all significantly lower in patients than in controls, for both visits. There was a large difference in pulsatility within the patient-group, between TCPC patients (range .22-2.88) and those with an APC (range 4.21-9.69). Mean and maximum areas were not significantly different between patients and controls, but distensibility was significantly lower in patients for both visits. Mean and maximal WSS were both significantly lower in patients, with the most distinct difference between patients and controls for maximal WSS.

Comparison between baseline and follow-up

The comparison between baseline and follow-up within the patients is also shown in table 2. Mean and maximal flows (corrected for BSA) were significantly higher at follow-

Table 2. Comparison of flow and WSS variables

	Controls	Patients		P-value
		Baseline	Follow-up	
HR (/min)	73±11	76±18	70±16	.112
Mean Flow (ml/sec/m^2)	33.5 (27.2-37.5)	15.1 (14.3-19.1)*	18.7 (14.0-22.6)*	.023
Max Flow (ml/sec/m^2)	101.8 (95.4-125.7)	23.8 (20.3-33.2)*	28.5 (24.4-37.5)*	.031
Pulsatility	3.32 (3.09-3.63)	1.05 (.73-2.21)*	1.19 (.59-1.79)*	.605
Mean Area (mm^2/m^2)	109±22	113±36	113±38	.966
Max Area (mm^2/m^2)	143±32	125±40	123±40	.730
Distensibility	.47±.13	.17±.05*	.15±.04*	.167
Mean WSS ((N/m^2)/ m^2)	.50 (.42-.57)	.36 (.26-.40)*	.31 (.26-.40)*	.068
Max WSS ((N/m^2)/ m^2)	1.45 (1.24-1.59)	.54 (.47-.62)*	.47 (.37-.62)*	.078

p-values indicate differences between baseline and follow-up,
*:significant difference between patients and controls, HR: heart rate, WSS: wall shear stress

up. While absolute (not corrected for BSA) mean and maximal area increased significantly (mean area: 156±54 mm^2 vs 173±57 mm^2, p=.005; max area: 186±66 mm^2 vs 203±65 mm^2, p=.010, figure 1), BSA corrected mean and maximal areas did not change. Distensibility and pulsatility were comparable between both visits. There was a trend towards lower mean and maximal WSS at the second visit, but the range of values was wide.

Predictors for WSS

Results of multivariable regression analysis for WSS ((N/m^2)/ m^2) are shown in table 3. Log age, mean area, mean flow, pulsatility and distensibility were entered in the model. Since pulsatility was much higher in APC patients, these were excluded from the mul-

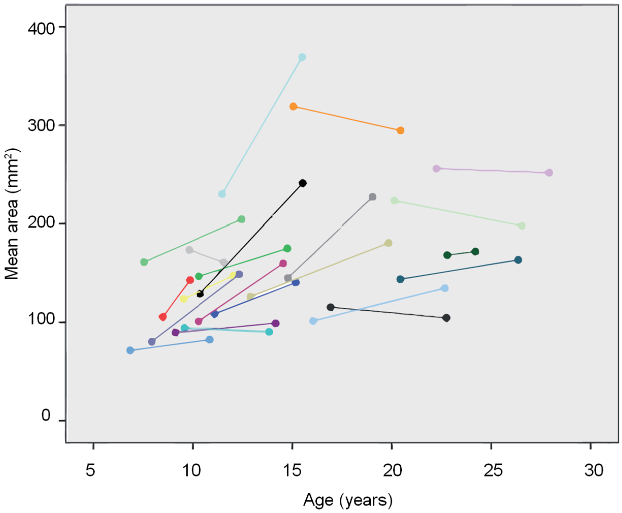

Figure 1. Mean cross-sectional area (mm^2) per patient vs. age (years)

tivariable analysis. Pulsatility and distensibility did not show a significant relation with WSS. In the final model log age, mean flow and mean area explain 85% of the variability in WSS.

Table 3. Multivariable regression model (for TCPC patients only) for mean WSS ((N/m^2)/ m^2)

variable	β	p-value	R^2
constant	1.227	<.001	.845
log Age (log years)	-.727	<.001	
Mean Flow (ml/sec/m^2)	.022	<.001	
Mean Area (mm^2/m^2)	-.004	<.001	

DISCUSSION

This study shows that PA size in growing Fontan patients is comparable to healthy controls and increases with age, appropriate to body size. Flow in the LPA increased significantly between both visits, but was still lower than in healthy controls. Pulsatility and distensibility were impaired and did not change over time, despite increase in flow. WSS was not significantly different between baseline and follow-up. Multivariable regression analysis revealed that age, mean flow and mean area are important predictors for WSS that explain most of the variability.

PA size

Several studies have assessed the range of branch PA size in healthy children and the relation with age and/or body size. Using contrast enhanced MRI Knobel and colleagues have shown that there is a linear relation between BSA and PA-size[8]. Using echocardiography, an older study showed a similar trend in younger children[9]. Our results indicate that LPA growth is proportionate to BSA in Fontan patients.

Only a few studies have investigated pulmonary artery size in Fontan patients using MRI. LPA size in our patients was comparable to that found in a previous smaller sample from our institutions[3]. Bellsham-Revell and colleagues investigated growth of the LPA between the hemi-Fontan stage and the TCPC in patients with hypoplastic left heart syndrome (HLHS)[10]. The (BSA corrected) size of the LPA pre-TCPC in their study was comparable to the values that we have presented. In the study by Bellsham-Revell it was found that, while there was an increase in area of the proximal LPA between stages, there was a relative decrease in size of the narrowest part of the LPA. The authors stated that the staged Fontan approach might be a risk factor itself for the narrowing of the LPA in these HLHS patients[10]. Earlier studies have shown that LPA-stenosis is a well-known problem, particularly in HLHS patients[11]. In our population there were only a few patients with HLHS. LPA areas in these patients (range 50-102 mm^2/m^2) were among the lowest sizes measured in our study. The previous studies and our results emphasize the need for close surveillance in this specific group.

Other studies have used X-ray catheter-assisted angiography to measure PA size, usually using the Nakata-index[12,13]. Although this makes comparison challenging, a previous study in patients with congenital heart disease has shown excellent agreement between angiography and MRI measurements of the great arteries, including branch pulmonary arteries[14].

In a recent study, Schmitt et al. found a decreased Nakata index of 150 mm^2/m^2 in 10 Fontan patients[15]. Converting this number into a single PA branch area as we have measured would result in a PA size of 75 mm^2/m^2, which is lower than we found. This difference might be explained by the fact that patients in the study by Schmitt were older and all of their patients had an unfenestrated extracardiac conduit Fontan.

Few studies have assessed PA size longitudinally after Fontan-completion. Baek and colleagues found that patients with a small PA before Fontan operation did not have a worse outcome 12.8 years after the Fontan-completion[16]. This is supported by a more recent study, indicating that small PA's are not an indication to postpone Fontan-completion[13]. One study showed that Nakata-index decreased after Fontan-completion, but did not affect functional outcome[17]. Another retrospective study also showed that PA growth failed to match the increase in BSA in Fontan patients[5]. A recent study by Restrepo and colleagues, using MRI-derived 3D-reconstructions of 25 TCPC patients, showed a similar trend. While there was an increase in absolute vessel diameters, normalized diameters decreased significantly with age[4]. This is in contrast to our measurements. This might be caused by the different in methods for quantification of PA size and in the duration of the follow-up. In our study, we included older patients at baseline, who did therefore not have significant somatic growth between the two MRI studies.

PA function

Interestingly, there was a significant increase in flow normalized to BSA in our patients between baseline and follow-up. This is in contrast to a recent MRI study among 25 TCPC patients with follow-up duration comparable to our study, showing no changes in flow corrected for BSA[4]. It remains unclear whether and how adjustment of the pulmonary circulation to the Fontan circulation occurs.

WSS is known to be lower in Fontan patients as compared to healthy controls. We found reduced levels of mean and maximal WSS relative to healthy subjects which is in accordance with an earlier study[3]. Impairment of WSS in Fontan patients most likely results from a combination of reduced pulmonary flow and nearly absent pulsatility[3]. In multi-variable regression analysis (the logarithm of) age was an important predictor of WSS, independently from both body size and PA area. Loss of pulsatility of blood flow and therefore lower mean and maximal WSS values have been associated with endothelial dysfunction of the PA's[18,19].

In a study of 10 young patients, reduced pulsatility after bidirectional Glenn was correlated to impaired endothelial relaxation[19]. Another study has demonstrated abnormal response of the PA's to exogenous nitrous oxide (NO) in Fontan patients[20]. Supplemental NO led to a fall in PVR, suggesting an elevated basal PVR, possibly related to endothelial dysfunction[20]. A lack of WSS could result in deterioration of endothelial function, mediated by endothelin, a potent vasoconstrictor. A study comparing endothelin receptor expression in failed and non-failed Fontan patients, has shown an overexpression of these receptors in the failed Fontan group[21].

WSS is also decreased in patients with pulmonary arterial hypertension (PAH). In contrast to Fontan patients, PAH patients have dilated pulmonary arteries, due to a longstanding elevated mean PA pressure[22]. Studies have shown a negative correlation between vessel size and WSS. It has been hypothesized that the decreased WSS in PAH patients leads to an increased arterial stiffness and reduced distensibility of the PA's[22,23].

The reduced level of WSS does not only influence the function of the PA's but it also affects the structure of the vessel wall according to a case-report of a 35-year old Fontan patient (APC). Immunohistological analysis revealed serious changes in the composition of the (main) pulmonary artery wall[24]. There was a profound reduction of muscular component and fragmentation of elastic fibers, wich might influence distensibility and the vasodilatory ability. It is likely that this is also true for younger Fontan patients, operated upon according to current techniques, but this should be further investigated.

Clinical implications

It has been demonstrated that exercise capacity is reduced in Fontan patients and it reduces further with age[25]. In the current study, we have shown that WSS is low in Fontan patients. The reduced WSS might influence endothelial function in the PA's. In healthy subjects, there is an increase of distensibility during exercise with an increase in the release of NO[26]. This induces vasodilatation and enhances pulmonary blood flow by a decrease in pulmonary vascular resistance. In Fontan patients, there often is an increase in pulmonary vascular resistance during exercise, indicating that this mechanism is impaired. This contributes to impaired ventricular filling[27]. A previous study from our institution showed that Fontan patients are not able to increase stroke volume during exercise[28]. Other studies have shown similar results[29]. The abnormal function of the PA's thus has direct consequences for exercise function of the patients, and may contribute to decline of exercise capacity.

Several studies have raised concerns about the growth of PA's after volume unloading or Fontan completion, but our results show that the long-term ability to grow is still present after Fontan completion. However the obvious reduction in WSS may have important implications for PA function late after Fontan, especially for the ability for dilation during exercise.

Considering these observations, it is of utmost importance to be able to influence pulmonary vascular resistance in the Fontan circulation. Several studies using bosentan, an endothelin-receptor antagonist, have not shown significant improvement[30,31]. Another study using sildenafil, a phosphodiesterase-5 inhibitor, to assess the influence during exercise in Fontan patients, showed an increase in stroke volume and cardiac index and a decrease in PVR during exercise[29]. Exercise capacity improved after sildenafil administration, but mainly in those patients with a poor baseline exercise capacity. This indicates that the reduced endothelial function could be attenuated to affect exercise capacity. In another study sildenafil was administered for a period of 6 weeks, but failed to show a significant improvement in exercise capacity[32]. It has been speculated that this result was caused by the fact that relatively fit Fontan patients were included[33]. Further studies are necessary to identify those patients that benefit the most from this potential therapy or to uncover other potential targets and means for possible therapeutical intervention.

Limitations

Sample size was relatively small and the Fontan-population is heterogeneous with respect to different cardiac diagnoses. The subgroups were too small for group-to-group comparison. This study assumes laminary flow in the PA's for the calculation of WSS. Although care was taken not to measure flow too close to the caval connection point, flow disturbances may have been present, depending on the individual anatomy and intravascular flow pattern in patients. Since measurements were performed in one of the branch pulmonary arteries, this study does not provide direct knowledge on the smaller pulmonary vasculature further downstream.

CONCLUSIONS

WSS in Fontan patients is decreased as compared to healthy controls. Pulsatility and distensibility are also significantly lower. Pulmonary artery size however, is not significantly different from healthy controls and growth after Fontan-operation remains proportionate to body size.

REFERENCES

[1] Khairy P, Poirier N, Mercier LA (2007) Univentricular heart. Circulation 115: 800-812

[2] Hager A, Fratz S, Schwaiger M, Lange R, Hess J, Stern H (2008) Pulmonary blood flow patterns in patients with Fontan circulation. Ann Thorac Surg 85: 186-191

[3] Robbers-Visser D, Helderman F, Strengers JL, van Osch-Gevers L, Kapusta L, Pattynama PM, Bogers AJ, Krams R, Helbing WA (2008) Pulmonary artery size and function after Fontan operation at a young age. J Magn Reson Imaging 28: 1101-1107

[4] Restrepo M, Mirabella L, Tang E, Haggerty CM, Khiabani RH, Fynn-Thompson F, Valente AM, McElhinney DB, Fogel MA, Yoganathan AP (2014) Fontan pathway growth: a quantitative evaluation of lateral tunnel and extracardiac cavopulmonary connections using serial cardiac magnetic resonance. Ann Thorac Surg 97: 916-922

[5] Tatum GH, Sigfusson G, Ettedgui JA, Myers JL, Cyran SE, Weber HS, Webber SA (2006) Pulmonary artery growth fails to match the increase in body surface area after the Fontan operation. Heart 92: 511-514

[6] Cheng C, Helderman F, Tempel D, Segers D, Hierck B, Poelmann R, van Tol A, Duncker DJ, Robbers-Visser D, Ursem NT, van Haperen R, Wentzel JJ, Gijsen F, van der Steen AF, de Crom R, Krams R (2007) Large variations in absolute wall shear stress levels within one species and between species. Atherosclerosis 195: 225-235

[7] Duivenvoorden R, Vanbavel E, de Groot E, Stroes ES, Disselhorst JA, Hutten BA, Lameris JS, Kastelein JJ, Nederveen AJ (2010) Endothelial shear stress: a critical determinant of arterial remodeling and arterial stiffness in humans--a carotid 3.0-T MRI study. Circ Cardiovasc Imaging 3: 578-585

[8] Knobel Z, Kellenberger CJ, Kaiser T, Albisetti M, Bergstrasser E, Buechel ER (2011) Geometry and dimensions of the pulmonary artery bifurcation in children and adolescents: assessment in vivo by contrast-enhanced MR-angiography. Int J Cardiovasc Imaging 27: 385-396

[9] Salim MA, DiSessa TG, Arheart KL, Alpert BS (1995) Contribution of superior vena caval flow to total cardiac output in children. A Doppler echocardiographic study. Circulation 92: 1860-1865

[10] Bellsham-Revell HR, Tibby SM, Bell AJ, Witter T, Simpson J, Beerbaum P, Anderson D, Austin CB, Greil GF, Razavi R (2013) Serial magnetic resonance imaging in hypoplastic left heart syndrome gives valuable insight into ventricular and vascular adaptation. J Am Coll Cardiol 61: 561-570

[11] Barron DJ, Kilby MD, Davies B, Wright JG, Jones TJ, Brawn WJ (2009) Hypoplastic left heart syndrome. Lancet 374: 551-564

[12] Kansy A, Brzezinska-Rajszys G, Zubrzycka M, Mirkowicz-Malek M, Maruszewski P, Manowska M, Maruszewski B (2013) Pulmonary artery growth in univentricular physiology patients. Kardiologia polska 71: 581-587

[13] Lehner A, Schuh A, Herrmann FE, Riester M, Pallivathukal S, Dalla-Pozza R, Kozlik-Feldmann R, Netz H, Malec E, Januszewska K (2014) Influence of pulmonary artery size on early outcome after the fontan operation. Ann Thorac Surg 97: 1387-1393

[14] Valsangiacomo Buchel ER, DiBernardo S, Bauersfeld U, Berger F (2005) Contrast-enhanced magnetic resonance angiography of the great arteries in patients with congenital heart disease: an accurate tool for planning catheter-guided interventions. Int J Cardiovasc Imaging 21: 313-322

[15] Schmitt B, Steendijk P, Ovroutski S, Lunze K, Rahmanzadeh P, Maarouf N, Ewert P, Berger F, Kuehne T (2010) Pulmonary vascular resistance, collateral flow, and ventricular function in patients with a Fontan circulation at rest and during dobutamine stress. Circ Cardiovasc Imaging 3: 623-631

[16] Baek JS, Bae EJ, Kim GB, Kim WH, Lee JR, Kim YJ, Park EA, Lee W, Noh CI (2011) Pulmonary artery size and late functional outcome after Fontan operation. Ann Thorac Surg 91: 1240-1246

[17] Adachi I, Yagihara T, Kagisaki K, Hagino I, Ishizaka T, Kobayashi J, Kitamura S, Uemura H (2007) Preoperative small pulmonary artery did not affect the midterm results of Fontan operation. Eur J Cardiothorac Surg 32: 156-162

[18] Klimes K, Abdul-Khaliq H, Ovroutski S, Hui W, Alexi-Meskishvili V, Spors B, Hetzer R, Felix R, Lange PE, Berger F, Gutberlet M (2007) Pulmonary and caval blood flow patterns in patients with intracardiac and extracardiac Fontan: a magnetic resonance study. Clin Res Cardiol 96: 160-167

[19] Kurotobi S, Sano T, Kogaki S, Matsushita T, Miwatani T, Takeuchi M, Matsuda H, Okada S (2001) Bidirectional cavopulmonary shunt with right ventricular outflow patency: the impact of pulsatility on pulmonary endothelial function. J Thorac Cardiovasc Surg 121: 1161-1168

[20] Khambadkone S, Li J, de Leval MR, Cullen S, Deanfield JE, Redington AN (2003) Basal pulmonary vascular resistance and nitric oxide responsiveness late after Fontan-type operation. Circulation 107: 3204-3208

[21] Ishida H, Kogaki S, Ichimori H, Narita J, Nawa N, Ueno T, Takahashi K, Kayatani F, Kishimoto H, Nakayama M, Sawa Y, Beghetti M, Ozono K (2012) Overexpression of endothelin-1 and endothelin receptors in the pulmonary arteries of failed Fontan patients. Int J Cardiol 159: 34-39

[22] Truong U, Fonseca B, Dunning J, Burgett S, Lanning C, Ivy DD, Shandas R, Hunter K, Barker AJ (2013) Wall shear stress measured by phase contrast cardiovascular magnetic resonance in children and adolescents with pulmonary arterial hypertension. J Cardiovasc Magn Reson 15: 81

[23] Tang BT, Pickard SS, Chan FP, Tsao PS, Taylor CA, Feinstein JA (2012) Wall shear stress is decreased in the pulmonary arteries of patients with pulmonary arterial hypertension: An image-based, computational fluid dynamics study. Pulmonary circulation 2: 470-476

[24] Adachi I, Ueno T, Hori Y, Sawa Y (2010) Alterations in the medial layer of the main pulmonary artery in a patient with longstanding Fontan circulation. Interact Cardiovasc Thorac Surg 11: 682-683

[25] Bossers SS, Helbing WA, Duppen N, Kuipers IM, Schokking M, Hazekamp MG, Bogers AJ, Ten Harkel AD, Takken T (2014) Exercise capacity in children after total cavopulmonary connection: lateral tunnel versus extracardiac conduit technique. J Thorac Cardiovasc Surg 148: 1490-1497

[26] Green DJ, Spence A, Rowley N, Thijssen DH, Naylor LH (2012) Vascular adaptation in athletes: is there an ‘athlete’s artery’? Experimental physiology 97: 295-304

[27] Gewillig M, Brown SC, Eyskens B, Heying R, Ganame J, Budts W, Gerche AL, Gorenflo M (2010) The Fontan circulation: who controls cardiac output? Interact Cardiovasc Thorac Surg 10: 428-433

[28] Robbers-Visser D, Jan Ten Harkel D, Kapusta L, Strengers JL, Dalinghaus M, Meijboom FJ, Pattynama PM, Bogers AJ, Helbing WA (2008) Usefulness of cardiac magnetic resonance imaging combined with low-dose dobutamine stress to detect an abnormal ventricular stress response in children and young adults after fontan operation at young age. Am J Cardiol 101: 1657-1662

[29] Van De Bruaene A, La Gerche A, Claessen G, De Meester P, Devroe S, Gillijns H, Bogaert J, Claus P, Heidbuchel H, Gewillig M, Budts W (2014) Sildenafil improves exercise hemodynamics in fontan patients. Circ Cardiovasc Imaging 7: 265-273

[30] Schuuring MJ, Vis JC, van Dijk AP, van Melle JP, Vliegen HW, Pieper PG, Sieswerda GT, de Bruin-Bon RH, Mulder BJ, Bouma BJ (2013) Impact of bosentan on exercise capacity in adults after the Fontan procedure: a randomized controlled trial. Eur J Heart Fail: 2013 Jun;15(6):690-8

[31] Ovaert C, Thijs D, Dewolf D, Ottenkamp J, Dessy H, Moons P, Gewillig M, Mertens L (2009) The effect of bosentan in patients with a failing Fontan circulation. Cardiol Young 19: 331-339

[32] Goldberg DJ, French B, McBride MG, Marino BS, Mirarchi N, Hanna BD, Wernovsky G, Paridon SM, Rychik J (2011) Impact of oral sildenafil on exercise performance in children and young adults after the fontan operation: a randomized, double-blind, placebo-controlled, crossover trial. Circulation 123: 1185-1193

[33] Hager A, Weber R, Muller J, Hess J (2014) Predictors of sildenafil effects on exercise capacity in adolescents and adults with Fontan circulation. Clin Res Cardiol: Aug;103(8):641-6

Chapter 9

The effect of exercise training on pulmonary artery wall shear stress, distensibility and pulsatility in children and young adults with Fontan circulation: a randomized controlled trial

Based on:

Duppen N, Cibis M, Wentzel JJ, Bossers S, Potters W, Moelker A, Kapusta L, Hopman M, Helbing W, The effect of exercise training on pulmonary artery wall shear stress, distensibility and pulsatility in children and young adults with Fontan circulation: a randomized controlled trial. Submitted.

ABSTRACT

Introduction

Vascular endothelial-dysfunction is common in the pulmonary artery (PA) in patients with a Fontan circulation. The flow through the Fontan PA depends highly on pulmonary vascular resistance (PVR). A slight increase in PVR can result in decreased ventricular preload and cardiac output, which may contribute to decreased exercise capacity. PVR can be reduced by endothelial released nitric oxide. PA wall shear stress (WSS) regulates this release. We hypothesized that exercise training would enhance WSS and thereby may result in favorable changes in PA endothelial-function.

Methods

A multi-center randomized controlled trial was conducted in Fontan patients (10 to 25 years). The exercise-group (n=28) received a 12-week exercise training program, 3 times per week, the control-group (n=17) did not. Healthy controls (n=17) underwent magnetic resonance only at rest whereas Fontan participants were studied at rest and with dobutamine stress (7.5 µg/kg/min). WSS, distensibility and pulsatility of the PA were calculated.

Results

Fontan patients had significantly lower WSS, distensibility and pulsatility compared to healthy controls (WSS: 0.57 ± 0.23 N/m^2 vs 0.82 ± 0.21 N/m^2; p=0.001; distensibility: 0.18 ± 0.05 vs 0.40 ± 0.30; p= 0.012; pulsatility: 1.13 ± 0.61 vs 3.40 ± 0.37; $p<0.001$). The training program did not change WSS, distensibility and pulsatility within the exercise-group, or between the exercise and control-group. At baseline predicted-peakVO_2 was 80% in Fontan patients.

Conclusion

Exercise training did not alter WSS in relatively healthy Fontan patients. Further research is needed to unravel the key to increase WSS and PA endothelial-function.

INTRODUCTION

In patients with univentricular hearts and a Fontan circulation (Fontan patients), the caval veins are directly connected to the pulmonary artery (PA)[1]. As a result of the Fontan operation, the pre-pulmonary pump function of the heart is lost[1]. The flow through the PA in this situation depends on the transpulmonary pressure gradient and pulmonary vascular resistance (PVR)[1]. In contrast to healthy peers, a slight increase in PVR results in decrease of ventricular preload and thus cardiac output[1]. This may contribute to decreased exercise capacity in Fontan patients and may relate to poor long-term outcome[2,3]. Recent studies have explored the possibilities to increase cardiac output in Fontan patients by decreasing PVR with drugs[4,5]. Most of these studies have not demonstrated beneficial effect and drug use may be accompanied by adverse effects, so alternative strategies to influence PVR may be required[4,5,6].

Shear stress at the vessel wall and pulsatility in the vessel regulate the release of nitric oxide by the endothelium[7]. Nitric oxide, acting as a local vasodilator, contributes to maintain low PVR[1]. Low wall shear stress (WSS) and loss of distensibility due to loss of pulsatility in the PA have been related to pulmonary vascular dysfunction in the Fontan circulation[8]. In healthy individuals, heart rate and stroke volume increase during exercise. This results in increased NO release and decreased PVR, allowing blood flow through the PA to increase. Prolonged exercise training in healthy subjects results in short term functional adaptation and longer term structural changes in the large arteries, increasing vascular diameter and decreasing vascular resistance[9]. These mechanisms could be of benefit to influence PA endothelial-function in Fontan patients.

Several studies in small heterogeneous congenital heart disease (ConHD) patient groups, which included Fontan patients, have shown that exercise training can improve exercise capacity[10]. Aim of the study was to assess WSS, distensibility and pulsatility before and after a 12 week standardized aerobic exercise training program in patients with a Fontan circulation. We hypothesized that exercise training would increase WSS, pulsatility and distensibility, thereby improving PA endothelial-function.

METHODS

A multi-center prospective randomized controlled trial was conducted in 5 tertiary referral centers for ConHD in the Netherlands. The study was designed according to Consolidated Standards of Reporting Trials (CONSORT) guidelines[11]. The study is registered at www.trialregister.nl, identification number NTR2731.

Participants

Patients with a Fontan circulation (Fontan patients) between 10 to 25 years were eligible. Seventeen age-matched healthy controls, that did not undergo exercise training, were also included in the study. Exclusion criteria were patients with a ventricular outflow tract obstruction, measured as Doppler echo pressure gradient >60 mmHg, and patients that were mentally or physically unable to follow a training program, as indicated by their own physician. The study complied with the Declaration of Helsinki. The research protocol was approved by the institutional Ethics Committees. All participants (and/or their parents if required) gave written informed consent.

Intervention

Fontan patients were randomized in a 2 to 1 allocation ratio to either the exercise or control-group by an independent blinded researcher. Stratification was based on gender and age group (10-12 years, 13-14 years, 15-17 years, and 18-25 years). All participants underwent a standardized stepwise bicycle cardiopulmonary exercise test as described by Bossers et al[2].

The exercise-group was enrolled in a 12 week, 3 times per week 1 hour standardized aerobic dynamic exercise training program, supervised by local physiotherapists. A heart rate monitor (SR400, Polar Electro BV, the Netherlands) was given to the patients to ensure execution of the program within the predetermined submaximal heart rate range (60-70% of heart rate reserve). The control-group was instructed to continue their normal daily live. The healthy peers were only included in the baseline measurements.

Magnetic resonance imaging

All participants underwent cardiac magnetic (MR) resonance imaging on the locally available whole body MR scanners (Philips Panorama 1T; Siemens Avanto 1.5T; GE Signa 1.5T; GE Discovery 1.5T; Philips Achieva 1.5T and Philips Ingenia 1.5T) according to previously described methods, at baseline and directly after the 12 week intervention period[12]. Briefly, MR imaging was performed using a phase-contrast (PC) acquisition with an unidirectional velocity encoding range of 60 to 120 cm/s to measure the blood flow inside the PA. In-plane resolution of PC MR images was between 1.13-1.25 mm, slice thickness was 6 mm. This protocol resulted in flow measurements with 18-30 frames per cardiac cycle. Images were acquired and averaged over 3 heart cycles to diminish the effect of respiration. Dobutamine was administered to mimic physical exercise at a rate of 7.5 µg/kg/min. Low-dose dobutamine stress images were only acquired when logistically possible and if the patient consented. Flow measurements were repeated after reaching a steady heart rate, using the same parameters as in the rest conditions. Contours of the pulmonary artery were drawn semi-automatically with the software package QFLOW (Medis Medical Imaging Systems, Leiden, the Netherlands).

Wall shear stress, distensibility and pulsatility

In order to assess local WSS, distensibility and pulsatility, we used an algorithm which was adapted from Duivenvoorden et al[13]. In short, blood velocities were calculated inside the contours of the pulmonary arteries by using PC MR phase difference images. The cross-section was divided into four segments with 10 degrees of overlap. In each segment, the velocities were projected onto one plane. In this plane, only velocities located within an inward distance of 0.5 pixels and 3 pixels were excluded. A second order curve fit was applied on the projected velocities, while forcing blood velocity to be zero at the lumen wall, to calculate the local spatial derivative of the velocity perpendicular to the wall, wall shear rate. WSS was calculated by multiplying WSR with the blood viscosity which was set to 3.2 10^{-3} Pa·s for all time intervals. The WSS values of 4 segments were averaged to obtain mean cross-sectional WSS which was necessary to eliminate the adverse effect of complex flow on the WSS estimation. For the analysis, cardiac cycle averaged WSS was calculated.

Distensibility was defined as the maximum change in the cross-sectional area within one cardiac cycle and pulsatility was defined as the flow change within one cardiac cycle and calculated as the following formulas:

$$\textit{distensibility} = \frac{\textit{(maximal area-minimal area)}}{\textit{maximal area}}$$

$$\textit{pulsatility} = \frac{\textit{(maximal flow-minimal flow)}}{\textit{mean flow}}$$

WSS, distensibility and pulsatility were calculated at one cross-section in the left pulmonary artery (LPA) in Fontan patients. In healthy controls WSS, distensibility and pulsatility were calculated in the right pulmonary artery (RPA). LPA was measured in Fontan patients due to due to the short distance between the connection of the superior vena cava and the first branching point in the RPA. LPA and RPA do not differ in absolute blood flow and peak velocity, as shown by Robbers et al[8].

Statistical analysis

Differences in parameters between Fontan patients and healthy controls were analyzed by independent t-tests. Differences in parameters between Fontan exercise-group and Fontan control-group were analyzed by two-way (repeated measures) ANOVA. Within group (Fontan exercise-group and Fontan control-group) differences from baseline to follow-up were analyzed by paired Student's t-tests. We considered a p-value of <0.05 (2-sided test) as statistically significant.

RESULTS

Study population

Forty-five patients and 17 healthy controls participated in this study. Age at study and age at Fontan completion did not significantly differ between the participants and the non-participants (n=87). Significantly more female than male patients declined to participate. We specified 3 groups, a Fontan exercise-group (n=28), a Fontan control-group (n=17) and a healthy peer control-group (n=17). Two patients in the Fontan exercise-group dropped out. We were able to analyze the MRI images of 20 of the 26 patients in the Fontan exercise group and 12 of the 17 patients in the Fontan control-group. Gender, age at study, length and weight did not significantly differ between the healthy controls and the Fontan patients (table 1). Baseline characteristics between the Fontan exercise-group and the Fontan control-group did not significantly differ either (table 1). Twenty Fontan patients were randomized to the exercise-group. Attendance rate was 92% (median, inter quartile rage 78-100%). The heart rate monitors showed that the training intensity was within the set heart rate range during exercise.

Table 1. Baseline characteristics, healthy controls and Fontan patients

	Healthy controls (n = 17)	**All Fontan patients** (n = 32)	**Randomization (Fontan patients)**	
			Exercise-group (n = 20)	Control-group (n = 12)
Male (n)	8 (47%)	23 (72%)	14 (70%)	9 (75%)
Length (cm)	164 ± 10	160 ± 14	160 ± 16	160 ± 11
Weight (kg)	52 ± 11	49 ± 14	52 ± 15	46 ± 11
Age (yrs)	13 ± 2	15 ± 4	15 ± 4	15 ± 4
Age at Fontan (yrs)		3.5 ± 1.5	3.6 ± 1.3	3.4 ± 1.8
Follow-up post Fontan (yrs)		11 ± 3	11 ± 3	11 ± 4
Oxygen saturation (%)		95 ± 2	95 ± 2	94 ± 2
Percentage predicted peak VO_2 (%)		82 ± 18	78 ± 18	87 ± 17
Dominant ventricle				
Left		23 (72%)	14 (70%)	9 (75%)
Right		9 (28%)	6 (30%)	3 (25%)
Fontan type				
Intra-atrial lateral tunnel		17 (53%)	11 (55%)	6 (50%)
Extra cardiac conduit		13 (41%)	8 (40%)	5 (42%)
Conversion		2 (6%)	1 (5%)	1 (8%)
Medication				
Oral anticoagulants/platelet inhibitors		32	20	12
Beta-blockers		3	3	0
Digoxine		1	0	1
Arrhythmic event in history		6	4	2
Post Fontan interventions		5	2	3

P-value < 0.05 based on independent t-test (indicated by *); healthy controls vs all patients and Fontan exercise-group vs Fontan control-group.

Differences in wall shear stress, distensibility, pulsatility and flow between healthy controls and Fontan patients

In pre-and post-training period exercise tests, no differences were observed for peakVO_2 and peak workload.

Healthy controls had significantly higher WSS (1.4 times higher), distensibility (2.2 times higher), pulsatility (3 times higher) and flow (1.8 times higher) in the PA as well as a greater maximum area of the PA (1.2 times greater) than Fontan patients (table 2).

Changes in wall shear stress, distensibility, pulsatility and flow in Fontan patients at follow-up

WSS, distensibility, pulsatility and flow did not change after the intervention period within the Fontan exercise-group and Fontan control-group. The change of all parameters as observed from baseline to follow-up in the Fontan exercise-group was not significantly different from the Fontan control-group (table 3).

Table 2. Healthy controls vs Fontan patients at baseline

	Healthy controls (n = 17)	Fontan patients (n = 32)	p-value
Wall shear stress (N/m^2)	0.82 ± 0.21	0.57 ± 0.23	0.001
Distensibility index	0.40 ± 0.30	0.18 ± 0.05	0.012
Mean area (mm^2)	157 ± 46	155 ± 53	0.873
Max area (mm^2)	209 ± 55	171 ± 56	0.031
Pulsatility index	3.40 ± 0.37	1.13 ± 0.61	< 0.001
Mean flow (ml/s)	51 ± 14	29 ± 6	< 0.001
Heart rate (bpm)	73 ± 11	71 ± 14	0.666

P-value based on independent t-test.

Measurements of wall shear stress at rest and with dobutamine stress in Fontan patients

In general, WSS measured during dobutamine stress was significantly increased relative to rest condition (2-way ANOVA, $p<0.001$)(figure 1). However, at the follow-up assessment of the control group, the WSS increase after dobutamine did not reach statistical significance ($p=0.084$) (figure 1). The change in WSS within the exercise group was not significantly different than that within the control group. Distensibility, mean and maximal area in the LPA after dobutamine administration did not significantly differ than those at rest in both the exercise and control-group.

Table 3. Measurements before and after the exercise training program in Fontan patients

	Fontan exercise-group (n = 20)		Fontan control-group (n = 12)		
LPA	Before	After	Before	After	p
Wall shear stress (N/m^2)	0.55 ± 0.23	0.54 ± 0.23	0.59 ± 0.24	0.62 ± 0.32	0.53
Distensibility index	0.18 ± 0.06	0.20 ± 0.0	0.179 ± 0.055	0.18 ± 0.07	0.62
Mean area (mm^2)	158 ±51	155 ± 53	150 ± 59	156 ± 69	0.58
Max area (mm^2)	174 ± 54	174 ± 57	165 ± 61	171 ± 75	0.67
Pulsatility index	1.11 ± 0.94	1.26 ± 0.61	0.89 ± 0.43	0.82 ± 0.37	0.29
Mean flow (ml/s)	29 ± 6	28 ± 6	27 ± 6	29 ± 8	0.08
Heart rate (bpm)	70 ± 15	68 ± 15	73 ± 14	72 ±11	0.97

Legend: p-value relates to the between subjects comparisons, analyzed by two-way ANOVA; paired t-test within group, p<0.05 is indicated by *.

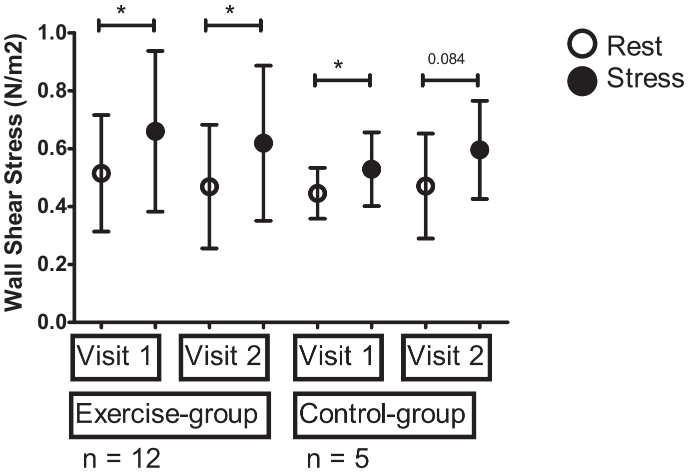

Figure 1. Wall Shear Stress rest and stress. P-value based on paired t-test. * p <0.05

DISCUSSION

This randomized controlled trial demonstrated that a 12 week aerobic exercise training program does not change wall shear stress, distensibility and pulsatility in the pulmonary arteries in Fontan patients. As WSS is an important determinant of NO-release mediated decrease of PVR, this suggests that PVR did not change.

Abnormal PA endothelial-function is common after the Fontan procedure and relates to the abnormal flow throughout the different stages towards and after completion of the Fontan circulation[3]. These factors have been associated with impaired pulmonary artery function[14]. As a result of the loss of the pre-pulmonary pump, ventricular preload is highly dependent on pulmonary vascular function in these patients[1,8]. PVR directly relates to PA endothelial-function which is mediated by NO[1,7,9]. Endothelial NO is released under the influence of wall shear stress, distensibility and pulsatility of the vessel[1,7,9]. In

Fontan patients, PA endothelial-function is hampered by a decrease of WSS, distensibility and pulsatility, as confirmed in the present study. This may result in a decrease of NO release[8].

It has been demonstrated that physical exercise training can result in changes in the large arteries of trained healthy subjects. Training results in adaptation of vasodilator capacity as well as in arterial remodeling[7]. During exercise WSS increases. Short term changes of exercise training are characterized by increased vasodilatation potential[9].

As in Fontan patients, PA WSS and distensibility are decreased in patients with pulmonary hypertension (PAH)[15]. In PAH patients therapy consists of (pulmonary) vasodilator drugs which reduce PVR and increases cardiac output in this population[15]. Results of trials with vasodilator drugs in Fontan patients have shown equivocal results[5,16,17,18].

Most studies using the endothelin antagonist bosentan have not shown beneficial results in Fontan patients[5,16]. Recently, Hebert et al. reported the largest bosentan study so far. In a randomized controlled trial with 3 months follow-up, a small but significant increase in peakVO$_2$, exercise capacity and NYHA functional class were demonstrated. Treatment responses tended to be greater in males, participants with a low body mass index, in young patients, and in those with high plasma ET-1. No difference was seen between patients with high and low baseline values of peakVo$_2$ and pro-BNP[6]. Although there were no serious adverse events, 8% of the subjects withdrew from the study for assumed adverse effects. In the studies that have administered phosphodiesterase 5 inhibitor sildenafil, an increase in exercise performance and ventricular stroke volume and a decrease of PVR was seen[17,18]. Sildenafil related improvement in exercise capacity was particularly noted in Fontan patients who had a poor baseline exercise capacity[17]. An intervention study in which sildenafil was administered to a relatively young and healthy cohort of Fontan patients for 6 weeks failed to show significant improvement in exercise capacity, but showed improved ventilatory efficiency[4]. The lack of significant peakVO$_2$ increase was attributed to the relatively healthy cohort, reducing the room for improvement of exercise capacity[17]. The difference in effect as shown in studies using bosentan or sildenafil most likely was related to the differences in their mode of action. Endothelin expression is enhanced in patients with a failing Fontan circulation[19]. Inhibition of the expression by bosentan will be mostly effective in those patients. Sildenafil inhibits, in all patients, phosphodiesterase-5, which increases cyclic GMP, part of the NO pathway, leading to pulmonary vasodilatation[18]. This would endorse the theory that NO release is altered in Fontan patients, as a result of vascular dysfunction[8,17].

In contrast to drug intervention studies, well-designed exercise training programs in Fontan patients have shown improved exercise capacity. In one study, it was shown that cardiac output increased following exercise training[10,20]. In analogy to the sildenafil studies, Fontan patients with a poorer baseline exercise capacity were more likely to enhance their exercise capacity than those with higher baseline values, which was confirmed in our Fontan patients with relatively well preserved baseline clinical state[2,17]. This is in contrast to the clear improvement in exercise performance in patients operated for tetralogy of Fallot at similar age who underwent the same exercise training protocol[21]. In acquired heart disease in adults, characteristics of arterial function have not shown a direct relationship with maximal exercise parameters. Furthermore, the effects of exercise training on arterial function have differed importantly throughout studies, which may in part depend on the underlying type of disease[22,23].

A potential problem in the use of sildenafil is side-effects that occur in relatively high percentage of patients. Exercise training lacks drug related side-effects, contributes to the reduction of obesity commonly seen in ConHD patients, may increase physical activity levels, as recommended in the current health guidelines, and contributes to an increase in domains of health related quality of life[24,25,26].

The exercise training program described in our study did not change measured parameters related to PA endothelial-function. This could indicate that the exercise training program did not influence the release of NO and PVR. It should be noted that our participants had a relative high peakVO$_2$ at baseline[27].

There may be several reasons why we did not find any changes following an extensive training program with good adherence. The duration of the training program may have been too short. The type of training may not have been adequate or the hypothesis that exercise training improves PA endothelial-function in these patients may be invalid.

WSS calculations were based on the actual velocity measured in vivo with PC MRI. Shear stress measurements are subject to variations because of interobserver variability in lumen segmentation. In order to prevent interobserver variability, the segmentations were performed in one go and by one person (ND). To calculate WSS, we assumed a parabolic curve of flow velocities across the vessel diameter[13]. This is a simplification of reality, as the flow profile will most likely not be parabolic due to the branched pattern of the PA system[28]. Computational fluid dynamics (CFD) simulations are the golden standard to assess flow velocity profiles and WSS. A recent study showed that PC MRI is as accurate as CFD in assessing WSS patterns[29]. Due to lack of pulsatility, and the anatomy of the Fontan circuit, blood flow inside Fontan circuit has a complex pattern which may cause some errors in 2D PC MRI measurement such as intra-voxel dephasing. By taking the mean WSS per cross-section, we calculated a general WSS value less sensitive to the local measurement errors.

In this study distensibility was assessed as the relative change in PA area. The relative changes in the PA area over the cardiac cycle are affected by both the arterial stiffness and the pressure variations. The lack of change in distensibility after a period of a standardized training protocol might be caused by counteracting influences of arterial stiffness and pulse pressure. Since pulsatility in flow did not change due to a training protocol, the data make it plausible that the arterial stiffness did not change over the study period.

Results were obtained using simulated exercise with dobutamine. There are differences in the circulatory response between physiological and pharmacological stress, however dobutamine mimics physical stress at low dose[30]. As described by Robbers et al. dobutamine in low dose increases heart rate and cardiac index in young Fontan patients[31]. The Results (data not shown) in the current study were similar with respect to the effect type and size.

In conclusion, WSS, distensibility and pulsatility, which are lower in Fontan patients than in healthy peers, did not change in response to exercise training in a relatively healthy group of Fontan patients. Considering the important clinical need to influence PA endothelial-function in these patients, further research is needed to assess the potential of exercise training to enhance PA endothelial-function in Fontan patients.

REFERENCES

[1] Gewillig M, Brown SC, Eyskens B, et al. The Fontan circulation: who controls cardiac output? Interact Cardiovasc Thorac Surg 2010;10:428-33.

[2] Bossers SS, Helbing WA, Duppen N, et al. Exercise capacity in children after total cavopulmonary connection: Lateral tunnel versus extracardiac conduit technique. J Thorac Cardiovasc Surg 2014;1:1-8.

[3] Gewillig M. The Fontan circulation. Heart 2005;91:839-46.

[4] Goldberg DJ, French B, McBride MG, et al. Impact of oral sildenafil on exercise performance in children and young adults after the fontan operation: a randomized, double-blind, placebo-controlled, crossover trial. Circulation 2011;123:1185-93.

[5] Schuuring MJ, Vis JC, van Dijk AP, et al. Impact of bosentan on exercise capacity in adults after the Fontan procedure: a randomized controlled trial. Eur J Heart Fail 2013;15:690-8.

[6] Hebert A, Mikkelsen UR, Thilen U, et al. Bosentan improves exercise capacity in adolescents and adults after Fontan operation: the TEMPO (Treatment With Endothelin Receptor Antagonist in Fontan Patients, a Randomized, Placebo-Controlled, Double-Blind Study Measuring Peak Oxygen Consumption) study. Circulation 2014;130:2021-30.

[7] Green DJ, Spence A, Rowley N, et al. Vascular adaptation in athletes: is there an ‘athlete’s artery’? Experimental physiology 2012;97:295-304.

[8] Robbers-Visser D, Helderman F, Strengers JL, et al. Pulmonary artery size and function after Fontan operation at a young age. J Magn Reson Imaging 2008;28:1101-7.

[9] Green DJ. Exercise training as vascular medicine: direct impacts on the vasculature in humans. Exerc Sport Sci Rev 2009;37:196-202.

[10] Duppen N, Takken T, Hopman MT, et al. Systematic review of the effects of physical exercise training programmes in children and young adults with congenital heart disease. Int J Cardiol 2013;168:1779-87.

[11] Schulz KF, Altman DG, Moher D, et al. CONSORT 2010 statement: updated guidelines for reporting parallel group randomised trials. BMJ 2010;340:c332.

[12] Robbers-Visser D, Luijnenburg SE, van den Berg J, et al. Safety and observer variability of cardiac magnetic resonance imaging combined with low-dose dobutamine stress-testing in patients with complex congenital heart disease. Int J Cardiol 2011;147:214-8.

[13] Duivenvoorden R, Vanbavel E, de Groot E, et al. Endothelial shear stress: a critical determinant of arterial remodeling and arterial stiffness in humans--a carotid 3.0-T MRI study. Circ Cardiovasc Imaging 2010;3:578-85.

[14] Gewillig M, Brown SC, Heying R, et al. Volume load paradox while preparing for the Fontan: not too much for the ventricle, not too little for the lungs. Interact Cardiovasc Thorac Surg 2010;10:262-5.

[15] Tang BT, Pickard SS, Chan FP, et al. Wall shear stress is decreased in the pulmonary arteries of patients with pulmonary arterial hypertension: An image-based, computational fluid dynamics study. Pulmonary circulation 2012;2:470-6.

[16] Ovaert C, Thijs D, Dewolf D, et al. The effect of bosentan in patients with a failing Fontan circulation. Cardiol Young 2009;19:331-9.

[17] Hager A, Weber R, Muller J, et al. Predictors of sildenafil effects on exercise capacity in adolescents and adults with Fontan circulation. Clin Res Cardiol 2014;3:1-6.

[18] Van De Bruaene A, La Gerche A, Claessen G, et al. Sildenafil improves exercise hemodynamics in fontan patients. Circ Cardiovasc Imaging 2014;7:265-73.

[19] Ishida H, Kogaki S, Ichimori H, et al. Overexpression of endothelin-1 and endothelin receptors in the pulmonary arteries of failed Fontan patients. Int J Cardiol 2012;159:34-9.

[20] Cordina RL, O'Meagher S, Karmali A, et al. Resistance training improves cardiac output, exercise capacity and tolerance to positive airway pressure in Fontan physiology. Int J Cardiol 2013;168:780-8.

[21] Duppen N, Kapusta L, de Rijke YB, et al. The effect of exercise training on cardiac remodelling in children and young adults with corrected tetralogy of Fallot or Fontan circulation: a randomized controlled trial. Int J Cardiol 2014.

[22] Vinet A, Karpoff L, Walther G, et al. Vascular reactivity at rest and during exercise in middle-aged obese men: effects of short-term, low-intensity, exercise training. Int J Obes (Lond) 2011;35:820-8.

[23] Fujimoto N, Prasad A, Hastings JL, et al. Cardiovascular effects of 1 year of progressive endurance exercise training in patients with heart failure with preserved ejection fraction. Am Heart J 2012;164:869-77.

[24] Pemberton VL, McCrindle BW, Barkin S, et al. Report of the National Heart, Lung, and Blood Institute's Working Group on obesity and other cardiovascular risk factors in congenital heart disease. Circulation 2010;121:1153-9.

[25] Dulfer K, Duppen N, Kuipers IM, et al. Aerobic Exercise Influences Quality of Life of Children and Youngsters With Congenital Heart Disease: A Randomized Controlled Trial. The Journal of adolescent health : official publication of the Society for Adolescent Medicine 2014;2:1-8.

[26] Takken T, Giardini A, Reybrouck T, et al. Recommendations for physical activity, recreation sport, and exercise training in paediatric patients with congenital heart disease: a report from the Exercise, Basic & Translational Research Section of the European Association of Cardiovascular Prevention and Rehabilitation, the European Congenital Heart and Lung Exercise Group, and the Association for European Paediatric Cardiology. Eur J Prev Cardiol 2012;19:1034-65.

[27] Diller GP, Dimopoulos K, Okonko D, et al. Exercise intolerance in adult congenital heart disease: comparative severity, correlates, and prognostic implication. Circulation 2005;112:828-35.

[28] Reneman RS, Arts T, Hoeks AP. Wall shear stress--an important determinant of endothelial cell function and structure--in the arterial system in vivo. Discrepancies with theory. Journal of vascular research 2006;43:251-69.

[29] Cibis M, Potters WV, Gijsen FJ, et al. Wall shear stress calculations based on 3D cine phase contrast MRI and computational fluid dynamics: a comparison study in healthy carotid arteries. NMR in biomedicine 2014;27:826-34.

[30] Helbing WA, Luijnenburg SE, Moelker A, et al. Cardiac stress testing after surgery for congenital heart disease. Curr Opin Pediatr 2010.

[31] Robbers-Visser D, Jan Ten Harkel D, Kapusta L, et al. Usefulness of cardiac magnetic resonance imaging combined with low-dose dobutamine stress to detect an abnormal ventricular stress response in children and young adults after fontan operation at young age. Am J Cardiol 2008;101:1657-62.

Chapter 10

General Discussion

Several cardiovascular diseases, either acquired during life or congenital, are associated with altered haemodynamic conditions of the blood vessels[1-5]. Monitoring haemodynamic changes in the diseased blood vessels might provide essential information on the status and the possible progression of these diseases. Cine phase contrast MRI (PC MRI) is an emerging tool which provides haemodynamic information non-invasively in large blood vessels[6-8]. The aim of this thesis was to investigate the potential use of PC MRI in monitoring haemodynamic parameters associated with two cardiovascular diseases: carotid atherosclerosis and univentricular heart (repaired by Fontan operation). The former is an example of an acquired cardiovascular disease and the latter of a congenital cardiovascular disease.

Chapters 2 to 5 are devoted to quantification of two haemodynamic parameters that are associated with carotid atherosclerosis; wall shear stress (WSS) and oscillatory shear index (OSI). In **chapter 2**, a study is described that focuses on the estimation of WSS based on CFD simulations and ECG and respiratory gated time-resolved 3D PC MRI with three directional velocity encoding, also known as 4D Flow MRI[9]. The two WSS quantification methods were compared in nine healthy carotid arteries (from 5 subjects). We performed the WSS analysis on the entire luminal surface of the carotid arteries, which is the main strength of this study compared to the previous studies. MRI-based WSS was previously obtained either by 2D PC MRI measurements which were performed at limited number of measurement planes[10-12] or by 4D Flow MRI measurements but the analysis was performed only at some planar slices of the carotid arteries[13,14]. In this study, 4D Flow MRI measurements were performed with an isotropic spatial resolution of 0.625 mm. CFD simulations were based on the subject-specific geometry and the boundary conditions were obtained from the 4D Flow MRI measurements Our results showed that MRI and CFD-based WSS spatial patterns are generally in good agreement. However, the magnitude of WSS is underestimated by MRI-based calculations due to the lower spatial resolution of 4D flow MRI measurements. The direction of the WSS vectors based on CFD and MRI is also in good agreement in general, although, deviations in the vector directions are larger at regions of low velocity due to the low velocity to noise ratio (VNR) at these regions. The general good agreement between MRI and CFD-based WSS calculations shows that MRI can be used in monitoring spatial WSS patterns, and it must be kept in mind that the magnitude of WSS is underestimated. Please note that the study presented in Chapter 2 was carefully designed and the MRI scans were carefully performed with dedicated multi-channel carotid coils, at an isotropic spatial resolution for a small group of young volunteers and without taking into account the clinical feasibility of the scan time to obtain the best image quality. One can however expect that MR images obtained for population-based studies have relatively lower image quality due to sub-optimal scan protocol parameters, which are generally chosen to keep the scan time clinically feasible. Another reason for lower image quality might be that the

MRI scans are not performed with the latest MRI equipment to maintain consistency between baseline and follow-up measurements in long-term follow-up studies. In a population-based setting, the agreement between MRI and CFD-based WSS distribution may therefore be reduced. On the other hand, CFD simulations are not feasible in such a setting due to long computational time requirement (hours to days per subject) and MRI-based WSS calculations are preferable since they are straightforward, less time-consuming and they do not require extensive pre and post-processing steps. Despite the lower accuracy of MRI-based WSS in a population-based setting, MRI can still be used for estimating WSS if similar associations between WSS and the vascular pathology are found by both MRI and CFD calculations. If so, this would open up a whole new line of research allowing populations studies on wall shear stress and taking more general confounding factors into consideration, which is not possible with small scale studies. Therefore, the aim of the study described in **chapter 3** was to investigate the agreement between MRI and CFD-based WSS distribution in a large population based setting. The subjects of this study that were selected from a cohort study (Rotterdam study), had an asymptomatic carotid plaque detected by ultrasound measurements. They underwent two MRI scan sessions within a follow-up period of approximately 4 years. The scans included black blood MRI and untriggered 3D PC MRI acquisitions. The wall thickness of the carotid arteries was obtained from the black blood images. CFD simulations were performed by using the subject-specific geometries. MRI-based velocities were used as boundary conditions for CFD. MRI and CFD-based WSS were compared at baseline. The baseline and follow-up WSS were also compared for both MRI and CFD-based calculations. Finally, the similarity of the relation between wall thickness and CFD-based WSS and the relation between wall thickness and MRI-based WSS was investigated. The results of this study confirmed our previous findings that the limited spatial resolution of MRI causes an underestimation of WSS. A similar inverse relation was found between wall thickness and WSS obtained by the two WSS estimation methods, which validated the potential use of both CFD and MRI. We conclude that application of MRI is feasible in estimation of WSS patterns also in a population-based setting since the associations between vascular pathology and WSS based on MRI measurements were similar to those based on CFD.

Our studies presented in chapter 2 and chapter 3 and also some previous studies from the literature[15-17] reported the underestimation of WSS due to the limited spatial resolution of MRI. None of the previous studies however investigated the effect of temporal resolution on the estimation of haemodynamic parameters. In addition, the degree of underestimation at different spatiotemporal resolutions and the minimum required spatiotemporal resolution for an accurate estimation of WSS remained unknown. If the relation between spatiotemporal resolution of MRI and the haemodynamic parameters is systematic, the underestimation depending on the resolution might be corrected.

In the study reported in **chapter 4**, the aim was to evaluate the effect of spatial and temporal resolution simultaneously on the assessment of mean and peak flow, WSS and OSI. These haemodynamic parameters were obtained with ECG gated time-resolved 2D cine PC MRI measurements, which were performed at two measurement planes of a carotid artery phantom at thirty different spatiotemporal resolutions. 2D PC MRI measurements were preferred, since thirty MRI measurements including those at very high spatiotemporal resolution would require infeasible scan times. In this study, 2D PC MRI measurements took between 1.1 and 21.0 minutes per measurement depending on the spatiotemporal resolution. The carotid artery phantom, which was based on the surface reconstruction of a healthy right carotid artery, was connected to a flow setup generating realistic pulsating flow. Our findings in this study showed that all haemodynamic parameters are influenced by spatiotemporal resolution but to different degrees. The mean flow was dependent on the spatial resolution due to the increased uncertainties in the image segmentation at lower spatial resolutions, but it was independent of temporal resolution. In contrast, the peak flow was mostly dependent on the temporal resolution. Since the flow waveform was flattened at lower temporal resolutions; the peak flow was underestimated. WSS was primarily influenced by the spatial resolution and underestimated at all spatial resolutions except for high resolution images ~$0.2\times0.2mm^2$. OSI was influenced by both spatial and temporal resolution. A remarkable observation was that at spatial resolutions lower than $0.4\times0.4mm^2$ and temporal resolutions lower than 40 ms, OSI did not significantly change. We also found that the location of the low and high WSS and OSI regions were estimated consistently in most of the measurements regardless of spatiotemporal resolution.

In **chapter 5**, a more clinically oriented study was described using CFD. The study investigated the relation between atherosclerotic plaque components and WSS distribution. The subjects were chosen from Rotterdam Study. Only a subset of the data was analyzed (93 carotid arteries from 74 subjects); hence performing CFD simulations was feasible. The MRI scan sessions included black blood MRI and untriggered 3D PC MRI sequences. Different sequences were used to evaluate the presence of plaque components. The evaluation of the presence of intra-plaque hemorrhage (IPH), large lipid rich necrotic core (LNRC) and calcium was performed by two trained observers. Subject-specific CFD simulations were performed using the luminal surface as geometry and the MRI-based velocities as inflow boundary condition. The results showed that WSS was higher at the regions of plaques with IPH. A possible explanation can be that IPH accelerates plaque growth hence it causes lumen narrowing and subsequently an increase in WSS. An association was also found between higher maximum shear stress and calcium. We did not find any relation between WSS distribution and LRNC prevalence. Further longitudinal research is necessary to determine the cause-effect relation between hemodynamic factors and the plaque composition.

Chapters 6 to 9 are primarily concerned with the estimation of haemodynamic parameters in Fontan circulation. Chapters 6 and 7 describe the studies that focus on the power loss estimation inside Fontan circulation. Previous studies suggested that power loss inside Fontan circulation is associated with the exercise intolerance of Fontan patients[18,19], but the amount of increase in power loss during exercise relative to rest condition was unknown. In **chapter 6**, the aim was to quantify power loss inside the Fontan circulation at rest and during exercise, which was simulated with dobutamine administration. The study included 15 subjects operated with intra-atrial later tunnel (ILT) and 14 subjects with extracardiac conduit (ECC) approach. CFD simulations were performed by subject-specific geometry and the boundary conditions were based on ECG gated time-resolved 2D PC MRI measurements. The results showed that the power loss inside Fontan circulation significantly and nonlinearly increased under exercise conditions. A nonlinear association between power loss and cardiac index was found. A clear difference in power losses was observed between ILT and ECC approaches.

In previous studies[20-23] and in the study presented in chapter 6, power loss inside Fontan circulation was calculated by CFD simulations. The potential use of 4D flow MRI in quantification of power loss was however never investigated mainly because it is expected that power loss is underestimated due to the limited spatial resolution of MRI. In **chapter 7**, the effect of spatial resolution and the noise of 4D flow MRI measurements on the estimated power loss inside Fontan circulation were discussed. One of the aims of the research was to quantify power loss inside Fontan circulation at different spatial resolutions of 4D flow MRI measurements. In vivo 4D Flow MRI measurements at several spatial resolutions were however not feasible due to unacceptably long scan times required for 4D flow MRI. The effect of resolution was therefore investigated by performing subject-specific CFD simulations and by down-sampling CFD velocities and generating MRI-like data. Power loss was calculated by using down-sampled CFD velocities at isotropic resolutions of 0.5 mm, 1.0 mm, and 2.0 mm and at subject-specific MRI resolution. The measurement noise, which was defined as the standard deviation of the measured velocities in static regions, was obtained from the phase images of the 4D flow MRI measurements. The subject-specific noise was added to the down-sampled CFD velocities to mimic MRI data. The effect of noise was studied by comparing the power loss calculated with and without adding noise. The power loss was underestimated by 66±4% with velocities at an isotropic spatial resolution of 2 mm relative to those at an isotropic spatial resolution of 0.1 mm. The underestimation of the power loss was due to the fading of complex flow structures by down-sampling the velocities. Adding noise on the velocities increased the estimated power loss slightly. Nevertheless, regardless of the noise or the spatial resolution, the relative power loss of each subject relative to the other patients was retained. Our findings in this study indicate that the patients having relatively high power loss inside the Fontan circulation can be detected by using 4D flow

MRI measurements even at lower spatial resolutions, but the magnitude of the power loss is underestimated.

Chapter 8 and 9 discuss the WSS distribution, distensibility and pulsatility of pulmonary arteries in Fontan patients. These haemodynamic parameters were studied in the pulmonary arteries since the pulmonary artery distensibility and the growth in these patients are limited and the underlying mechanism is unclear. It is however known that the endothelial cells which form the innermost layer of the arteries are responsive to WSS[24,25]. The reduced flow, hence reduced WSS inside Fontan circulation[26] might influence the endothelial function in the pulmonary arteries of Fontan patients. We hypothesized that the low level of WSS in the pulmonary arteries of Fontan patients might influence endothelium function and consequently the growth and function of the pulmonary arteries and the exercise capacity of these patients. **Chapter 8** focuses on the flow, WSS distribution, distensibility and pulsatility of the left pulmonary artery and the changes in these haemodynamic parameters over time. On twenty three Fontan patients two longitudinal time-resolved 2D cine PC MRI scans were acquired with a median follow up duration of 4.4 years. This study compared the associated haemodynamic conditions at baseline and follow-up within the Fontan patient group and between healthy controls and Fontan patients. We found that the blood flow, mean and peak WSS, the pulsatility and the distensibility of the pulmonary arteries were lower in Fontan patients than in healthy controls. No significant difference was found in lumen area and mean and peak WSS between baseline and follow-up in Fontan patients. Further research is necessary to identify the effect of haemodynamics on the growth and function of pulmonary arteries.

We hypothesized that increasing WSS in Fontan circulation by i.e. exercise training might improve endothelial function and consequently increase exercise capacity. In **chapter 9**, WSS distribution, distensibility and pulsatility of caval veins and pulmonary arteries were assessed before and after a twelve week of standardized exercise training in Fontan patients. The haemodynamic conditions of the randomly selected Fontan group assigned to exercise training were compared with the Fontan control group and a healthy control group. The results showed that flow, WSS, distensibility and pulsatility were low in Fontan patients relative to the healthy controls, which confirmed the findings of chapter 8. However, the 12 weeks of training program did not alter the WSS, distensibility or pulsatility in Fontan patients. These findings suggest that short term exercise has no definite positive or negative impact on distensibility, flow and WSS distribution. Further research has to be conducted to find potential solutions to improve haemodynamic conditions, endothelial function and distensibility of pulmonary arteries in Fontan patients.

The chapters of this thesis were dedicated to quantification of haemodynamic parameters by using CFD simulations and PC MRI measurements. The results showed that PC MRI has a high potential since it enables in vivo measurements of time-resolved 3D blood velocity field in large vessels by using the intrinsic magnetic properties of blood in an external magnitude field. PC MRI has two superior properties relative to other velocity measurement techniques like ultrasound or tomography. Firstly, it is a non-invasive method, which does not require the use of ionizing radiation and it does not necessarily require the use of contrast agents. Secondly, it does not have any preferred direction for the measurements, unlike ultrasound, since three directional velocities can be measured at any cross-sectional area or volume of interest in any 3D orientation. Nevertheless, PC MRI has also some disadvantages and some issues still remain in use of PC MRI in estimation of derived haemodynamic parameters. Several important issues about PC MRI measurements and their potential remedies are discussed below.

FUTURE DEVELOPMENTS IN PHASE CONTRAST MRI

MRI is an expensive and a time-consuming imaging modality relative to other imaging modalities like ultrasound. The long scan times required for MRI do not only contribute to the cost but they also make MRI acquisitions impractical since patient motion increases with scan time and it results in image artefacts. Nevertheless, three dimensional time-resolved ECG and respiratory navigator gated PC MRI with velocity encoding in 3 directions (4D flow MRI) scans with whole heart coverage can nowadays be performed in less than 20 minutes with the current technical developments[27]. The enhancements in the MRI acquisition methods such as effective use of sparse sampling[28,29], radial acquisition[30] and multidimensional parallel imaging[31] will reduce the MRI scan times further in the future.

The main drawback of PC MRI in estimating the derived haemodynamic parameters arises from the limited spatial resolution. The haemodynamic parameters such as power loss, wall shear stress and oscillatory shear index are based on the spatial gradient of the blood velocities. The spatial gradient of velocities is underestimated due to its limited spatial resolution resulting in underestimation of the magnitude of these parameters. The maximum achievable spatial resolution of PC MRI is however limited due to scan time limits and due to the inverse relation of VNR to spatial resolution. As the resolution increases, the signal reduces; VNR reduces hence the precision gets lower. VNR can be improved by using dedicated coils that optimize the SNR or the acquisition, with stronger magnetic fields[32] and with the use of contrast agents[33,34]. Nevertheless, the studies presented in chapter 4 showed that the accurate estimation of haemodynamic parameters is only possible at very high isotropic spatial resolutions, i.e. in the order of 0.1 mm. In order to obtain accurate values based on 4D flow data, a correction might be used. For example, a look up table can be generated to approximate a correction factor for the different resolutions. Alternatively, relative values of the haemodynamic parameters can be used as suggested in Chapter 7 of this thesis instead of the absolute values in comparative studies, but in this case MRI protocols must be kept similar for valid comparison.

Another parameter influencing VNR hence the quality of the PC MRI measurements is the velocity encoding (Venc), which is the maximum detectable velocity by PC MRI measurements. Venc is tuned by the user before the measurement and it corresponds to the maximum phase shift of 180º. The velocities higher than Venc are represented incorrectly due to aliasing. Venc must therefore be estimated before the measurements and defined sufficiently high in order to prevent aliasing. On the other hand, VNR is inversely proportional to Venc, hence Venc must be kept as small as possible to keep VNR high. At low velocity regions where i.e. WSS and OSI are of interest, VNR is especially low. In order to improve VNR, the encoding schemes that have been recently introduced such as dual Venc encoding[35] or five-point balanced flow encoding[36] are recommended.

For the estimation of the WSS and OSI vectors along the entire 3D vessel wall, the vessel wall needs to be segmented for the entire cardiac cycle. Current methods employ a PC angiogram derived from the phase and magnitude images using pseudo-complex differences or sum of squares algorithms. This typically represents the angiogram only at peak systole. A time-resolved angiogram would be preferable to correctly determine WSS and OSI over the entire cardiac cycle, but with the limited contrast in the magnitude image at diastole and the slow velocities at diastole, a clear depiction of the lumen boundary is impossible. Therefore, typically 4D flow MRI derived WSS gets only evaluated at peak systole and OSI is very often not derived at all. To overcome this limitation, one could improve the magnitude image of the 4D flow MRI acquisition by using radial k-space acquisition approaches or other advanced acquisition improvements that allow for increase in the SNR without necessarily increasing the scantime.

The other sources of errors in PC MRI measurements are eddy current effects, Maxwell terms, and gradient field distortions. Eddy currents can be corrected as suggested in the literature by subtracting the spatially varying eddy current estimated from static tissue[37]. Maxwell terms and the gradient field distortions can be corrected during image reconstruction using the known gradient waveforms and gradient field models[38].

CLINICAL APPLICATIONS

The ultimate goal of estimating subject-specific haemodynamics is to provide clinically useful information. The information on subject-specific haemodynamics will eventually help to understand the underlying mechanisms of the vascular pathology, to predict the effect of flow alterations, to find markers for early diagnosis of the cardiovascular diseases, to predict the progression of these diseases and the outcome of the treatments.

The improvements in PC MRI and computational modelling will lead to their use for haemodynamic estimations in clinical routine more frequently. PC MRI, particularly

4D flow MRI, has high potential to become a clinical tool for paediatric patients with congenital heart disease and also other patients with acquired cardiovascular diseases and it would give the opportunity to not only improve patient diagnosis and treatment strategy, but also to learn more about those diseases.

The studies described in this thesis added to our existing knowledge on the estimation of the subject-specific haemodynamics. The extensive comparison of estimations based on PC MRI and computational fluid dynamics show that PC MRI leads to underestimation in the estimated values. However, both methods give similar haemodynamic patterns. Hence both methods would lead to similar conclusions if translated into routine clinical practice. This enhances our confidence in both computational fluid dynamics and also in phase contrast MRI based haemodynamic estimation.

REFERENCES

[1] Evans PC, Kwak BR. Biomechanical factors in cardiovascular disease. Cardiovasc Res. 2013 Jul 15;99(2):229-31.

[2] Peiffer V, Sherwin SJ, Weinberg PD. Does low and oscillatory wall shear stress correlate spatially with early atherosclerosis? A systematic review. Cardiovasc Res. 2013 Jul 15;99(2):242-50

[3] Hoi Y, Zhou YQ, Zhang X, Henkelman RM, Steinman DA. Correlation between local hemodynamics and lesion distribution in a novel aortic regurgitation murine model of atherosclerosis. Ann Biomed Eng. 2011 May;39(5):1414-22

[4] Frueh J, Maimari N, Homma T, Bovens SM, Pedrigi RM, Towhidi L, Krams R. Systems biology of the functional and dysfunctional endothelium. Cardiovasc Res. 2013 Jul 15;99(2):334-41

[5] Santhanakrishnan A, Maher KO, Tang E, Khiabani RH, Johnson J, Yoganathan AP. Hemodynamic effects of implanting a unidirectional valve in the inferior vena cava of the Fontan circulation pathway: an in vitro investigation. Am J Physiol Heart Circ Physiol. 2013 Nov 15;305(10):H1538-47.

[6] Singer JR (1978) NMR diffusion and flow measurements and an introduction to spin phasegraphing. J PhysESei Instrum 11:281–291 25.

[7] Von Schulthess GK, Higgins CB. Blood flow imaging with MR: spin phase phenomena. Radiology 157:687-695

[8] Nayak KS, Nielsen JF, Bernstein MA, Markl M, D Gatehouse P, M Botnar R, Saloner D, Lorenz C, Wen H, S Hu B, Epstein FH, N Oshinski J, Raman SV. Cardiovascular magnetic resonance phase contrast imaging. J Cardiovasc Magn Reson. 2015 Aug 9;17(1):71

[9] Dyverfeldt P, Bissell M, Barker AJ, Bolger AF, Carlhäll CJ, Ebbers T, Francios CJ, Frydrychowicz A, Geiger J, Giese D, Hope MD, Kilner PJ, Kozerke S, Myerson S, Neubauer S, Wieben O, Markl M. 4D flow cardiovascular magnetic resonance consensus statement. J Cardiovasc Magn Reson. 2015 Aug 10;17(1):72

[10] Oshinski JN, Ku DN, Mukundan S, Loth F, Pettigrew RI. Determination of wall shear stress in the aorta with the use of MR phase velocity mapping. JMRI. 1995; 5(6): 640–7.

[11] Stokholm R, Oyre S, Ringgaard S, Flaagoy H, Paaske WP, Pedersen EM. Determination of wall shear rate in the human carotid artery by magnetic resonance techniques. Eur J Vasc Endovascular Surg. 2000; 20(5): 427–33.

[12] Masaryk AM, Frayne R, Unal O, Krupinski E, Strother CM. In vitro and in vivo comparison of three MR measurement methods for calculating vascular shear stress in the internal carotid artery. AJNR.1999; 20(2): 237–45

[13] Stalder AF, Russe MF, Frydrychowicz A, Bock J, Hennig J, Markl M. Quantitative 2D and 3D phase contrast MRI: optimized analysis of blood flow and vessel wall parameters. Magn Reson Med. 2008; 60(5): 1218–31.

[14] Frydrychowicz A, Stalder AF, Russe MF, Bock J, Bauer S, Harloff A, Berger A, Langer M, Hennig J, Markl M. Three-dimensional analysis of segmental wall shear stress in the aorta by flow-sensitive four-dimensional-MRI. JMRI. 2009; 30(1): 77–84.

[15] Papathanasopoulou P, Zhao S, Köhler U, Robertson MB, Long Q, Hoskins P, Xu XY, Marshall I. MRI measurement of time-resolved wall shear stress vectors in a carotid bifurcation model, and comparison with CFD predictions. JMRI. 2003; 17(2): 153–62.

[16] Petersson S, Dyverfeldt P, Ebbers T. Assessment of the accuracy of MRI wall shear stress estimation using numerical simulations. JMRI. 2012; 36(1): 128–38.

[17] Van Ooij P, Potters WV, Guédon A, Schneiders JJ, Marquering HA, Majoie CB, vanBavel E, Nederveen AJ. Wall shear stress estimated with phase contrast MRI in an in vitro and in vivo intracranial aneurysm. JMRI. 2013; 38(4): 876-84

[18] Whitehead KK, Pekkan K, Kitajima HD, Paridon SM, Yoganathan AP, Fogel MA. Nonlinear power loss during exercise in single-ventricle patients after the Fontan: insights from computational fluid dynamics. Circulation 2007;116:I165-171.

[19] Itatani K, Miyaji K, Tomoyasu T, Nakahata Y, Ohara K, Takamoto S, Ishii M. Optimal conduit size of the extracardiac Fontan operation based on energy loss and flow stagnation. Ann Thorac Surg 2009;88:565-572; discussion 572-563.

[20] Bove EL, de Leval MR, Migliavacca F, Balossino R, Dubini G. Toward optimal hemodynamics: computer modeling of the Fontan circuit. Pediatr Cardiol 2007; 28:477-481.

[21] de Leval MR, Dubini G, Migliavacca F, Jalali H, Camporini G, Redington A, Pietrabissa R. Use of computational fluid dynamics in the design of surgical procedures: application to the study of competitive flows in cavo-pulmonary connections. J Thorac Cardiovasc Surg 1996;111:502-513.

[22] Dubini G, Leval, MR, Pietrabissa, R, Montevecchi, FM., Fumero, R. A numerical fluid mechanical study of repaired congenital heart defects application to the TCPC. Journal of Biomechanics 1996; 29:111-121.

[23] Haggerty CM, Restrepo M, Tang E, de Zélicourt DA, Sundareswaran KS, Mirabella L, Bethel J, Whitehead KK, Fogel MA, Yoganathan AP. Fontan hemodynamics from 100 patient-specific cardiac magnetic resonance studies: a computational fluid dynamics analysis. J Thorac Cardiovasc Surg. 2014 Oct;148(4):1481-9

[24] Cecchi E, Giglioli C, Valente S, Lazzeri C, Gensini GF, Abbate R, Mannini L. Role of hemodynamic shear stress in cardiovascular disease. Atherosclerosis. 2011 Feb;214(2):249-56.

[25] Malek AM, Alper SL, Izumo S. Hemodynamic shear stress and its role in atherosclerosis. JAMA. 1999 Dec 1;282(21):2035-42.

[26] Robbers-Visser D, Helderman F, Strengers JL, van Osch-Gevers L, Kapusta L, Pattynama PM, Bogers AJ, Krams R, Helbing WA (2008) Pulmonary artery size and function after Fontan operation at a young age. J Magn Reson Imaging 28: 1101-1107

[27] Cibis, M, Potters, WV, Gijsen, FJH, Marquering, H, vanBavel, E,van der Steen, AFW, Nederveen, AJ, Wentzel JJ. Wall shear stress calculations based on 3D cine phase contrast MRI and computational fluid dynamics: a comparison study in healthy carotid arteries. NMR Biomed. 2014 Jul; 27(7):826-34.

[28] Lustig M, Donoho D, Pauly JM. Sparse MRI: The application of compressed sensing for rapid MR imaging. Magn Reson Med 2007;58(6):1182-1195.

[29] Baltes C, Kozerke S, Hansen MS, Pruessmann KP, Tsao J, Boesiger P. Accelerating cine phase-contrast flow measurements using k-t BLAST and k-t SENSE. Magn Reson Med 2005;54(6):1430-1438.

[30] Thompson RB, McVeigh ER. Flow-gated phase-contrast MRI using radial acquisitions. Magn Reson Med 2004;52(3):598-604.Pike GB, Meyer CH, Brosnan TJ, Pelc NJ. Magnetic resonance velocity imaging using a fast spiral phase contrast sequence. Magn Reson Med 1994;32(4):476-483.

[31] Jung B, Stalder AF, Bauer S, Markl M. On the undersampling strategies to accelerate time-resolved 3D imaging using k-t-GRAPPA. Magn Reson Med. 2011 Oct; 66(4):966-75.

[32] Aurélien J. Trotier, William Lefrançois, Kris Van Renterghem, Jean-michel Franconi, Eric Thiaudière, Sylvain Miraux. Positive contrast high-resolution 3D-cine imaging of the cardiovascular system in small animals using a UTE sequence and iron nanoparticles at 4.7, 7 and 9.4 T. J Cardiovasc Magn Reson. 2015; 17(1): 53.

[33] Bock J, Frydrychowicz A, Stalder AF, Bley TA, Burkhardt H, Hennig J, Markl M. 4D phase contrast MRI at 3 T: effect of standard and blood-pool contrast agents on SNR, PC-MRA, and blood flow visualization. Magn Reson Med. 2010 Feb;63(2):330-8. doi: 10.1002/mrm.22199.

[34] Michael P Hartung, Thomas M Grist, Christopher J François. Magnetic resonance angiography: current status and future directions. J Cardiovasc Magn Reson. 2011; 13(1): 19.

[35] Nett EJ, Johnson KM, Frydrychowicz A, Del Rio AM, Schrauben E, Francois CJ, Wieben O. Four-dimensional phase contrast MRI with accelerated dual velocity encoding. J Magn Reson Imaging. 2012 Jun;35(6):1462-71.

[36] Johnson KM, Markl M. Improved SNR in phase contrast velocimetry with five-point balanced flow encoding. Magn Reson Med. 2010 Feb;63(2):349-55.

[37] Walker PG, Cranney GB, Scheidegger MB, Waseleski G, Pohost GM, Yoganathan AP. Semiautomated Method for Noise Reduction and Background Phase Error Correction in MR Phase Velocity Data. J Magn Reson Imaging. 1993;3:521-530

[38] Bernstein MA, Zhou XJ, Polzin JA, King KF, Ganin A, Pelc NJ, Glover GH. Concomitant Gradient Terms in Phase Contrast Mr: Analysis and Correction. Magnetic Resonance in Medicine. 1998;39:300-308

Summary

Haemodynamic conditions are associated with the initiation and progression of cardiovascular diseases. Carotid atherosclerosis and the univentricular heart repaired by Fontan operation were introduced as examples of the acquired and congenital cardiovascular diseases. The associated haemodynamic parameters are generally quantified by computational fluid dynamics (CFD), but they can also be quantified by using phase contrast MRI (PC MRI) velocity measurements. The aim of this thesis was to evaluate the quantification of haemodynamic parameters associated with carotid atherosclerosis and univentricular heart repaired by Fontan operation by using PC MRI and CFD. Chapter 1 introduced the background and the aim of the thesis.

In chapter 2, wall shear stress (WSS) distribution based on ECG-gated time-resolved 3D phase contrast MRI was compared with that based on CFD in nine carotid arteries of six healthy volunteers. The MRI scans were performed with a 3T MRI scanner at an isotropic resolution of 0.625 mm. MRI-based velocities were used as the boundary conditions of CFD hence the CFD simulations were as subject-specific as possible. The CFD-based velocities were down-sampled to MRI resolution to generate MRI-like data. WSS was calculated with the MRI velocities, CFD velocities and the down-sampled CFD velocities. The results showed that MRI and CFD-based WSS patterns were in good agreement. The magnitude of WSS was however underestimated by both MRI and down-sampled CFD velocities indicating that the underestimation was caused by the limited spatial resolution. The direction of WSS vectors were also in good agreement in general. However, discrepancies were observed at the regions of low WSS. This study showed that the spatial WSS patterns based on MRI can be used in clinical routine despite the underestimation of the magnitude of WSS.

In chapter 3, a comparative study between MRI and CFD-based WSS was described for elderly subjects with asymptomatic atherosclerotic plaque. The aim of this study was to check the potential use of MRI in WSS calculation in population-based studies where lower image quality due to sub-optimal scan protocol parameters and MRI equipment are expected to keep the scan time clinically feasible. This was necessary since CFD simulations are not feasible in population-based studies due to the requirement of long computational time (hours to days) per subject. The subjects of this study (n= 14) were selected from Rotterdam study, which is a population-based cohort study. The subjects included in this study underwent two MRI scan sessions with an approximately four years of follow-up time and had artifact-free MR images. The wall thickness of the carotid arteries was obtained from MR images. WSS was calculated at baseline and follow-up with both MRI and CFD-based velocities and compared. Similar to our previous findings, we observed an underestimation of WSS based on MRI velocities due to

the limited spatial resolution. The mean WSS and the wall thickness did not significantly change over the follow-up period. We found an inverse relation between WSS and the wall thickness of the carotid arteries for both WSS estimation methods which suggests that studies on atherosclerosis and its relationship to MRI-based WSS patterns is feasible in a population-based setting.

In chapter 4, the effect of spatial and temporal resolution of MRI measurements on the estimated values of haemodynamic parameters was investigated. This study was performed to examine the degree of underestimation at different spatiotemporal resolution and to determine minimal requirement in resolution for accurate estimations. A carotid artery phantom was connected to a flow set-up supplying pulsatile flow. ECG-gated time-resolved 2D PC MRI measurements were performed at thirty spatiotemporal resolutions at two measurement planes of a carotid artery phantom. In this study, we preferred 2D PC MRI measurements due to the clinically infeasible scan times required for 3D PC MRI. The MRI scans took 1 to 20 minutes depending on the resolution. Mean and peak flow, WSS and OSI were compared for these spatiotemporal resolutions. The results showed that mean flow depends on spatial resolution while peak flow depends more on temporal resolution. WSS was influenced by spatial resolution and OSI was dependent on both spatial and temporal resolution. Nevertheless, the location of the low and high WSS and OSI regions were estimated consistently in most of the measurements regardless of spatiotemporal resolution.

In chapter 5, the association between WSS and plaque components was investigated in carotid arteries with early atherosclerosis. 93 carotid arteries from 74 subjects were selected from the population based Rotterdam study. The presence of plaque components such as intra-plaque haemorrhage (IPH), lipid rich necrotic core (LRNC) and calcifications was evaluated by two trained observers. By using MRI-based geometry and boundary conditions, subject-specific CFD simulations were performed to obtain WSS values. The associations between WSS measures and plaque composition were studied using generalized estimating equations analysis, adjusting for age, sex and carotid wall thickness. We found that IPH was more present in the plaques exposed to higher WSS. Higher maximum WSS was also significantly associated with the presence of calcifications. No associations were found between WSS and presence of LRNC.

In chapter 6, the power loss inside Fontan circulation at rest and during exercise was evaluated. MRI measurements were performed to obtain flow inside caval veins at rest and during exercise, which was simulated by dobutamine administration. Subject-specific CFD simulations were performed at three flow conditions: 1) at rest 2) during exercise which was simulated by dobutamine 3) during exercise which was assumed to increase the inferior caval vein flow twofold compared to the rest. 29 Fontan patients (15 intra-atrial lateral tunnel (ILT) and 14 extracardiac conduit (ECC)) were included. We found that the correlation between cardiac index and power loss was exponential.

There was a clear difference in power loss between patients operated with ILT and ECC approaches. In all flow conditions, ILT patients have lower power loss than ECC patients.

In chapter 7, the impact of spatial resolution and measurement noise of 4D flow MRI measurements on the estimation power loss inside Fontan circulation were evaluated. 6 Fontan patients underwent whole heart 4D flow MRI. Subject-specific CFD simulations were performed. The CFD velocities were down-sampled to isotropic spatial resolutions of 0.5 mm, 1mm, 2 mm and to MRI resolution. Viscous dissipation was compared between 1) high resolution CFD velocities, 2) CFD velocities down-sampled to MRI resolution, 3) down-sampled CFD velocities with MRI mimicked noise levels, and 4) in-vivo 4D flow MRI velocities. Relative viscous dissipation between subjects was also calculated. 4D flow MRI velocities were higher, although not significantly different than CFD based velocities. CFD-based viscous dissipation was significantly higher than those based on low resolution velocity fields. Relative viscous dissipation between different subjects was maintained irrespective of resolution and noise, suggesting that comparison of viscous dissipation between patients is still possible with MRI velocities at low resolution.

In chapter 8, the effect of the abnormal flow, which is due to lack of pulsatility in the pulmonary arteries (PA), on the size and function of PA's was discussed. 23 Fontan patients with a long term serial follow-up were included in this study. Median age was 11.1 (9.5-16.0) years at baseline and 15.5 (12.5-22.7) years at follow-up . Flow, WSSm distensibility, pulsatility and size of the left pulmonary artery (LPA) were determined using MRI measurements. A group of healthy peers was included as a reference. Flow and pulsatility were significantly lower in patients than in controls which might influence endothelium function and consequently the growth and function of the pulmonary arteries. Mean area was comparable in patients and controls, but distensibility was significantly higher in controls. Mean and peak WSS were significantly lower in Fontan patients. Area, pulsatility, distensibility and WSS did not change. Multivariable regression analysis showed that flow, area and age were important predictors for WSS.

In chapter 9, the effect of exercise training on WSS, distensibility and pulsatility of pulmonary arteries and caval veins was investigate in Fontan patients. A multi-center randomized controlled trial was conducted in Fontan patients (10 to 25 years). The exercise-group (n=28) received a 12-week exercise training program, 3 times per week, the control-group (n=17) did not. Healthy controls (n=17) underwent MRI measurements only at rest whereas Fontan participants were studied at rest and during exercise simulated by dobutamine administration. Similar to the findings in chapter 8, Fontan patients had significantly lower WSS, distensibility and pulsatility compared to healthy controls. The training program did not change WSS, distensibility and pulsatility within the exercise-group, or between the exercise and control-group. Exercise training did not alter WSS in relatively healthy Fontan patients. Further research is needed to unravel the key to increase PA endothelial-function.

In chapter 10, the main findings were reviewed. The challenges and the potential improvements in estimation of haemodynamic parameters using MRI measurements were discussed.

Samenvatting

Hemodynamische condities zijn van invloed op het ontstaan en de progressie van cardiovasculaire aandoeningen en de cardiovasculaire status van een patiënt. Voorbeelden van verworven en aangeboren cardiovasculaire aandoeningen zijn respectievelijk atherosclerose in de carotis en een univentriculair hart, dat kan worden verholpen met een Fontan operatie. Hemodynamische parameters worden doorgaans gekwantificeerd met behulp van numerieke stromingsleer (computational fluid dynamics, CFD), maar snelheidsmetingen met fase-contrast MRI (phase contrast MRI, PC MRI) kunnen ook gebruikt worden om deze parameters te bepalen. Het doel van dit proefschrift was om de kwantificatie van hemodynamische parameters geassocieerd met carotis atherosclerose en het univentriculaire hart, na toepassing van de Fontan operatie, met behulp van PC MRI en CFD te evalueren. In hoofdstuk 1 zijn de achtergrond en de doelstellingen van dit proefschrift nader beschreven.

In hoofdstuk 2 wordt een studie beschreven, waarin de wall shear stress (WSS) distributie, gebaseerd op ECG-gated time-resolved 3D fase contrast MRI, wordt vergeleken met de WSS distributie gebaseerd op CFD in negen carotiden van zes gezonde vrijwilligers. De MRI scans zijn uitgevoerd met een 3T MRI scanner, met een isotrope resolutie van 0,625 mm. De randvoorwaarden die gebruikt werden in de CFD simulatie, waren gebaseerd op de flow metingen gedaan met MRI en deze simulaties waren dus daarom zo subject-specifiek mogelijk. Met CFD kan de snelheids verdeling in een hoge spatiele resolutie verkregen worden. Om de CFD data in een resolutie te gebruiken vergelijkbaar aan de MRI werden de snelheden spatieel gemiddeld. WSS werd berekend met de MRI snelheden, CFD snelheden en CFD snelheden op lage resolutie. De MRI- en CFD-gebaseerde WSS patronen kwamen goed overeen. De hoogte van de WSS werd echter onderschat bij gebruik van snelheids verdeling op basis van MRI, als wel de snelheden op basis van CFD met een lage resolutie in vergelijking met de WSS waarden op basis van hoog resolutie CFD. Dit wijst erop dat de onderschatting het gevolg is van een beperkte spatiele resolutie. De richtingen van de WSS vectoren kwamen doorgaans goed overeen. Echter, discrepanties werden gezien bij lage WSS regio's. Deze studie heeft aangetoond dat WSS patronen, gebaseerd op MRI, gebruikt kunnen worden in de kliniek, ondanks de onderschatting van de hoogte van de WSS.

Hoofdstuk 3 beschrijft een studie waarbij in the carotis van oudere asymptomatische proefpersonen de MRI- en CFD-gebaseerde WSS werden vergeleken. Het doel van de studie was om te onderzoeken of ook de MRI, zoals toegepast in populatie studies, gebruikt kan worden voor WSS berekeningen. In populatie studies is de beeldkwaliteit doorgaans laag, als gevolg van een suboptimaal scan protocol en verouderde MRI apparatuur omdat de metingen over een langere tijd vergelijkbaar moeten zijn. Dit onderzoek was noodzakelijk omdat CFD simulaties in populatiestudies niet haalbaar zijn. Dit vanwege de het feit dat CFD uren tot dagen rekentijd kan kosten per persoon. De proefpersonen (n=14) waren geselecteerd uit de Rotterdam studie, een populatie-gebaseerde cohortstudie. De geïncludeerde personen ondergingen twee MRI scans met ongeveer vier jaar tussen periode. De wanddikte in de carotiden werd afgeleid van de MR beelden. WSS werd op beide tijdstippen berekend aan de hand van zowel MRI- en CFD-gebaseerde snelheden. In overeenstemming met onze voorgaande resultaten zagen we een onderschatting van de MRI-gebaseerde WSS, als gevolg van de beperkte spatiële resolutie. De gemiddelde WSS en wanddikte veranderden niet significant over een periode van 4 jaar. In de carotiden werd een inverse verband tussen wanddikte en WSS gevonden met beide methoden van WSS berekening. Dit suggereert dat het bestuderen van athersoclerosis in relatie tot MRI-gebaseerde WSS patronen haalbaar is in een populatie studie.

In hoofdstuk 4 werd het effect van spatiële en temporele resolutie van MRI metingen op de geschatte waarden van hemodynamische parameters onderzochten werd bepaald wat de minimaal benodigde resolutie voor nauwkeurige schattingen was. In deze studie werd gebruik gemaakt van een carotis phantom, die werd verbonden met een flow set-up die pulsatiele flow aanvoerde. ECG-gated time-resolved 2D PC MRI metingen werden uitgevoerd op dertig spatiotemporele resoluties op twee meetvlakken van de carotis phantom. In deze studie hebben we gekozen voor 2D PC MRI metingen, omdat 3D PC MRI metingen klinisch onhaalbaar lange scantijden zouden vragen. De MRI scans duurden tussen de 1 en 20 minuten, afhankelijk van de resolutie. Mean en peak flow, WSS en OSI werden vergeleken voor deze spatiotemporale resoluties. De resultaten wezen uit dat mean flow afhankelijk is van spatiele resolutie, terwijl peak flow meer afhangt van temporele resolutie. WSS werd beïnvloed door spatiele resolutie en OSI hing af van zowel spatiele als temporale resolutie. Desondanks werden in het merendeel van de metingen, ongeacht de spatiotemporale resolutie de hoge en lage WSS en OSI locaties consistent op de juiste locatie geschat.

In hoofdstuk 5 wordt een onderzoek beschreven, waarbij het verband tussen WSS en plaque componenten werd onderzocht in carotiden met vroege atherosclerose in 93 carotiden van 74 proefpersonen. Deze proefpersonen werden geselecteerd uit de populatie-gebaseerde Rotterdam studie. De aanwezigheid van plaque componenten zoals plaque bloedingen, vetrijk necrotisch weefsel en kalk werden geëvalueerd door twee getrainde onderzoekers en de WSS werd berekend met CFD in subject-specifieke 3D reconstructies gebaseerd op de MRI beelden. Het verband tussen WSS metingen en plaque compositie werd onderzocht met behulp van geavanceerde statistische analyses waarbij de resultaten gecorrigeerd werden voor de leeftijd,en het geslacht van de proefpersoon en de lokale wanddikte. We zagen dat plaque bloedingen vaker aanwezig zijn in plaques blootgesteld aan hogere WSS. Hogere maximum WSS hing ook significant samen met de aanwezigheid van calcificaties. Tussen WSS en de aanwezigheid van vetrijk nectrisch weefsel werd geen verband gevonden.

In hoofdstuk 6 wordenenergie verliezen in de Fontan circulatie geëvalueerd in zowel rust als tijdens inspanning., welke werd nagebootst door middel van dobutamine toediening. Patiënt-specifieke CFD simulaties werden uitgevoerd in drie flow condities: 1) in rust, 2) tijdens inspanning, nagebootst door dobutamine, 3) tijdens inspanning, die verondersteld werd de flow in de vena cava inferior te verdubbelen vergeleken met rust. 29 patienten met een Fontan circulatie (15 intra-atrial lateral tunnel (ILT) en 14 extracardiac conduit (ECC)) werden geïncludeerd in de studie. We zagen een exponentiele relatie tussen cardiac index en energie verliezen. Tussen patiënten geopereerd met ILT en ECC behandelingen was een duidelijk verschil in energie verliezen. Voor alle flow condities waren de energie verliezen in patiënten, die een ILT behandeling hadden ondergaan lager dan in patiënten, die een ECC behandeling hadden ondergaan.

Hoofdstuk 7 behandelt de impact van spatiele resolutie en meet ruis in 4D flow MRI metingen op de schatting van energie verliezen in de Fontan circulatie. Zes Fontan patienten ondergingen 4D flow metingen met MRI van het gehele hart en subject-specifieke CFD simulaties werden uitgevoerd. De CFD snelheden werden terug-gerekend naar isotrope spatiele resoluties van 0,5 mm, 1 mm, 2 mm en naar MRI resolutie. Visceuze dissipatie werd berekend op basis van 1) hoge resolutie CFD snelheden, 2) CFD snelheden terug-gerekend naar MRI resolutie met en zonder ruis, en3) in-vivo 4D flow MRI snelheden. 4D flow MRI snelheden waren hoger, maar niet significant verschillend van CFD-gebaseerde snelheden. Visceuze dissipatie gebaseerd op snelheden verkregen met CFD was significant hoger dan gebaseerd op lage resolutie MRI snelheidsvelden. De relatieve verschillen in visceuze dissipatie tussen patiënten bleef behouden, ongeacht resolutie en ruis. Dit suggereert dat het vergelijken van visceuze dissipatie tussen patiënten mogelijk is, zelfs voor snelheden die met MRI gemeten zijn op lage spatiele resolutie.

In hoofdstuk 8 wordt het effect van abnormale flow, veroorzaakt door afwezigheid van pulsatiliteit in de pulmonair vatenop de grootte en functie van de pulmonair arterie besproken. Een lange termijn studie werd uitgevoerd in 23 Fontan patiënten met een leeftijd van ongeveer 11 jaar (9.5-16). Bij aanvang van de studie en ongeveer 5 jaar later werden de patienten bestudeerd met MRI. Flow WSS, distensibiliteit en pulsatiliteit en grootte van de linker pulmonaal arterie werden bepaald met behulp van de MRI metingen. Een groep gezonde proefpersonen werd eveneens geïncludeerd als referentie. Flow en pulsatiliteit waren significant lager in de patiënten vergeleken met de controle groep. Dit zou invloed kunnen hebben op het functioneren van het endotheel en op het groeien en functioneren van de pulmonair arterien. Het doorstromings oppervlak van de pulmonaal arterie was in patiënten en controles vergelijkbaar, maar distensibiliteit was significant hoger in de controle groep. Mean en peak WSS waren significant lager in Fontan patiënten. Doorstromings oppervlak, pulstiliteit, distensibiliteit en WSS veranderden niet. Multivariabele regressie analyse wees uit dat flow, oppervlak en leeftijd belangrijke voorspellers zijn voor WSS.

In hoofdstuk 9 wordt het effect van inspanningstraining op WSS, distensibiliteit en pulsatiliteit van pulmonair arterien en de venae cava van Fontan patiënten beschreven. Een multi-center studie werd uitgevoerd in Fontan patiënten in de leeftijd van10 tot 25 jaar. De inspanningsgroep (n=28) volgde een trainingsprogramma 3 keer per week, gedurende 12 weken, terwijl de controle groep (n=17) geen trainings programma volgde. Gezonde controles (n=17) ondergingen alleen MRI metingen in rust, terwijl bij Fontan patiënten MRI metingen werden uitgevoerd in rust en tijdens inspanning, nagebootst door middel van dobutamine toediening. In overeenstemming met de resultaten in hoofdstuk 8, hadden Fontan patienten significant lagere WSS, distensibiliteit en pulsatiliteit, vergeleken met gezonde controles. Het trainingsprogramma had geen invloed op de WSS, distensibiliteit en pulsatiliteit van de pulmonaal arterie Inspanningstraining veranderde WSS niet in relatief gezonde Fontan patiënten. Meer onderzoek is nodig om uit te vinden hoe pulmonaal arterie endotheel-functie kunnen worden verhoogd.

In hoofdstuk 10 wordt teruggeblikt op de belangrijkste bevindingen van het onderzoek beschreven in dit proefschrift. Bovendien worden uitdagingen en potentiele verbeteringen in het schatten van hemodynamische parameters met MRI bediscussieerd.

Curriculum Vitae

Merih Cibiş was born on July 25, 1984 in Eskişehir, Turkey. She completed her high school education in 2002 at Yusuf Ziya Öner Science High School in Antalya, Turkey. In the same year, she started her undergraduate study in Mechanical Engineering Department of Middle East Technical University in Ankara, Turkey. After obtaining her Bachelor of Science degree in 2007, she was awarded TU/e Talent Scholarship to pursue her Master of Science degree at Eindhoven University of Technology. She completed her Master program in 2009. After graduation, she worked as a computational fluid dynamics specialist in industry. In 2011, she started working as a PhD student in Biomedical Engineering deparment of Erasmus Medical Center. Her PhD project focused on evaluation of haemodynamic parameters based on computaional fluid dynamics and phase contrast MRI measurements. Her work was presented at several national and international conferences. During her PhD period, she spent six months at the Radiology Department of Northwestern University in Chicago, as a visiting reseracher.

Publications

JOURNAL PAPERS

Steinman DA, Hoi Y, Fahy P, Morris L, Walsh MT, Aristokleous N, Anayiotos AS, Papaharilaou Y, Arzani A, Shadden SC, Berg P, Janiga G, Bols J, Segers P, Bressloff NW, **Cibis M**, Gijsen FH, Cito S, Pallarés J, Browne LD, Costelloe JA, Lynch AG, Degroote J, Vierendeels J, Fu W, Qiao A, Hodis S, Kallmes DF, Kalsi H, Long Q, Kheyfets VO, Finol EA, Kono K, Malek AM, Lauric A, Menon PG, Pekkan K, Esmaily Moghadam M, Marsden AL, Oshima M, Katagiri K, Peiffer V, Mohamied Y, Sherwin SJ, Schaller J, Goubergrits L, Usera G, Mendina M, Valen-Sendstad K, Habets DF, Xiang J, Meng H, Yu Y, Karniadakis GE, Shaffer N, Loth F. Variability of computational fluid dynamics solutions for pressure and flow in a giant aneurysm: the ASME 2012 Summer Bioengineering Conference CFD Challenge. J Biomech Eng. 2013 Feb; 135(2):021016.

Bossers SS*, **Cibis M***, Gijsen FJ, Schokking M, Strengers JL, Verhaart RF, Moelker A, Wentzel JJ, Helbing WA. Computational fluid dynamics in Fontan patients to evaluate power loss during simulated exercise. Heart. 2014 May;100(9):696-701.

Cibis M*, Potters WV*, Gijsen FJ, Marquering H, vanBavel E, van der Steen AF, Nederveen AJ, Wentzel JJ. Wall shear stress calculations based on 3D cine phase contrast MRI and computational fluid dynamics: a comparison study in healthy carotid arteries. NMR Biomed. 2014 Jul;27(7):826-34.

Cibis M, Jarvis K, Markl M, Rose M, Rigsby C, Barker AJ, Wentzel JJ, The effect of resolution on viscous dissipation measured with 4D flow MRI in patients with Fontan circulation: Evaluation using computational fluid dynamics. J. Biomech. 2015 Aug 12:BMD1500331

Bossers S, **Cibis M**, Kapusta L, Potters W, Snoeren MM, Wentzel JJ, Moelker A, Helbing W, Long term serial follow-up of pulmonary artery size and wall shear stress in Fontan patients. Accepted

Cibis M*, Potters W*, Selwaness M, Gijsen FJ, Franco O, Lorza AMA, van der Lugt A, Nederveen AJ, Wentzel JJ, Relationship between wall shear stress and carotid artery wall thickening MRI vs CFD. Submitted.

Cibis M*, Potters W*, Gijsen FJ, Marquering H, vanBavel E, Wentzel JJ, Nederveen AJ, Effect of temporal and spatial resolution of 3D cine phase contrast MRI in wall shear stress and oscillatory shear index assessment. Submitted

Duppen N, **Cibis M**, Wentzel JJ, Bossers S, Potters W, Moelker A, Kapusta L, Hopman M, Helbing W, The effect of exercise training on pulmonary artery wall shear stress, distensibility and pulsatility in children and young adults with Fontan circulation: a randomized controlled trial. Submitted.

Tuenter A, Selwaness M, Lorza AA, Schuurbiers J, Speelman L, **Cibis M**, van der Lugt A, de Bruijne M, van der Steen AFW, Franco O, Vernooij M, Wentzel JJ. High shear stress relates to intraplaque haemorrhage in asymptomatic carotid plaques. Submitted

* indicates the co-first authorship

PhD Portfolio

PhD Portfolio

Conference and symposium attendance	**Year**	**ECTS**
1st Optic in Cardiology Symposium, Rotterdam, NL	2011	0.6
Symposium Een Warm Hart (ICIN), Amsterdam, NL	2011	0.3
STW Annual Congress (STW), Nieuwegein, NL	2012	0.3
3rd Annual COEUR PhD Day (Erasmus MC), Rotterdam, NL	2012	0.3
ASME 2012 Summer Bioengineering Conference, Fajardo, Puerto Rico, USA	2012	1.2
4th Dutch Biomedical Engineering Conference , Egmond aan Zee, NL	2013	0.6
4th Annual COEUR PhD Day (Erasmus MC), Rotterdam, NL	2013	0.3
8th International Symposium on Biomechanics in Vascular Biology and Cardiovascular Disease, Rotterdam, NL	2013	0.6
7th World Congress of Biomechanics, Boston, USA	2014	1.5
6th Annual Meeting of the Benelux ISMRM Chapter, Maastricht, NL	2014	0.3
5th Dutch Biomedical Engineering Conference , Egmond aan Zee, NL	2015	0.6
9th International Symposium on Biomechanics in Vascular Biology and Cardiovascular Disease, Rotterdam, NL	2015	0.6
23rd Annual Meeting of ISMRM, Toronto, Canada	2015	2.0
SB3C Summer Bioenginering Conference, SLC, USA	2015	1.2

Courses	**Year**	**ECTS**
11th PhD Course 'In Vivo NMR (Wageningen University), Wageningen, NL	2012	3.0
Aneurismal and atherosclerotic disease (Erasmus MC), Rotterdam, NL	2012	1.5
Congenital Heart Disease COEUR PhD course (Erasmus MC), Rotterdam, NL	2013	1.5
Cardiovascular Imaging and Diagnostics COEUR PhD course (Erasmus MC), Rotterdam, NL	2013	1.5
Translational Imaging Workshop (AMIE), Rotterdam, NL	2013	1.4
English Biomedical Writing and Communication (Erasmus MC), Rotterdam, NL	2013	4.0
Biostatistics for Clinicians (NIHES), Rotterdam, NL	2014	2.0

Seminars	**Year**	**ECTS**
Congenital Heart Disease (COEUR), Rotterdam, NL	2011	0.2
Imaging Carotid Arteries: Structure and Function (COEUR), Rotterdam, NL	2011	0.2
Carotid Atherosclerotic Plaques: Biomechanics and Imaging (COEUR), Rotterdam, NL	2012	0.2

Podium Presentations	Year	ECTS
ASME 2012 Summer BioEngineering Conference, Fajardo, Puerto Rico, USA	2011	0.2
COEUR Research Seminar on Carotid Atherosclerotic Plaques: Biomechanics and Imaging,	2012	0.2
Rotterdam, NL	2013	0.2
4th Dutch Biomedical Engineering Conference , Egmond aan Zee, NL	2014	0.2
6th Annual Meeting of the Benelux ISMRM Chapter, Maastricht, NL	2015	0.2
5th Dutch Biomedical Engineering Conference , Egmond aan Zee, NL	2015	0.2
SB3C Summer Bioenginering Conference, SLC, Utah, USA		

Poster Presentations	Year	ECTS
8th International Symposium on Biomechanics in Vascular Biology and Cardiovascular Disease,	2013	0.4
Rotterdam, NL (2 Poster Presentations)	2014	0.2
7th World Congress of Biomechanics, Boston, USA		
9th International Symposium on Biomechanics in Vascular Biology and Cardiovascular Disease,	2015	0.6
Rotterdam, NL (3 Poster Presentations)	2015	0.6
23rd Annual Meeting of ISMRM, Toronto, Canada (3 Poster Presentations)		

Supervision	Year	ECTS
Graduation Proejct BSc Student Haagse Hogeschool	2014	2.0

Acknowledgements

It was the very beginning of my PhD; November 2011 was cold and dark in the Netherlands. A night in this country felt already too long. I was thinking how the coming four years would pass in Rotterdam. For a short while I even doubted my decision of beginning to my PhD. Years passed and I came to the end of this period, the densest, the most didactic, the most colourful period of my life, the years that I grew the most in terms of knowledge and personality. The thesis that you are holding now is the product of this period. There have been dozens of people around me who contributed to this period and I feel responsible to thank them all.

I would like to begin with a special thank you to my promoter, Prof. Dr. Antonius van der Steen. Dear Ton, I would like to express my gratitude for giving me the opportunity to pursue my PhD at Erasmus Medical Center and for being my promoter. I enjoyed being part of your group in every single day.

PhD is a long run with both up and downhills. Without a good supervision and support, a successful run to the end would have been very difficult if not impossible. For their support and supervision, I would like to acknowledge my co-promoters, Dr. Jolanda Wentzel and Dr. Aart Nederveen. Dear Jolanda, at any circumstance we came across during my PhD, I always felt your full trust and support. I am very grateful for these very productive four years, for your trust and patience and for the projects that we worked on together. Dear Aart, I am glad to have the opportunity to be in close collaboration with you in several projects and do MRI measurements at AMC. Thank you very much for all very fruitful discussions and the valuable work that we did together.

I would like to express my gratitude to Prof Dr. Wim Helbing, Prof Dr. Michael Markl and Prof. Dr. Ed van Bavel for the successful collaborations and for being in my reading committee. I would also like to thank Prof. Dr. Aad van der Lugt and Prof. Dr. Frans van de Vosse, for accepting to be member of my defense committee.

During my PhD, I found the opportunity to spend six months in the lab of Prof. Dr. Michael Markl at Northwestern University in Chicago. This period of six months in Chicago was one of the highlights of my PhD and my life. Dear Michael and Alex I am very thankful to you for giving me this opportunity and for your supervision.

Dear Wouter, I would like to thank you for the great teamwork. I learned a lot from you during our projects. Your diligence, your intelligence and your knowledge always impressed me. It was a pleasure to work with you. I wish you success in your new career.

Dear Sjoerd and Nienke, working with you gave me the chance to approach our scientific questions from a different perspective. I am thankful for the work that we did together.

Dear Frank, it was a pleasure to work with you in the lab. Our group would be less colourful without you. I am grateful for all our scientific discussions, your support in my projects and the delicious food you cooked during the conferences.

Dear Lambert, it was reassuring to have you next door at the office, so that I could disturb you with all my questions. Thanks for all your contribution. It is unfortunate for our lab not to have you around anymore. I wish you success in your new career.

Dear Ruoyu, it was very nice to share the office with you. I am not sure if I will ever have such a warm and nice office as ours. Thank you very much for all nice times.

Dear Jelle, we started our PhD's almost at the same time and now we are finishing it up on the same day. I am happy that we shared this journey. Thank you for all the times we had at our office, our work related discussions and for our friendship. I wish you the best with your future career. "Het komt wel goed schatje". And of course, I have to mention our unforgettable road trip with you and Annette.

I am also very grateful to all my colleagues, Kim, Kimmetje, Hans, Leah, Ayla, Harm, Mariana, Ali, Zaid, Dion, Mirjam, Quinn, Eric, Lennard, Astrid, Blerim, Andres, Bahar, Bibi, Pieter, Gijs, Nico, Klazina, Hans, Robert, Gracia, Mieke and all others, for all very fruitful scientific discussions and those very good memories.

Dear Susanne and Teodora, in such a short period of six months, we were able to establish great friendships. I feel very lucky for meeting you. The road trip that we had, ISMRM memories, our trip to Bremen and all other memories are indispensable. Dear Kelly, Pim and Julio, it was very nice to work at the same office with you. Thank you all for good times in Chicago.

Besides my colleagues, I would like to express my gratitude to my friends and family who have been around me during my PhD. Cancan and Ulaş, my dear friends, you are my reason to be in the Netherlands. Even if we are not together each day, knowing that you are somewhere very close always gives me strength. Dear İso, canım benim, thank you for our very interesting talks, your never ending energy, your Chicago visit and our tequila shots. ☺ Dear Ezgi, ablası çok tatlı, I always felt your place as my second home in the Netherlands, thank you for having your doors always so open to me. Dear Nesrin, we share the destiny of finishing up our PhD's around the same time. From now on we will only have shiny days. As you also mentioned, life after 30's will only be great! Dear Görkem, the very last bit of choir rehearsals with you was a lot of fun. I wish we started it way earlier. By the way, how is your marriage going? ☺ The lentil balls and all other so delicious food that you cook are worth mentioning as highlights of my PhD. Dear Sinan, aka Sinan aga, you have always been the source of laughs; your presence in our group makes it always very nice! Dear Nimo, annecik and dear Tunç, Rotterdam became a nicer place to live after you all moved to here. Thank you all for our all great memories in Rotterdam. Dear Umut, the days after you left were less interesting at Erasmus MC, thanks

for those colourful days with you. Dear Fırat, Derya, İremo, Melike, Seda, Ümit, Özge, Yasemin and Fanny I have the memories of all your smiling faces which make me happy.

During my PhD in Rotterdam, I found the opportunity to contribute to the Red Tulip Film Festival and the Red Tulip Choir. Being part of these organizations gave me the fortune to meet some great people like Mehmet abi, Tuncay, Özgül, Hatice, Osman, Marco, Burak hoca, Hayat, İnci and many others. I would like to especially thank Hayat and İnci. İyilğiniz, sevginiz öyle güzel ve çok ki bazen beni mahcup ediyor. Rotterdam'da varlığınız bana güç veriyor. Çok ama çok teşekkür ederim.

My dear paranymphs Beste and Nilhan, canlarım, your friendships make me feel lucky in life. Benim canım Nilüm, how can I think of a Rotterdam without you! Rotterdam without you is as meaningless as the library without books☺. We shared so much which makes me afraid of moving somewhere far from you, I hope we will always be as close, iyi ki varsın. Canım Bestem, we shared an office together and loads of memories. The final one was about the suitcase trade in a starbucks store☺. I am sure we will scale up those in our future.

My dear Jeroen, I met you in the very last part of my PhD. A very happy fortune. I am sure, the memories that we built in that short time are the assurance of many more in the future. Thank you for everything benim canım.

I am also very thankful to my parents and my brother for their love and support throughout my life. Canım Cemim, benim iyi ki kardeşim! Varlığın ve mutluluğun benim mutlu olma sebebim. Canım Selin, sen de benim iyi ki kardeşim :). Umarım hep güzel günlerimiz olsun. Canım annem ve babam, hangi sözler size olan teşekkür ve minnetimi ifade etmeme yeter bilemiyorum. Bana her adımımda destek oldunuz. Hayatımda verdiğim her kararda, yaptığım her güzel şeyde emeğiniz var. Canım babam, senin vizyonun olmasa ne bu tezi bitirebilir, ne de şimdiye kadar yapmış olduklarımı yapabilirdim. Canım annem, benim bitanem, senin sevgin desteğin sayesinde, herşeyi başarmak çok kolaydı. Siz benim şansımsınız. Herşey ama herşey için bin teşekkür ederim.